MEANLINE PERFORMANCE ANALYSIS OF RADIAL COMPRESSORS

A THESIS SUBMITTED TO
THE GRADUATE SCHOOL OF NATURAL AND APPLIED SCIENCES
OF
MIDDLE EAST TECHNICAL UNIVERSITY

BY

EMRAH GÜLLÜ

IN PARTIAL FULFILLMENT OF THE REQUIREMENTS
FOR
THE DEGREE OF MASTER OF SCIENCE
IN
MECHANICAL ENGINEERING

SEPTEMBER 2015

Approval of the thesis:

MEANLINE PERFORMANCE ANALYSIS OF RADIAL COMPRESSORS

submitted by **EMRAH GÜLLÜ** in partial fulfillment of the requirements for the degree of **Master of Science in Mechanical Engineering Department, Middle East Technical University** by,

Prof. Dr. M. Gülbin Dural Ünver _____
Dean, Graduate School of **Natural and Applied Sciences**

Prof. Dr. Raif Tuna Balkan _____
Head of Department, **Mechanical Engineering**

Prof. Dr. Haluk Aksel _____
Supervisor, **Mechanical Engineering Department, METU**

Examining Committee Members:

Prof. Dr. Kahraman Albayrak
Mechanical Engineering Department, METU _____

Prof. Dr. M. Haluk Aksel
Mechanical Engineering Department, METU _____

Assist. Prof. Dr. Cüneyt Sert
Mechanical Engineering Department, METU _____

Assoc. Prof. Dr. M. Metin Yavuz
Mechanical Engineering Department, METU _____

Assist. Prof. Dr. Ö. Uğraş Baran
Department of Mechanical Engineering, TED University _____

Date: _____

I hereby declare that all information in this document has been obtained and presented in accordance with academic rules and ethical conduct. I also declare that, as required by these rules and conduct, I have fully cited and referenced all material and results that are not original to this work.

Name, Last Name: EMRAH GÜLLÜ

Signature :

ABSTRACT

MEANLINE PERFORMANCE ANALYSIS OF RADIAL COMPRESSORS

Güllü, Emrah
M.S., Department of Mechanical Engineering
Supervisor : Prof. Dr. Haluk Aksel

September 2015, 106 pages

Due to the complex nature of flow within a compressor, two- and three-dimensional CFD codes are commonly employed in compressor design today and they are leading to levels of efficiency believed to be impossible a few years ago. However, these sophisticated CFD codes are costly and time-consuming. Many improvements can be done in a simple mean-line analysis during the preliminary design of a compressor which leads to fewer hours of fine tuning in CFD codes. Despite its inherent limitations, the one-dimensional flow analysis along a mean-line is a very practical and powerful tool to inexpensively design and analyze a compressor. Mean-line method employs fundamental flow equations along with some empirical models to address the flow losses and some important flow phenomena. The accuracy of the results directly depends on the validity of the empirical models employed. The aim of this thesis is to develop a computer program that can be used to predict the performance of a radial compressor using mean-line method. Validation of the empirical models has been carried out by comparing the results with the experimental data available in the literature.

Keywords: Compressor, Centrifugal Compressor, Radial Compressor, Mean-line

ÖZ

RADYAL KOMPRESÖRLERİN ORTA ÇİZGİ PERFORMANS ANALİZİ

Güllü, Emrah
Yüksek Lisans, Makina Mühendisliği Bölümü
Tez Yöneticisi : Prof. Dr. Haluk Aksel

Eylül 2015 , 106 sayfa

Günümüzde iki ve üç boyutlu HAD analizleri sıklıkla kompresör tasarımı için kullanılmaktadır ve bu analizler sayesinde bir kaç yıl önce imkansız gibi gözüken verim değerleri yakalanmaktadır. Ancak bu karmaşık HAD analizleri pahalı ve zaman alıcıdır. Ön tasarım sırasında bir çok iyileştirme basit bir orta çizgi analizi ile yapılabilmektedir ve bu HAD analizlerindeki ince ayar süresini bir hayli azaltmaktadır. Tabiatından dolayı kaynaklanan kısıtlamalara rağmen, orta çizgi boyunca yapılan bir boyutlu analiz ucuz bir şekilde kompresör analizi ve tasarımı yapmamızı sağlayan çok pratik ve güçlü bir araçtır. Bu yöntem temel akış denklemlerini empirik modeller ile birlikte kullanır. Empirik modeller bazı önemli akış olaylarını ve akış kayıplarını modellemek için gereklidir. Analizin sonuçları tamamen empirik modellerin doğruluğu ile alakalıdır. Bu tezin amacı orta çizgi analizi ile bir radyal kompresörün performansını tahmin edebilecek bir bilgisayar programı yazmaktır. Kullanılan empirik modellerin doğruluğunun gösterilmesi için literatürden alınan deneysel sonuçlar kullanılmıştır.

Anahtar Kelimeler: Kompresör, Santrifüj Kompresör, Radyal Kompresör, Orta Çizgi

To my family

ACKNOWLEDGMENTS

First of all, I want to thank my family for their support and patience during this work.

Next, I wish to express my gratitude to my supervisor Dr. M. Haluk Aksel and to my manager Taylan Ercan for their guidance.

Finally, I am thankful to my colleagues Gökhan Aran, Mert Erk and Mustafa Bilgiç for their support, advice and friendship.

TABLE OF CONTENTS

LIST OF TABLES

TABLES

LIST OF FIGURES

FIGURES

NOMENCLATURE

Symbols

a	$\mathrm{m/s}$	Speed of Sound
	m	Location of Point of Maximum Camber
A	$\mathrm{m^2}$	Area
b	m	Passage Width
B	-	Blockage
c	m	Chord
C	$\mathrm{m/s}$	Absolute Velocity
d	m	Diameter
D	m	Divergence Parameter
DF	-	Diffusion Factor
DR	-	Diffusion Ratio
E	-	Diffusion Efficiency
h	$\mathrm{j/kg}$	Specific Enthalpy
i	deg	incidence
I	-	Work Input Coefficient
L	m	Meanline Length
m	m	Meridional Position
M	-	Mach Number
nCV	-	Number of Control Volumes
N	$\mathrm{rad/s}$	Angular Velocity
p	$\mathrm{N/m^2}$	Pressure
P	W	Power
$peri$	m	Perimeter
r	m	Radius
R	$\mathrm{j/kg}$	Rothalpy
	$\mathrm{j/kg/K}$	Gas Constant of Air
Re	-	Reynolds number
$React$	-	Degree of Reaction
s	$\mathrm{j/kg/K}$	Specific Entropy
T	K	Temperature
U	$\mathrm{m/s}$	Peripheral Speed
X	-	Choke Trigger
W	$\mathrm{m/s}$	Relative Velocity
z	-	Number of Blades

α	deg	Flow Angle
β	deg	Blade Angle
γ	-	Specific Heat Ratio
θ	-	Normalized Total Temperature
	deg	Camber Angle
δ	-	Normalized Total Pressure
	deg	Deviation Angle
	m	Boundary Layer Thickness
η	-	Efficiency
	-	Effectiveness
μ	-	Stage Work Coefficient
	kg/m/s	Dynamic Viscosity
ϕ	-	Flow Coefficient
	deg	Wedge Divergence Angle
λ	-	Tip Distortion Factor
	-	Swirl Coefficient
σ	-	Slip Factor
	-	Solidity
ϵ	-	Meanline Radius Ratio
	-	Secondary Flow Area Fraction
ρ	$\mathrm{kg/m^3}$	Density
ω	rad/s	Angular Velocity
χ	-	Secondary Flow Mass Fraction
A_R	-	Area Ratio
c_f	-	Skin Friction Coefficient
c_p	j/kg/K	Specific Heat at Constant Pressure
C_p	-	Pressure Recovery Coefficient
C_r	-	Contraction Ratio
C_M	-	Disk Torque Coefficient
d_H	m	Hydraulic Diameter
D_{eq}	-	Equivalent Diffusion Factor
f_c	-	Head Loss Correction
F_u	-	Tangential Velocity Factor
h_{th}	m	Throat Line Length
L_B	m	Blade Mean Camberline Length
$\dot{m}$	kg/s	Mass Flow Rate
s_{CL}	m	Clearance Gap Width
t_b	m	Blade Thickness
α_c	deg	Streamline Slope Angle
θ_C	deg	Divergence Angle
κ_m	rad/m	Streamline Curvature
$\bar{\omega}$	-	Loss Coefficient

Acronyms

CFD	Computational Fluid Dynamics
IGV	Inlet Guide Vane
ISC	Inducer Stall Criterion
LC	Loss Coefficient
NS	Navier-Stokes
PR	Pressure Ratio
SC	Swirl Coefficient
TEIS	Two-Element-in-Series

Subscripts

-1	IGV Inlet
0	IGV Exit
1	Impeller Inlet
2	Impeller Tip
	Vaneless Diffuser Inlet
3	Vaneless Diffuser Exit
	Vaned Diffuser Inlet
4	Vaned Diffuser Exit
	Vaneless Space After Vaned Diffuser Inlet
5	Vaneless Space After Vaned Diffuser Exit
	Return Bend Inlet
6	Return Bend Exit
	Return Channel Inlet
7	Return Channel Exit
	Exit Duct Inlet
8	Exit Duct Exit
B	Blade
BL	Blade loading
C	Curvature
CH	Choke
CL	Clearance Gap
COR	Corrected
CR	Critical
D	Diffusion
DF	Disk Friction
DIF	Diffusion
e	Value at Boundary Layer Edge
FB	Full Blade
h	Hub

HS	Hub to Shroud
id	Ideal
imp	Impeller
INC	Incidence
j	Jet
jc	Junction
L	Leakage
LIM	Limiting
m	Meridional Component
p	Polytropic
	Primary
par	Parasitic
r	Radial Component
R	Recirculation
s	Isentropic
	Shroud
	Secondary
SB	Splitter Blade
SEP	Separation
SF	Skin Friction
SH	Shock
u	Tangential Component
z	Axial Component
t	Total Condition
v	Velocity
VD	Vaned Diffuser
VLD	Vaneless Diffuser
tar	Target
th	Throat
tt	Total-to-Total
w	Wake
∞	Perfect Guidance
$\star$	Throat Parameter

Superscripts

’	Relative Condition
$\star$	Sonic Condition
	Minimum
-	Mean

CHAPTER 1

INTRODUCTION

There are a number of different approaches used for aerodynamic design and analysis of turbo-machinery throughout the industry. They all utilize the basic principles of thermodynamics along with the experimental data, but in different combinations and in different complexity. Methods available in the literature vary from being completely non-dimensional to three-dimensional. A simple scaling of an existing design may be sufficient for some applications while a multistage Navier-Stokes (NS) solver is required for the others. However, a proper combination of methods of different complexities should be employed for an efficient design procedure.

Design of a modern compressor is not possible without the help of Computational Fluid Dynamics (CFD) and this dependency is increasing day by day. [1] Fully 3D, multistage NS solvers are commonly employed in the compressor design today. However, these solvers are still too expensive to be a design tool that all the design process can rely on. Therefore, they must be supported by simpler and less expensive methods and the design must be refined successively by the methods of increasing complexity.

Figure 1.1 gives an overview of the standard design methodology employed for a state-of-the-art compressor. Aerodynamic design is linked with many other disciplines such as aeromechanical, structural and thermal analysis. Aerodynamic design begins with cycle design where the specification of pressure ratio, mass flow rate, shaft speed, geometrical constraints, target efficiency and target surge margin are determined. After this, a meanline code is employed to determine the number of

stages required, thermodynamic conditions and velocities after each stage component, preliminary sizes and off-design performance. Next, inviscid quasi 3D solvers are used where the flow domain is divided into hub-to-tip (S2) and blade-to-blade (S1) surfaces. [2] These methods are supported by empirical inputs to account for blockage and flow losses. Streamline curvature method is generally employed for hub-to-tip analysis, also referred as through-flow analysis, where annulus geometry is optimized and radial distributions of all flow quantities are checked. Blade profiles are optimized by a blade-to-blade solver, which generally utilizes a 2D Euler code coupled with a boundary layer solver. Finally, 3-D Euler and N-S codes are employed for detailed annulus and 3D blade geometry optimization, stage matching, analysis of cavity and bleed flows and off-design map generation.

1.1 Objective

In this thesis, it is aimed to write a meanline code that can be used to design and analyze radial compressors. This code will be a part of design system mentioned above in the near future. Meanline analysis is a very useful tool in the early stages of compressor design. It allows the designer to make preliminary sizing and compressor map predictions with the knowledge of only overall dimensions and blade angles. This method makes use of fundamental flow equations along with the empirical input. Accuracy of the obtained results is determined by the accuracy of the empirical input.

1.2 Literature Survey

There are a variety of approaches to the meanline performance prediction of centrifugal compressors within the literature. Japikse [4] classifies them as Level 1, Level 2 and Level 3 design.

Level 1 design employs similitude techniques to scale an existing, successful design. Application of these techniques to radial compressors is explained in almost every introductory level book about compressors, such as Whitfield and Baines [5], Dixon

[6], Cumpsty [7] and Japikse and Baines [8]. It is not always possible to employ Level 1 design since, for example, the scaling may require too high rotational speed which exceeds the stress limitations of the impeller. Another problem is that complete similitude is hard to achieve due to the scaling of the Reynolds number. Despite these limitations of the Level 1 design, it is employed very frequently in industry since it is fast and accurate.

Level 2 design employs empirical correlations derived from prior test experience for the overall component performance parameters, such as impeller efficiency, along with one-dimensional calculations. These correlations are generally derived for a certain type of machine and their application range is very limited. Japikse and Baines [4, 8] explain how such a design system works if these component correlations are available. It is not possible to find such correlations in the open literature since they are usually a company property.

Level 3 design employs a detailed set of models to represent the physics of the flow more accurately. This level of design requires the identification of different flow phenomena within each stage component and suitable models to estimate their effect on overall compressor performance. There are a variety of models to be used in the open literature. Oh *et al.* [9] compares the accuracy of different loss models presented in the open literature and suggest a set of loss models. Roberts [10] employs these loss models in his master's thesis and shows that they are indeed capable of modeling the impeller performance accurately. Whitfield and Baines [5] also summarizes the different models used in the open literature. Galvas [11] provides a Fortran program to predict the off-design performance of centrifugal compressors with channel diffusers. He employs a unique set of loss models taken from the literature and a surge and choke criteria to predict the operating range. Herbert [12] has an interesting study where he tries to model every stage component by employing variety of geometrical features. He couples the calculations with a boundary layer solver to estimate the blockage throughout the compressor stage. He defines a preliminary impeller shape by means of prescribed functions which enables a more detailed analysis to predict boundary layer growth, separation, flow blockage and energy dissipation. [5] Aungier [13, 14] and Japikse [4] provide a comprehensive set of models for every stage component of a radial compressor in a

well-documented and detailed way. Aungier employs one zone model to analyze the impeller flow while Japikse employs two zone model. Both methods have their advantages and disadvantages, which will be explained later in Chapter 3. One zone model analyses the impeller flow as a whole while two zone model divides it into two separate regions of different characteristics. Two zone model of Japikse is an improved version of Jet-Wake model of Dean and Senoo [15], which is based on the observations of Eckardt [16]. Eckardt observed and proved that the flow exiting from the impeller blades of a centrifugal turbomachine is divided into two regions, referred to as jet and wake. This idea is later improved by Japikse [4] and renamed as the two-zone model. It is experimentally verified that jet flow is almost isentropic while wake flow has all the flow losses. [4] Schiff [17], in his master's thesis, presents a detailed preliminary design and analysis procedure for the impeller, vaneless diffuser and vaned diffuser. He combines these procedures with some detailed geometrical calculations to create a preliminary impeller and diffuser geometry.

1.3 Scope

Radial compressor meanline theory used in this thesis mainly follows the work of Aungier [13], Japikse [4] and Herbert [12]. Aungier [13] provides very useful correlations and methodologies for the preliminary design and performance analysis of all stage components. Two zone model of Japikse [4] is a very popular technique to analyze impeller flow due to its physical base. It requires fewer empirical relations compared to traditional methods which makes it very practical in the preliminary design phase. Impeller gas path geometry calculation is done using equations provided by Herbert [12].

Validation of the developed code is done by the experimental test cases commonly used in the literature. Eckardt O-rotor [18, 19], Radiver [18, 20, 21], NASA CC3 [18, 22, 23] and 6.5 pressure ratio centrifugal compressor of Jones [18, 24] are used for this purpose.

The methodologies and correlations used in this thesis are widely used in the literature

and quite well documented. Validation of these methods has been done by many researchers. Therefore, they present a good starting point for a mean-line code that will be modified and corrected over the years by the experience of the author.

This thesis consists of 5 chapters. Chapter 2 gives some background information regarding fundamental concepts in radial compressor aerodynamics and Chapter 3 explain the meanline methodology used. The results are compared with some test cases in Chapter 4 and some concluding remarks are made in Chapter 5. Finally, a set of appendices are added to include some bulky and extensive theories used.

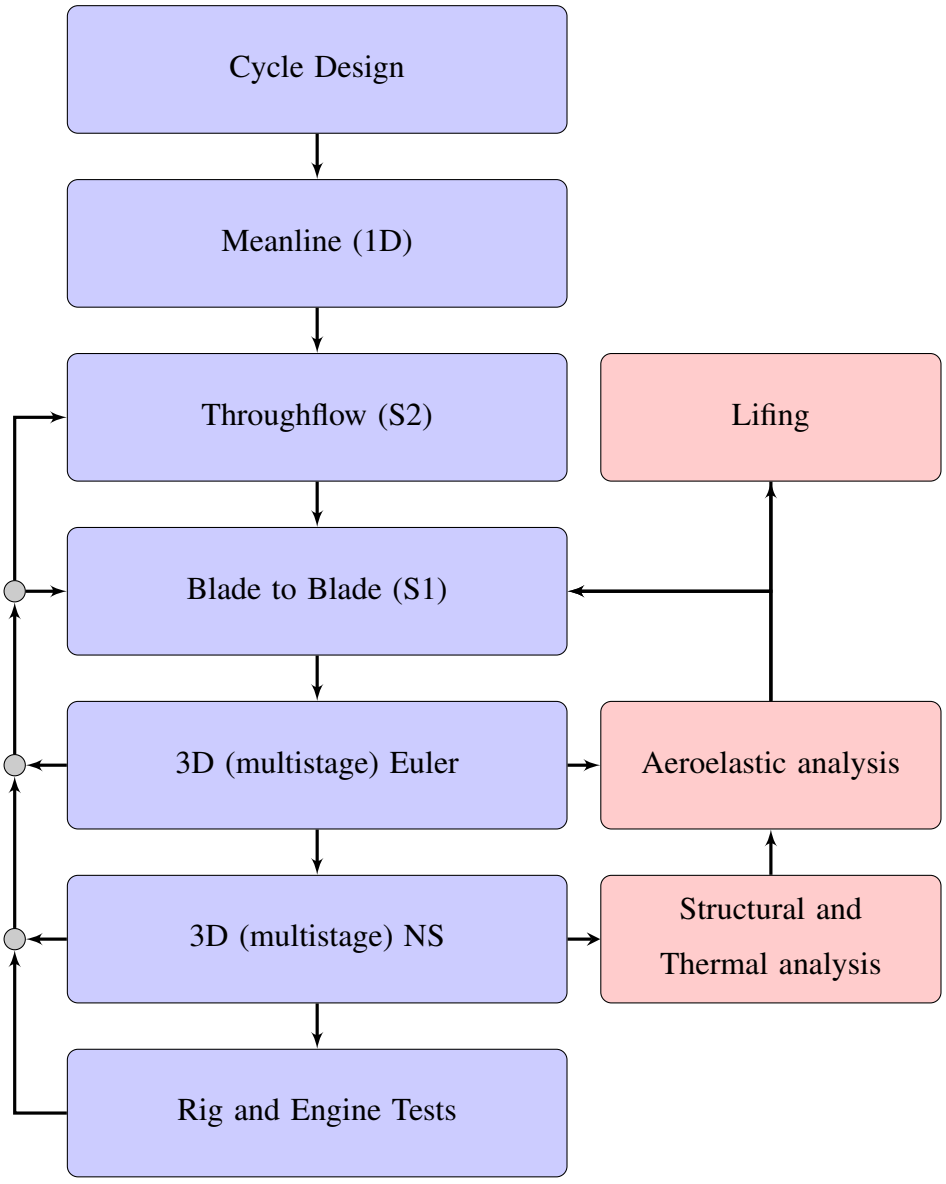

Figure 1.1: Aerodynamic Design Methodology [3]

CHAPTER 2

BACKGROUND INFORMATION

Gas turbine is one of the most popular means of producing mechanical power due to its high reliability and high power-to-weight ratio. It consists of three main components; the compressor, the combustion chamber and the turbine as shown in Figure 2.1.

First step in the cycle of a gas turbine is the compression of the working fluid in the compressor so that it can be expanded through a turbine. If there were no losses in either component, the work provided by the turbine would be just sufficient to drive the compressor. However, power developed by the turbine can be increased by the addition of energy to the working fluid prior to this expansion. If the working fluid is air, this energy addition can be done by the combustion of fuel in the compressed air. [25]

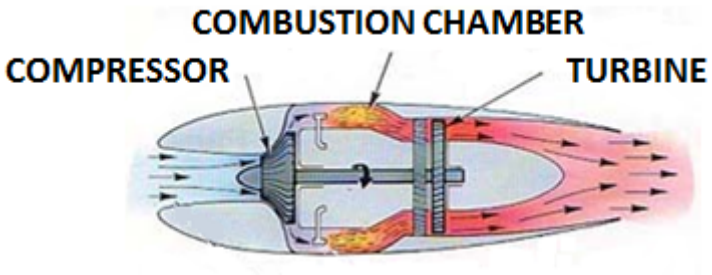

Figure 2.1: A Typical Gas Turbine [26]

Compressor is probably the most challenging component to design from an aerodynamic point of view. The flow through a compressor stage is diffusing, i.e., the flow is subject to adverse pressure gradients. Therefore, there is a risk of flow separation which brings the need for a control over the diffusion process in every

stage component. Flow separation can cause dramatic performance drops and stability problems.

Weight and cost are also other important parameters to consider besides the compressor performance and stability. It is important to keep the number of stages as low as possible in order to reduce weight and cost. This leads to more aerodynamically loaded blades (higher diffusion) which makes the compressor design even more challenging.

As it can be seen from Figure 2.2, the flow field within a compressor is quite complicated, three-dimensional and unsteady. Boundary layers develop both on blade surfaces and end walls. Vorticies form at the tip and hub corners. There are flows through the tip clearances due to the pressure difference between suction and pressure surfaces of a blade. There are also three-dimensional flow fields, named as secondary flow, generated by the interactions between the annulus boundary layers and the blade rows. If the maximum velocity on suction surface becomes supersonic, shocks can form and these shocks can cause boundary layer separations if they are strong enough. The flow field becomes even more complicated for a centrifugal machine where curvature effects of the annulus and strong Coriolis forces as a result of radial motion also comes into picture.

Basic information regarding compressor theory relevant to this thesis will be given in the following sections.

2.1 Classification of Compressors

Compressors are commonly classified as positive displacement and dynamic compressors. The positive displacement compressors achieve its pressure rise by forcing fluid into a confined space whose volume is decreased to compress the fluid while the dynamic compressors develop their pressure rise by the mechanical action of rotating blades that impart velocity and pressure to the continuously flowing fluid. Two basic types of dynamic compressors are centrifugal and axial flow compressors. Axial flow compressors have streamlines through their rotating blade rows which have almost constant radius while they undergo a substantial radius increase in

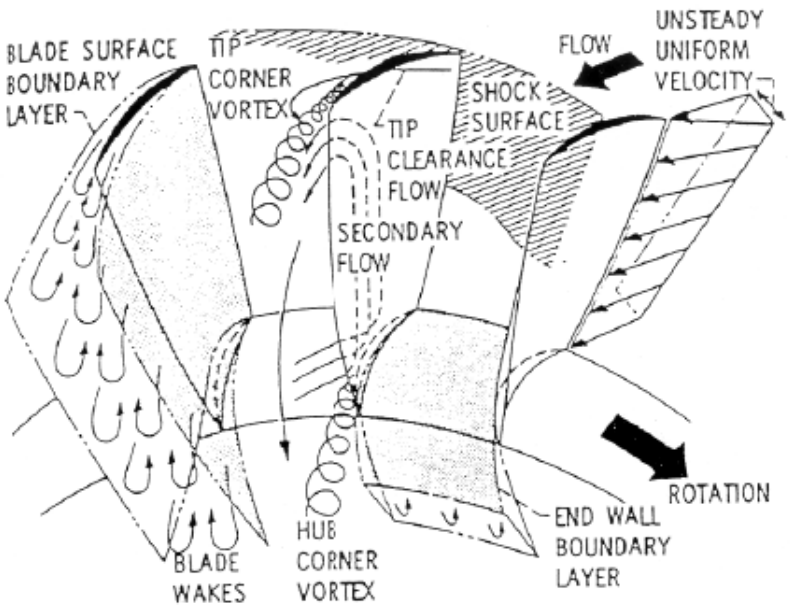

Figure 2.2: Flow Field within an Axial Compressor [27]

centrifugal compressors. For this reason, it is possible to obtain a higher pressure rise per stage in a radial compressor while an axial flow compressor can handle greater mass flow rate per unit frontal area. Radial compressors are more robust and of lower cost while axial flow compressors have the potential for better efficiency. [13]

An axial flow compressor consists of series of stages, where a stage refers to a rotating row (rotor) in combination with a stationary row (stator) as shown in Figure 2.3. The rotor rows impart kinetic energy to working fluid by increasing the swirl (tangential) velocity and stator rows remove the swirl developed to convert kinetic energy to static pressure. In addition, an inlet guide vane (IGV) and an exit guide vane (EGV) can be used to adjust the swirl velocity entering into and exiting from the stages for which the stages designed. Often the IGV is adjustable so that it can be restaggered to broaden the application range of compressors. [28] The working fluid passes through rotors and stators in this manner to increase the total pressure to the degree required in the engine cycle.

The basic operating principle of a centrifugal compressor is as follows. The fluid enters to the impeller through the eye. An inlet guide vane (IGV) can be employed

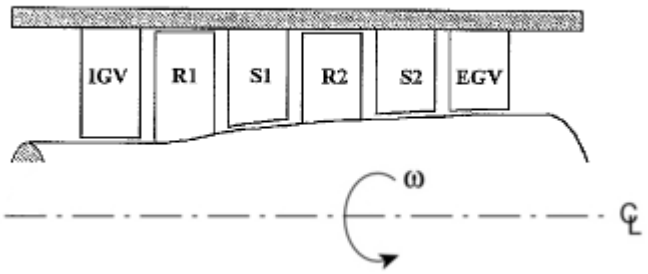

Figure 2.3: Axial Flow Compressor Configuration [28]

to introduce prewhirl to this flow and extend the operating range. The fluid then moves into the inducer, which is the axial portion of the impeller. The inducer transfers the fluid smoothly into the radial portion of the impeller, the exducer, where the rotating blades energize the fluid. Some of this energy is recovered as static pressure in the vaneless diffuser. A vaned diffuser can also be employed for further recovery of the remaining kinetic energy. Finally, a return system, which consists of a return bend and a return channel, directs the flow into the inlet of the next stage or into a combustion chamber. Vanes in the return channel also reduce the swirl developed by the preceding stage elements to the design value of the next stage element. Alternatively, for single-stage machines, a volute can be employed to smoothly collect the flow from the diffuser to the discharge pipe. Figures 2.4a and 2.4b show typical single and multistage centrifugal compressor configurations, respectively. [13]

2.2 Flow in a Rotating Coordinate System

The analysis of the flow in a rotating blade row is best accomplished in a coordinate system that rotates with the blades. The flow conditions in this coordinate system are called as relative conditions. If a blade row is rotating with an angular velocity, ω, blade speed at any radial position can be calculated as the product of rotational speed with the radial position, $U = \omega r$. Combining the blade speed vectorially with the relative velocity results in the absolute velocity. Both relative and absolute velocities have components in axial, radial and tangential directions. Combination of axial

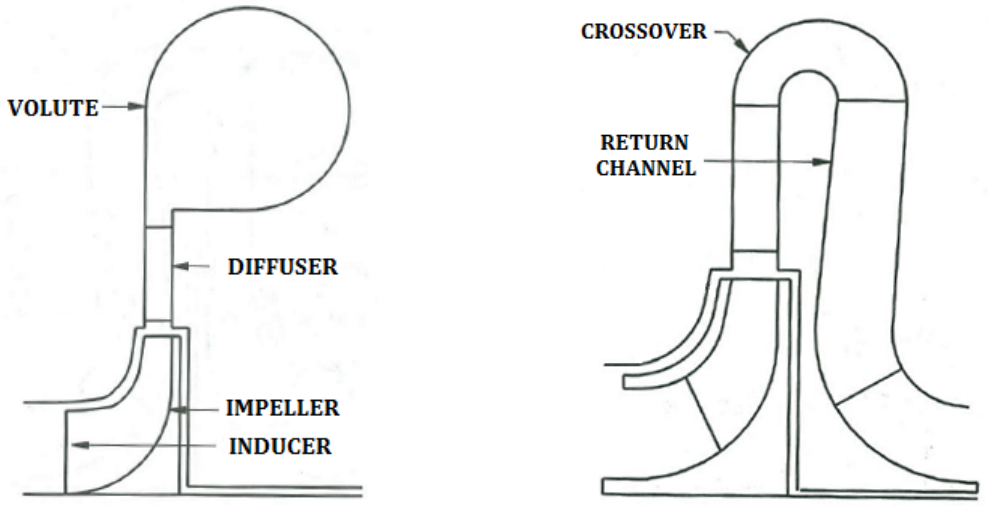

(a) Single Stage

(b) Multistage

Figure 2.4: Radial Compressor Configuration [13]

and radial components are termed as meridional component. Meridional components represent the mass flow through the stage while tangential components determine the energy transfer of the stage. That is,

$$\vec{W} + \vec{U} = \vec{C} \tag{2.1}$$

$$\vec{C_r} + \vec{C_z} = \vec{C_m} \tag{2.2}$$

$$\vec{C_m} + \vec{C_u} = \vec{C} \tag{2.3}$$

where W is the relative velocity and C is the absolute velocity while subscripts r, z, m and u represent radial, axial, meridional and tangential components respectively. Sketching these velocity vectors entering and leaving the blade rows in a form of so called velocity triangles is a very common and useful practice during compressor design. It makes it easier to visualize velocity and flow angle changes in a compressor stage. Velocity triangles for the rotor section of a compressor are shown in Figure 2.5.

If conservation of angular momentum is written between inlet (station 1) and outlet (station 2) of the rotating blade row, the power input supplied by the blade row is

$$P = \dot{m}(r_2 C_{u2} - r_1 C_{u1})\omega \tag{2.4}$$

where $\dot{m}$ is the mass flow rate and subscripts 1 and 2 represent the inlet and exit of the rotating blade row respectively. Combining above result with the first law of

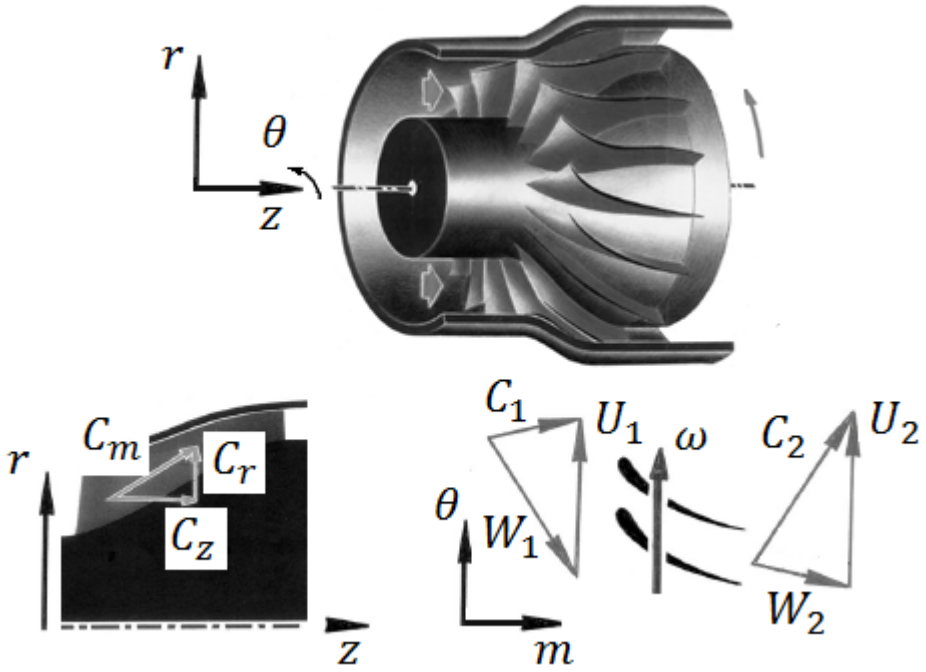

Figure 2.5: Velocity Triangles for the Rotor Section of a Compressor [29]

thermodynamics, the well-known Euler turbine equation is obtained as

$$h_{t2} - h_{t1} = \omega(r_2 C_{u2} - r_1 C_{u1}) \tag{2.5}$$

where h is the enthalpy and subscript t represents the total condition. The above equation can also be rewritten in the following form,

$$h_{t2} - \omega r_2 C_{u2} = h_{t1} - \omega r_1 C_{u1} \tag{2.6}$$

Therefore, it is convenient to define a parameter, R, as

$$R = h_t - \omega r C_u \tag{2.7}$$

which is constant along a stream sheet. This parameter is known as rothalpy.

Another useful form the Equation (2.6) can be obtained using the cosine theorem in the velocity triangle as,

$$h_{t2} - h_{t1} = \frac{W_1^2 - W_2^2}{2} + \frac{U_2^2 - U_1^2}{2} + \frac{C_2^2 - C_1^2}{2} \tag{2.8}$$

Therefore, total enthalpy rise is due to the decrease in the relative velocity, increase in the absolute velocity and change of radius. Making use of the relative total condition

definition, $h'_t = h + W^2/2$, and Equation (2.8), rothalpy can also be defined as,

$$R = h'_t - \frac{U^2}{2} \tag{2.9}$$

2.3 Performance Characteristics

Two compressor stages are completely similar if the ratios of all corresponding length dimensions, velocity components and forces are equal. Two completely similar machines have also similar performance which can be expressed by the dimensionless performance parameters. Although complete similarity is rarely achieved in practice, it can be approximated to yield good enough results.

The dimensionless performance parameters can be obtained using the so called Buckingham Pi theorem. Considering the various quantities that can influence the compressor behavior, it can be stated that

$$p_{t2}, RT_{t2} = f(d, N, \dot{m}, p_{t1}, RT_{t1}) \tag{2.10}$$

where p is the pressure, T is the temperature, R is the gas constant of the working fluid, d is a reference diameter of the compressor and N is the angular velocity. Therefore, the function given by the Equation (2.10) can be reduced to a different function of $7 - 3 = 4$ non-dimensional groups. These non-dimensional groups in their most useful form are

$$\frac{p_{t2}}{p_{t1}}, \frac{T_{t2}}{T_{t1}}, \frac{\dot{m}\sqrt{RT_{t1}}}{d^2 p_{t1}}, \frac{Nd}{\sqrt{RT_{t1}}} \tag{2.11}$$

Viscosity is also an important physical property that can affect the compressor behaviour. The presence of this variable would add another dimensional group having the character of Reynolds number. It is found from experience that the effect of this group is quite small in the normal operating range of most turbomachines. If the effect is not negligible, empirical correlations exist in the literature to add its influence. [25]

When dealing with the performance of a fixed size machine, R and d may be omitted from the groups and the inlet total conditions may be normalized by the reference

ambient state. ($p_{ref} = 1.013\,\text{bar}, T_{ref} = 288\,\text{K}$) Therefore,

$$f(\frac{p_{t2}}{p_{t1}}, \frac{T_{t2}}{T_{t1}}, \frac{\dot{m}\sqrt{\theta}}{\delta}, \frac{N}{\sqrt{\theta}}) = 0 \tag{2.12}$$

where $\theta = T_{t1}/T_{ref}$ and $\delta = p_{t1}/p_{ref}$. The function as given in Equation (2.12) states that any of the one group can be plotted against another while keeping a third constant. Experience has shown that the most useful plots are p_{t2}/p_{t1} and T_{t2}/T_{t1} against $\dot{m}\sqrt{\theta}/\delta$ while keeping $N/\sqrt{\theta}$ constant. The total temperature ratio can be replaced by isentropic efficiency, which is a function of total pressure and total temperature ratio. The typical compressor characteristics plots are shown in Figure 2.6. [25]

Each blade row has a specific inlet flow angle for which losses are minimum and it should operate close to this inlet flow angle at a specific operating condition, commonly referred to as compressor's design point. At flow rates less than the design flow rate, losses increase to a point where pressure-mass flow characteristics has a maximum. Lowering the flow rate even further, the characteristics have a positive slope which is theoretically unstable and onset of this severe unstable operation is called surge. Theoretical instability of the positive slope region can be explained as follows. Pressure rise developed by the compressor is less than the exit pressure of the compressor if the flow rate is reduced in this region. This causes forward flow through the compressor to stop and reverse its direction. After some point, pressure in the compressor exit drops below the pressure developed by the compressor and forward flow starts again. This causes a high frequency cycle of pressure build up and decay within the compressor which can cause severe mechanical vibrations. Surge is a very complex phenomenon that is highly dependent on the complete system, not just on the compressor. Although associating surge only with a positive slope on pressure-mass flow characteristics is an oversimplification, it is a useful one. [28]

Similarly, at flow rates greater than design flow rate, the increase in losses eventually reduces the stage pressure rise to zero. This is commonly referred to as choking. Large losses due to off-design operation can cause such an effect rather than a true aerodynamic choking condition, where the velocity of the flow reaches sonic speed somewhere within the compressor. [28]

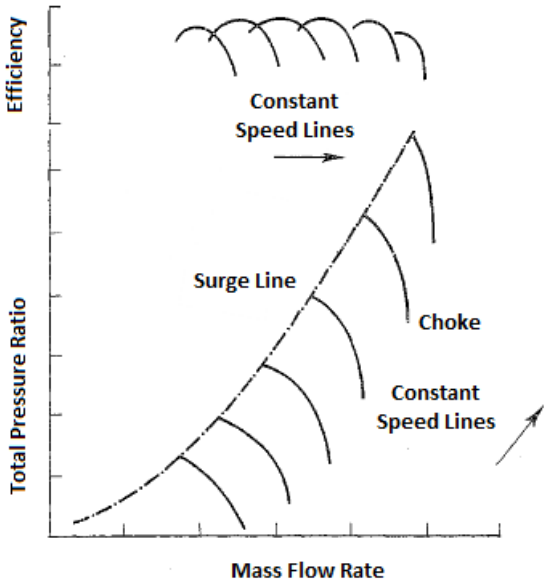

Figure 2.6: Typical Compressor Characteristics Map [25]

2.4 Efficiency and Loss Coefficient

Efficiency is a measure of the aerodynamic quality of a compressor and it can be defined as the actual performance relative to an ideal performance. One measure of efficiency is to compare the actual process to a reversible process. Since turbomachines are essentially adiabatic, the reversible process is also an isentropic one. Referring to Figure 2.7a, total-to-total isentropic efficiency of a compressor is defined as

$$\eta_s = \frac{h_{t2s} - h_{t1}}{h_{t2} - h_{t1}} \tag{2.13}$$

where subscript s represents the state after an isentropic process. Static conditions can be preferred instead of total conditions at the exit in the isentropic efficiency definition if the exit kinetic energy is wasted. This will yield the total-to-static isentropic efficiency.

Although adiabatic efficiency is the most common efficiency definition used for compressors, it cannot truly represent the aerodynamic quality of a compressor. Two compressor stages having same aerodynamic quality but different pressure ratios can

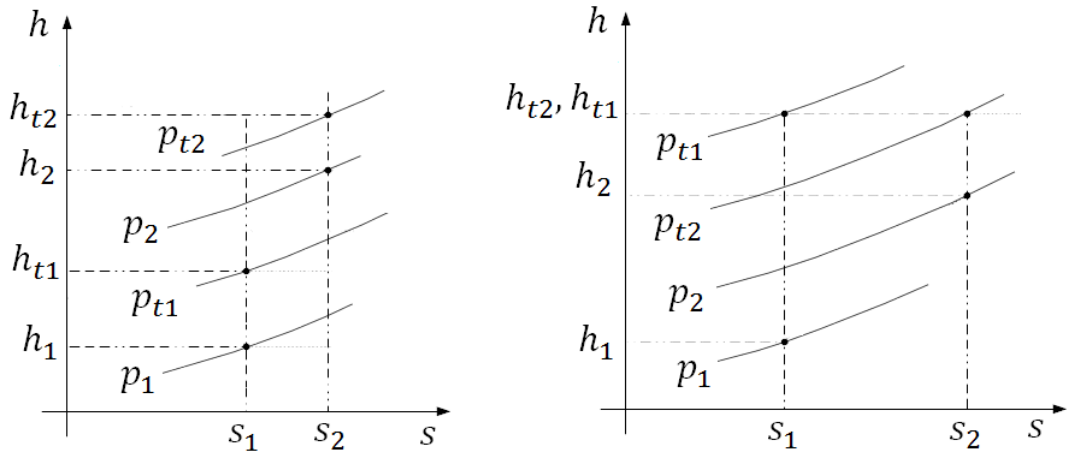

(a) Stage

(b) Stationary Component

Figure 2.7: Enthalpy-Entropy Diagram

have different isentropic efficiencies since constant pressure lines diverge on an $h - s$ diagram. Therefore, another efficiency definition, named as polytropic efficiency, is usually preferred over isentroic efficiency to evaluate the aerodynamic quality. Instead of using a constant entropy path, polytropic efficiency makes use of a path of constant efficiency. Assuming that a compressor consists of infinitesimal successive stages, polytropic efficiency is given by the isentropic efficiency of an infinitesimal stage such that it is constant throughout the whole process. [25] Therefore, it can be expressed as

$$\eta_p = \frac{\mathrm{d}h_s}{\mathrm{d}h} \tag{2.14}$$

which leads to the following formula for an ideal gas with constant specific heat,

$$\eta_p = \frac{R \ln(p_2/p_1)}{c_p \ln(T_2/T_1)} \tag{2.15}$$

The above efficiency definitions cannot be used to evaluate the aerodynamic quality of a stationary compressor component since, in the absence of heat transfer, the total enthalpy is constant. However, it is still useful to compare the performance of a stationary component to an ideal process. Pressure recovery coefficient, C_p, is one popular parameter used for stationary diffusing components. It is defined as the fraction of inlet dynamic pressure, $p_{t1} - p_1$, which is recovered as static pressure

rise. [13] Referring to Figure 2.7b,

$$C_p = \frac{p_2 - p_1}{p_{t1} - p_1} \tag{2.16}$$

Another measure of the irreversibility within a compressor is the loss coefficient. Since loss is usually proportional to kinetic energy, it is defined as

$$\bar{\omega} = \frac{\Delta p_t}{p_{t1} - p_1} \tag{2.17}$$

where Δp_t is the total pressure loss.

2.5 Dimensionless Parameters

There are a number of useful dimensionless parameters that are useful during the radial compressor design. They define the performance objectives the stage should achieve and the type of design that will be most effective in a form general to any stage design problem. [13]

Stage work coefficient and stage flow coefficient are defined as

$$\mu = \frac{\Delta h_{t,id}}{U_2^2} \tag{2.18}$$

$$\phi = \frac{\dot{m}}{\rho_{1t} \pi r_2^2 U_2} \tag{2.19}$$

where $\Delta h_{t,id}$ is the total enthalpy rise required to produce the total pressure rise of the compressor via an ideal process and ρ_{1t} is the inlet total gas density. The stage flow coefficient determines the achievable efficiency levels and type of design which will be most effective while the stage work coefficient represents how heavily loaded the stage is.

The rotational Mach number (also named as machine Mach number), M_U, is a popular dimensionless parameter used to characterize a centrifugal machine. It is given by

$$M_U = \frac{U_2}{a_{1t}} \tag{2.20}$$

where U_2 is the impeller tip speed and a_{1t} is the speed of sound based on inlet total conditions. It is a measure of the Mach number levels within the impeller and directly affects the stage pressure and temperature ratios.

Diffusion factor and diffusion ratio are common parameters that are used to limit the diffusion process. These parameters relate the peak velocity on the suction surface to the outlet velocity. They are defined as,

$$DR = \frac{W_{max}}{W_2} \tag{2.21}$$

$$DF = \frac{W_{max} - W_2}{W_1} \tag{2.22}$$

where W_{max} is the maximum relative velocity on the suction surface. Distribution of loading among the stage components is defined by the degree of reaction, $React$. It is defined as the ratio of static enthaply rise along the impeller to that of the stage. That is,

$$React = \frac{\Delta h_{impeller}}{\Delta h_{stage}} \tag{2.23}$$

Due to the influence of wall friction on performance, Reynolds number ($Re = \rho W d/\mu$), which is the ratio of inertia forces to viscous forces, is also another important characteristic parameter.

These parameters can be choosen or evaluated based on the design goals and previous experience.

CHAPTER 3

RADIAL COMPRESSOR MEANLINE THEORY

Radial compressor performance model used in this thesis has a modular structure. The main components of the stage are modeled separately. The stage consists of an impeller, a vaneless diffuser, a vaned diffuser and a return system. An inlet guide vane system (IGV) can also be included to broaden the operating range. Volute modeling is outside the scope of this thesis. Figure 3.1 and Table 3.1 show the station numbers and stage components used in this thesis. Velocity components and basic thermodynamic data are obtained at each computing station.

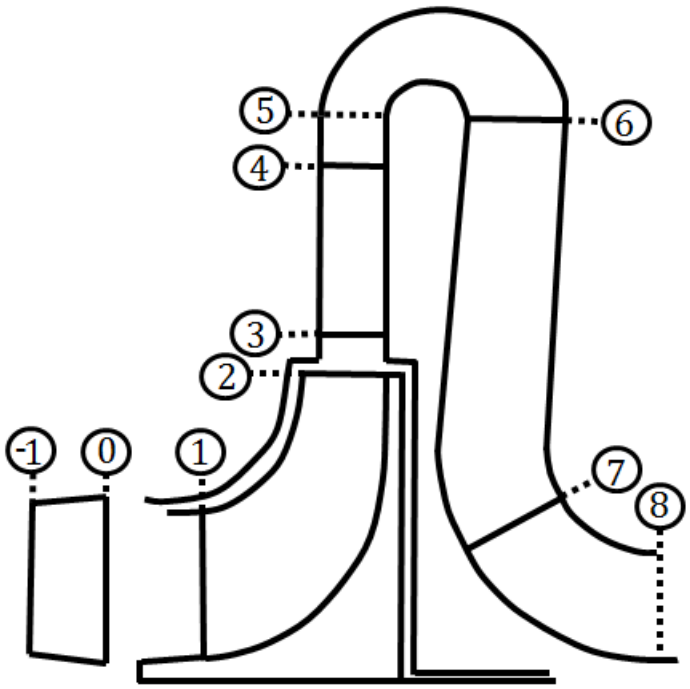

Figure 3.1: Computing Station Nomenclature [13]

Table 3.1: Computing Station Numbers

(-1)-(0)	IGV
(1)-(2)	Impeller
(2)-(3)	Vaneless Diffuser
(3)-(4)	Vaned Diffuser
(4)-(5)	Vaneless Space After Vaned Diffuser
(5)-(6)	Return Bend
(6)-(7)	Return Channel
(7)-(8)	Vaneless Space into Next Stage

Mathematical description of the each stage component and the related physics are explained in the following sections. Gas model used during these calculations is presented in Appendix A. The working fluid is air, which can be assumed ideal.

Each stage component requires input from its upstream stage components as inlet boundary condition. However, operation of the downstream components does not affect the operation of upstream components.

Most of the empirical correlations used in this chapter are taken from Aungier [13]. He mentions in his book that the validation studies for these correlations include stage flow coefficients ranging from 0.009 to 0.16 and pressure ratios up to 3.5, with actual application range is limited to pressure ratios up to 4.2. [13]

Most of the procedures presented below require some kind of iteration and simple guess and update procedure is used. These procedures are presented by means of flowcharts to show how the iterations are performed.

3.1 Impeller Performance

The impeller is the rotating component of the centrifugal compressor stage which is responsible for the energy transfer to the working fluid. It consists of an inducer, where the working fluid enters to the impeller smoothly, and an exducer, where the impeller energizes the working fluid. Figure 3.2 shows the impeller geometry with

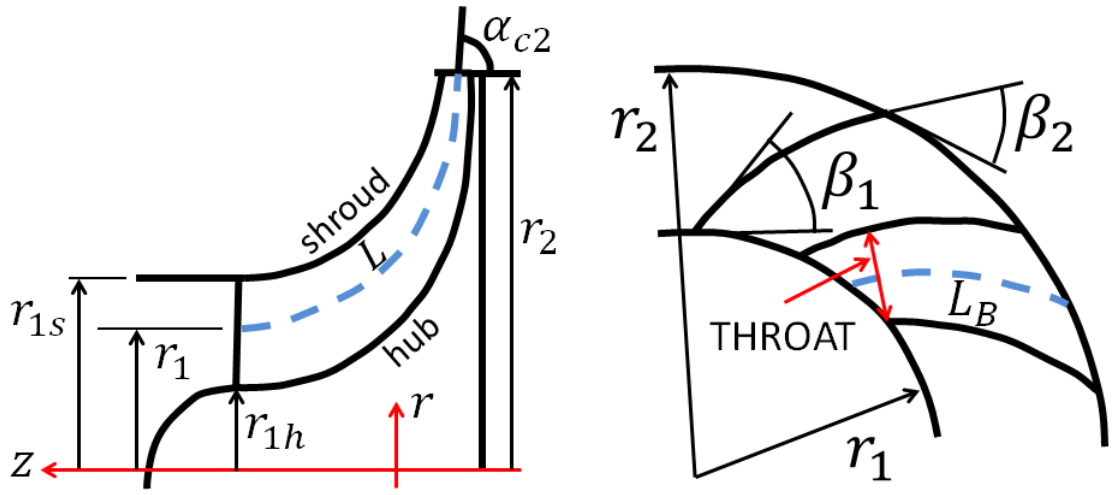

(a) Meridional Plane [19]

(b) Mean Stream Surface Plane [13]

Figure 3.2: Impeller Geometry

some key geometric parameters in the meridional and mean stream surface planes.

The inlet and outlet flow areas are calculated by,

$$A_1 = \pi(r_{1s}^2 - r_{1h}^2) - b_1 z_{FB} t_{b1} \tag{3.1}$$

$$A_2 = b_2[2\pi r_2 - (z_{FB} + z_{SB})t_{b2}] \tag{3.2}$$

where z_{FB} is the number of full blades, z_{SB} is the number of splitter blades, t_b is the blade thickness and b is the passage width. The impeller work input, I, is the total enthalpy rise imparted to the working fluid by the impeller in the dimensionless form. It is defined as,

$$I = \frac{\Delta h_t}{U_2^2} \tag{3.3}$$

The portion of this enthalpy rise supplied by the impeller blades is called blade work input coefficient or useful work, I_B. Rest of the impeller work input is termed as parasitic losses, which do not contribute to the pressure rise. The main parasitic losses are disk friction loss, recirculation loss and leakage loss. Disk friction loss, I_{DF}, is due to the adhesive interaction between the rotating disk and surrounding fluid in the clearance gaps. The recirculation loss, I_R, is generally seen in highly loaded impellers and it is caused by the fluid reversing its direction at the impeller tip. Finally, some of the leakage flow in the clearance gaps reenters into the impeller, creating the leakage

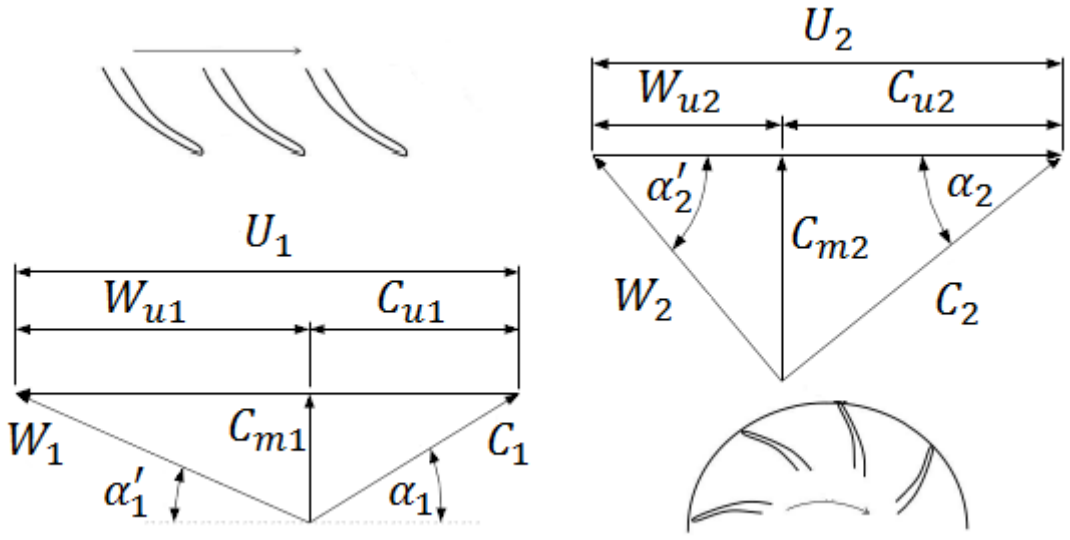

(a) Inlet

(b) Outlet

Figure 3.3: Impeller Velocity Triangles

loss, I_L [30, 31]. Therefore, the total work input coefficient is written as

$$I = I_B + I_{DF} + I_L + I_R \tag{3.4}$$

Using the Euler turbine equation given by Equation (2.5), the blade work input coefficient is,

$$I_B = \frac{C_{u2}}{U_2} - \frac{C_{u1}U_1}{U_2^2} \tag{3.5}$$

Velocity triangles for the inlet and outlet of the impeller are shown in Figure 3.3. Flow and blade angles are measured from tangential direction to be consistent with the work of Aungier [13].

If the flow is assumed to receive perfect guidance from the impeller blades, ${\alpha_2}' = \beta_2$, Equation (3.5) can be rewritten as,

$$I_B = 1 - \phi_2 \lambda \cot \beta_2 - \frac{C_{u1}U_1}{U_2^2} \tag{3.6}$$

where λ is the tip distortion factor, ϕ_2 is the tip flow coefficient and β_2 is the blade angle at the impeller tip. They are defined as,

$$\lambda = \frac{1}{1 - B_2} \tag{3.7}$$

$$\phi_2 = \frac{\dot{m}}{\rho_2 A_2 U_2} \tag{3.8}$$

where B_2 is area blockage at the impeller tip.

3.1.1 The Slip Factor

Perfect guidance of the flow by the impeller blades is only possible if there is infinite number of blades with infinitesimal thickness. In the real case, the relative flow angle always deviates from the blade angle for some appreciable amount. This is usually termed as slip. Referring to Figure 3.4, the slip velocity is defined as,

$$C_{slip} = C_{u2\infty} - C_{u2} \tag{3.9}$$

where $C_{u2\infty}$ is the tangential component of the absolute velocity if the flow follows the impeller blades perfectly. Based on slip velocity, a slip factor definition can be made as,

$$\sigma = 1 - \frac{C_{slip}}{U_2} = 1 - \frac{C_{u2\infty} - C_{u2}}{U_2} \tag{3.10}$$

Making use of this slip factor definition, velocity triangle given in Figure 3.4 and the Equation (3.6), the blade work input coefficient can be written as,

$$I_B = \sigma(1 - \phi_2 \lambda \cot \beta_2) - \frac{C_{u1} U_1}{U_2^2} \tag{3.11}$$

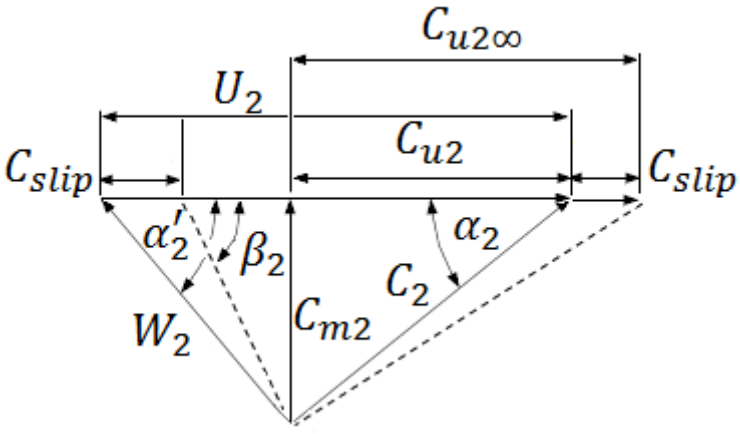

Figure 3.4: Tip Velocity Triangle with Slip

Therefore, there is a linear relation between blade work input coefficient, I_B, and tip flow coefficient, ϕ_2. The slope of this curve depends on the value of β_2. For an impeller with $\beta_2 < 90°$, also referred to as back-swept impeller, the slope is negative while for an impeller with $\beta_2 > 90°$, also referred to as forward-swept impeller, it is positive. Stability issues associated with positive slope was mentioned in Section 2.3. Therefore, a back-swept impeller is generally preferred. However, back-swept angle decreases the blade work input for the same flow coefficient. To keep the blade work input the same, impeller tip peripheral speed, U_2, should be increased with an increase in stress levels. Therefore, back-swept blading extends the operating range and improve the efficiency, but with the cost of increasing stresses. [4].

From Equation (3.11), it can be deduced that the slip factor is the ratio of actual blade work input to the value that would be obtained with perfect flow guidance for the case of zero inlet swirl velocity ($C_{u1} = 0$). It is also the blade work input coefficient that would be obtained for an impeller operating with zero mass flow for the same case.

The concept of slip factor can be explained by means of relative eddies forming within the impeller as shown in Figure 3.5. It can be assumed that the flow entering the impeller is irrotational. Hence, the flow must remain irrotational in the absolute frame of reference throughout the impeller. Relative eddies rotating in a direction opposite to the impeller are formed within the impeller to maintain this irrotationality. This concept is accepted as the main source of slip in radial flow turbomachines and people derived very useful correlations for slip factor just using the kinematics of these relative eddies, for example the slip factor model by Stodola. [32]

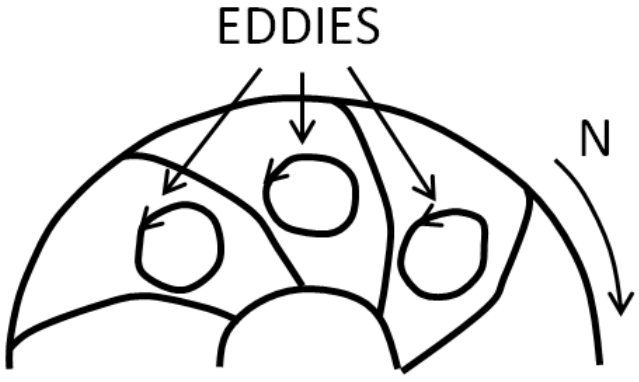

Figure 3.5: Relative eddy concept [31]

In this thesis, approximated Busemann slip factor by Wiesner is used to estimate the slip factor [13, 14]. It is given as

$$\sigma = 1 - \frac{\sin \alpha_{c2} \sqrt{\sin \beta_2}}{z^{0.7}} \tag{3.12}$$

where α_{c2} is the streamline slope angle at the impeller tip and z is the number of impeller blades. Equation (3.13) is valid up to the limiting meanline radius ratio, $\epsilon = r_1/r_2$, given by,

$$\epsilon_{LIM} = \frac{\sigma - \sigma_\star}{1 - \sigma_\star} \tag{3.13}$$

where $\sigma_\star = 19^\circ + 0.2\beta_2$. If this limiting radius ratio is exceeded, a corrected slip factor, σ_{COR}, is used. It is given by,

$$\sigma_{COR} = \sigma[1 - (\frac{\epsilon - \epsilon_{LIM}}{1 - \epsilon_{LIM}})^{\sqrt{\beta_2/10}}] \tag{3.14}$$

3.1.2 Splitter Blades

Centrifugal compressors designed for high rotational Mach numbers usually employ splitter blades, having partial length between adjacent full blades, as illustrated in Figure 3.6. They are used to reduce the blockage at throat while maintaining an acceptable blade solidity. Therefore, higher mass flow can be passed through the impeller before choking occurs by employing splitter blades.

The effective number of blades, z, given by the Aungier [13] is used to include the effect of splitter blades on the performance. It is given by,

$$z = z_{FB} + z_{SB} \frac{L_{SB}}{L_{FB}} \tag{3.15}$$

where L_{FB} and L_{SB} are the meanline lengths of the full and splitter blades.

3.1.3 Impeller Tip Blockage

High aerodynamic blockage is often encountered at the impeller exit due to the diffusing flow within the impeller. Correct estimation of the impeller tip blockage, B_2, or the impeller distortion factor, λ, is very important since it has a substantial

Figure 3.6: An Impeller with Splitter Blades [33]

effect on blade work input coefficient. Aungier [13] made the following observations during his experimental work:

(i) Blockage varies directly with the skin friction for very low flow coefficients

(ii) Blockage increases with the diffusion from impeller throat to impeller discharge

(iii) Blockage increases with blade aspect ratio, b_2/L_B

(iv) Blockage increases with blade clearance

Based on above observations, Aungier [13] formulated the impeller tip blockage as,

$$B_2 = \bar{\omega}_{SF}\frac{p_{v1}}{p_{v2}}\sqrt{\frac{W_1 d_H}{W_2 b_2}} + (0.3 + \frac{b_2^2}{L_B^2})\frac{A_R^2 \rho_2 b_2}{\rho_1 L_B} + \frac{s_{CL}}{2b_2} \tag{3.16}$$

where $\bar{\omega}_{SF}$ is the skin friction loss coefficient, d_H is the hydraulic diameter, L_B is the blade mean camberline length, s_{CL} is the clearance gap width, p_v is the dynamic pressure and A_R is the ratio of impeller tip flow area to throat area. A_R is defined by,

$$A_R = \frac{A_2 \sin\beta_2}{A_1 \sin\beta_{th}} \tag{3.17}$$

where β_{th} is the mean blade angle at the throat.

3.1.4 Inducer Analysis and Optimization

The aim of the inducer is to transfer working fluid from inlet to exducer with minimum loss. To achieve this goal, the following parameters should be controlled:

(i) approach relative velocity, W_1,

(ii) incidence, $i_1 = \beta_1 - \alpha'_1$,

(iii) preswirl, C_{u1} or α_1 and

(iv) local acceleration effects with subsequent diffusion as the flow passes around the blade leading edge

To establish the inducer velocity triangle shown in Figure 3.3a, the iterative procedure shown in Figure 3.7 should be executed. For the inlet blockage, B_1, recommendations given by Japikse [4] are included in Appendix A.

Meridional velocities at the hub and shroud of the inducer can be obtained using the following relations given by Aungier [13],

$$C_{mh1} = C_{m1}(1 + 0.5\kappa_{m1}b_1) \tag{3.18}$$

$$C_{ms1} = C_{m1}(1 - 0.5\kappa_{m1}b_1) \tag{3.19}$$

where κ_{m1} is the streamline curvature at the inlet. If the inlet swirl angle distribution and the meridional velocities are known, velocity triangles at the hub and shroud of the inducer can also be obtained.

Given the inducer hub radius, r_{1h}, or the inducer hub to tip ratio, r_{1h}/r_{1s}, as a constraint, the inducer tip radius, r_{1s}, which gives the minimum relative tip velocity, W_{1s}, can be found. This is referred to as inducer optimization. Flowchart given in Figure 3.8 can be followed to plot W_{1s} against C_{m1} for a given range of C_{m1}, as in Figure 3.9, and optimum r_{1s} can be spotted from this plot.

3.1.5 Throat Calculations

Throat of the impeller is the smallest area within the impeller passage where choking is most likely to occur. It plays a vital role in performance calculations since it

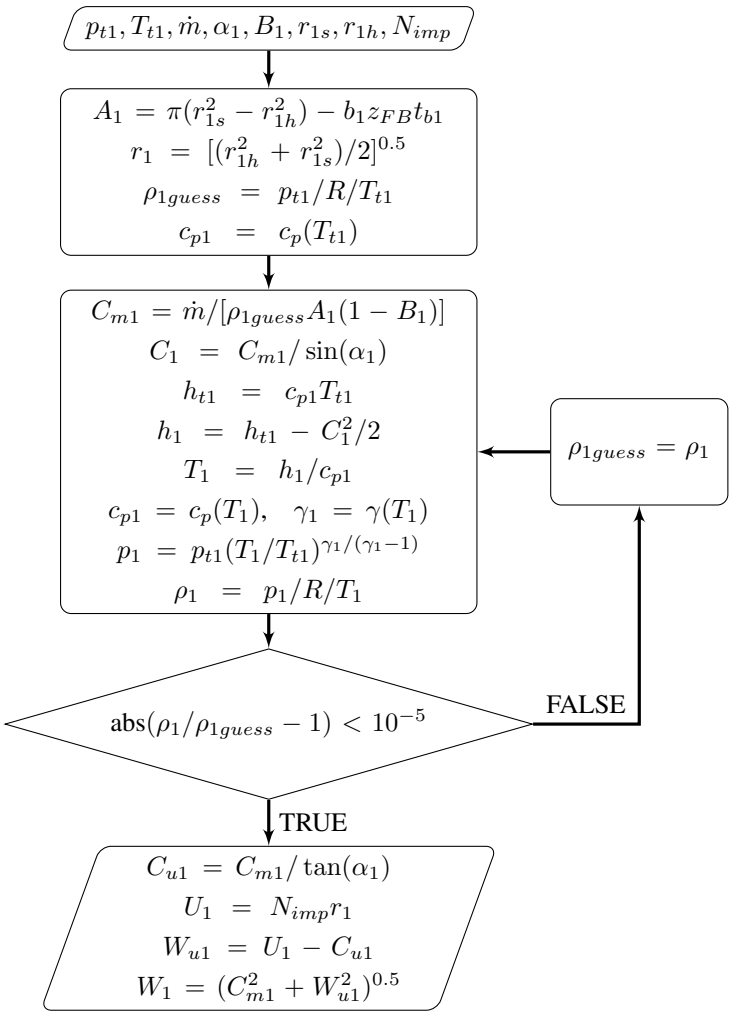

Figure 3.7: Inlet Analysis

determines the maximum mass flow rate that can pass through the impeller. To determine the onset of choking, total thermodynamic conditions (relative total conditions for the impeller case) must be known.

Since the throat is usually placed just after the inlet, the process between inlet to throat can be assumed isentropic, that is, total conditions at the inlet and throat are equal. It can also be assumed that the throat meanline radius is equal to the inlet meanline radius. These assumptions can be summarized as,

$$p_{tth} = p_{t1}, \quad T_{tth} = T_{t1}, \quad r_{th} = r_1 \tag{3.20}$$

The aerodynamic blockage in the impeller throat due to the sudden change in area

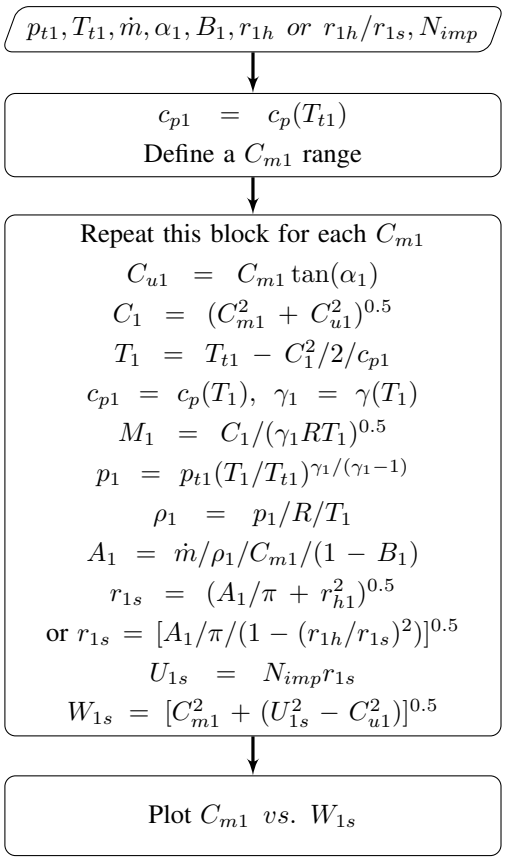

Figure 3.8: Inducer Optimization Algorithm

can be modeled by a contraction ratio as [13],

$$C_r = \min[(\frac{A_1 \sin\beta_1}{A_{th}})^{0.5}, 1 - (\frac{A_1 \sin\beta_1}{A_{th}} - 1)^2] \tag{3.21}$$

where A_{th} is the geometric throat area. The area for which the given mass flow rate and inlet total conditions yield a sonic velocity is given by,

$$A_{th}^\star = \frac{\dot{m}}{\rho_{th}^\star W_{th}^\star} \tag{3.22}$$

$$\rho_{th}^\star = \rho'_{tth}(\frac{2}{\gamma+1})^{1/(\gamma-1)} \tag{3.23}$$

$$W_{th}^\star = (\frac{2\gamma R T'_{tth}}{\gamma+1})^{0.5} \tag{3.24}$$

where superscript * represent sonic or critical condition. Choking will occur if $C_r A_{th} < A_{th}^\star$. Equations (3.22), (3.23) and (3.24) can be used for any vaned component by changing the relative values with the absolute ones for non-rotating components. The flowchart of the impeller throat calculations is given in Figure 3.11. Velocity triangle used during calculations is given in Figure 3.10.

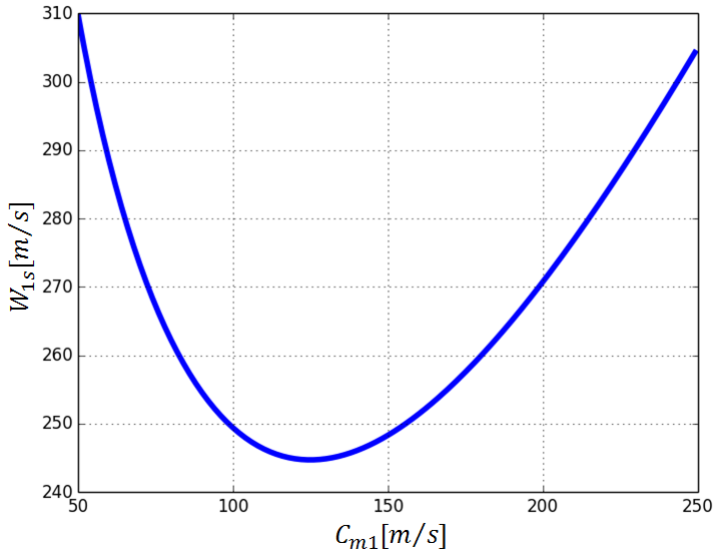

Figure 3.9: Inducer Optimization, C_{m1} vs. W_{1s}

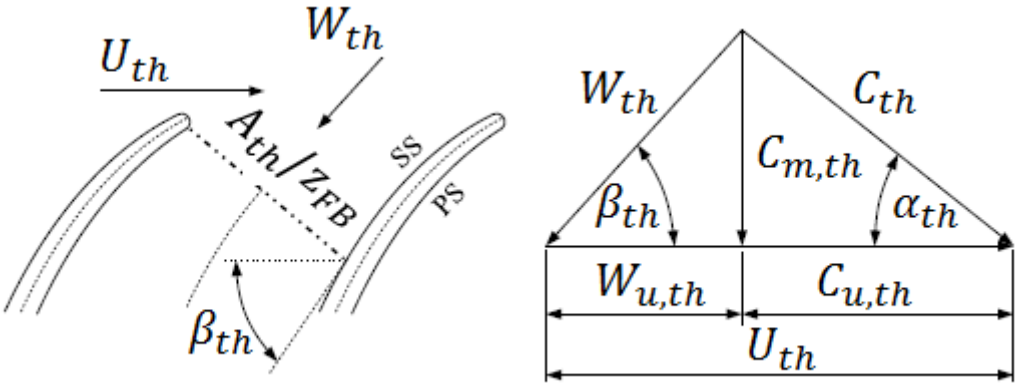

Figure 3.10: Throat velocity triangle [19]

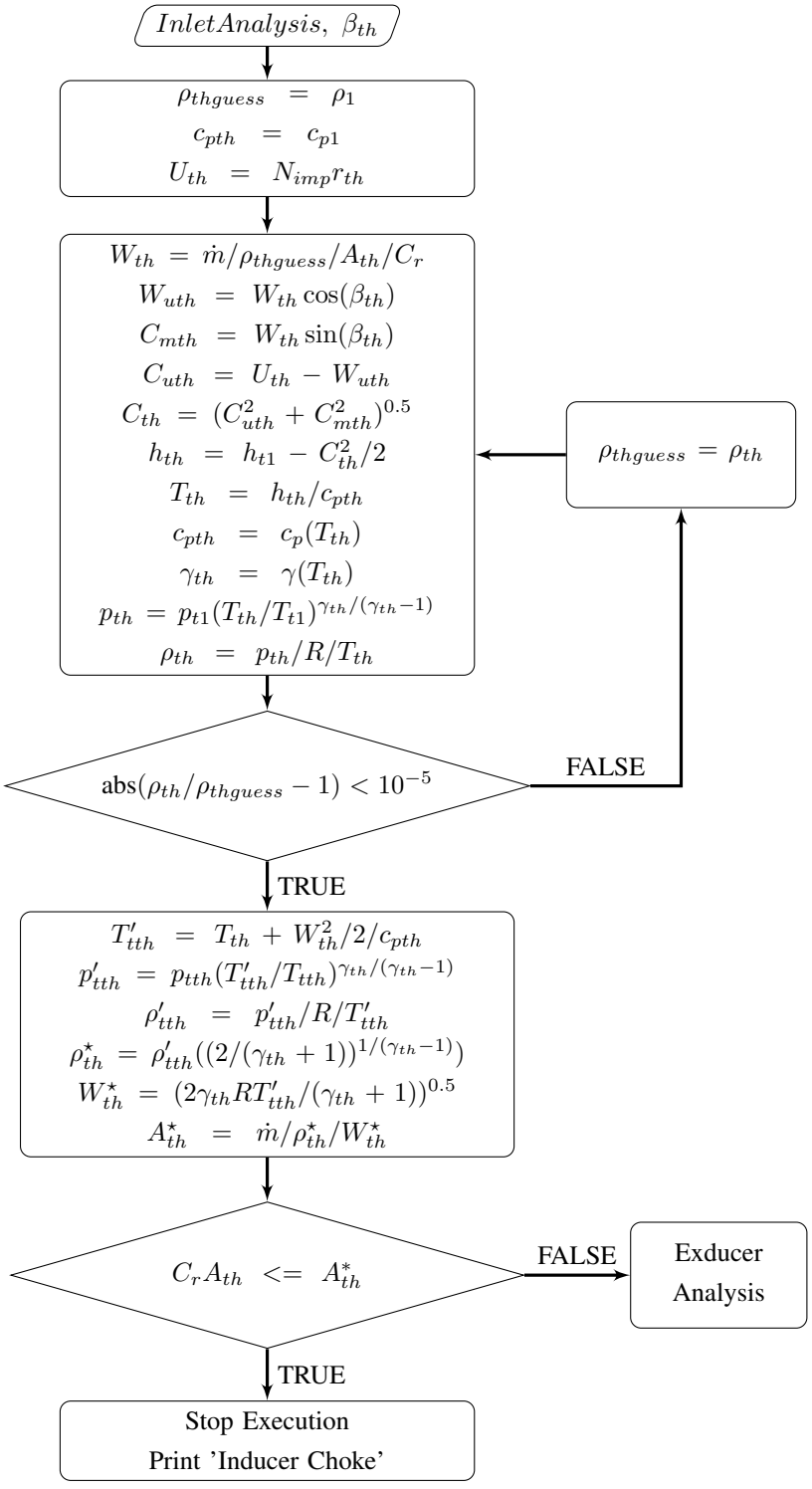

Figure 3.11: Throat Calculations

3.1.6 Parasitic (External) Loss Models

Power consumed by the compressor that is not doing any useful work is called parasitic loss and the main components of parasitic loss are disk friction loss, leakage loss and recirculation loss as mentioned in Section 3.1.

Leakage and disk friction losses are both dependent upon the flow in the clearance gaps. Aungier [13] provides a clearance gap flow model which can be used to calculate these parasitic losses for both open and closed impellers. Parts of the analysis relevant to the closed impellers are omitted since closed impellers are outside the scope of this thesis.

The flow through the clearance gap is created by the pressure difference between the two sides of an impeller blade which must be balanced by the impeller torque. Therefore, the average pressure difference across the clearance gap can be estimated by,

$$\Delta p_{CL} = \frac{\dot{m}(r_2 C_{u2} - r_1 C_{u1})}{z \bar{r} \bar{b} L} \tag{3.25}$$

where $\bar{r} = (r_1 + r_2)/2$ and $\bar{b} = (b_1 + b_2)/2$. The leakage flow undergoes a sudden contraction followed by a sudden expansion across the clearance gap and the velocity of the clearance gap flow can be estimated by assuming a throttling coefficient of 0.816. Density is also assumed constant and equal to the value at the impeller tip [13]. Therefore,

$$U_{CL} = 0.816 (\frac{2\Delta p_{CL}}{\rho_2})^{0.5} \tag{3.26}$$

Then, the mass flow through the clearance gap is given by,

$$\dot{m}_{CL} = \rho_2 z s_{CL} L_{FB} U_{CL} \tag{3.27}$$

Using these clearance gap flow calculations, Aungier [13] provides the following empirical formula for the leakage loss,

$$I_L = \frac{\dot{m}_{CL} U_{CL}}{2 \dot{m} U_2} \tag{3.28}$$

Disk friction loss model presented in Aungier [13] follows the work of Daily and Nece [34, 35]. They consider four different flow regimes with four different torque

coefficients as shown in Table 3.2. The Reynolds number, Re_{C_M}, used in these coefficients is defined by,

$$Re_{C_M} = \frac{\rho_2 \omega r_2^2}{\mu_2} \tag{3.29}$$

The true flow regime is represented by the torque coefficient having the largest value, that is,

$$C_{M0} = \max(C_{M1}, C_{M2}, C_{M3}, C_{M4}) \tag{3.30}$$

Aungier [13] applies some empirical corrections to the Daily and Nece torque coefficient, C_{M0}, as,

$$C_{MD} = \frac{0.75\, C_{M0}(1-K)^2}{(1-K_0)^2} \tag{3.31}$$

where $K = C_{u2}/U_2$ and $K_0 = 0.46/(1 + 2s_D/d_2)$. Therefore, the work input coefficient associated with disk friction is,

$$I_{DF} = \frac{C_{MD}\rho_2 U_2 r_2^2}{2\dot{m}} \tag{3.32}$$

Recirculation losses are dominant for the impellers with excessive blade loading. To be able to evaluate the blade loading, Aungier [13] uses the diffusion ratio definition given in Equation (2.21) as,

$$D_{eq} = \frac{W_{max}}{W_2} \tag{3.33}$$

where $W_{max} = (W_1 + W_2 + \Delta W)/2$. The average blade velocity difference, ΔW, is computed by,

$$\Delta W = \frac{2\pi d_2 U_2 I_B}{z L_B} \tag{3.34}$$

Lieblein [36, 37] accepted $D_{eq} > 2$ as the blade stall limit for the axial machines and Aungier [13] found $D_{eq} > 2$ to be an appropriate limit for the radial impellers as well. If this limit is exceeded, a recirculation work input coefficient is computed from,

$$I_R = (\frac{D_{eq}}{2} - 1)(\frac{W_{U2}}{C_{m2}} - 2\cot\beta_2) \tag{3.35}$$

3.1.7 Impeller Internal Losses

Besides the parasitic losses, blade work input is also compromised by the internal losses. The internal loss models for the impeller used in thesis include:

Table 3.2: Daily and Nece Torque Coefficients [13]

C_{M1}	Laminar, merged boundary layers	$2\pi/[(s_d/r_2)Re_{C_M}]$
C_{M2}	Laminar, separate boundary layers	$3.7(s_d/r_2)^{0.1}/Re_{C_M}^{0.5}$
C_{M3}	Turbulent, merged boundary layers	$0.08/[(s_d/r_2)^{1/6}Re_{C_M}^{1/4}]$
C_{M4}	Turbulent, separate boundary layers	$0.102(s_d/r_2)^{0.1}/Re_{C_M}^{0.2}$

(i) Inlet Bow Shock Loss

(ii) Incidence Loss

(iii) Entrance Diffusion Loss

(iv) Choking Loss

(v) Skin Friction Loss

(vi) Blade to Blade Loading Loss

(vii) Hub-to-Shroud Loading Loss

(viii) Abrupt Expansion Loss

(ix) Wake Mixing Loss

(x) Clearance Gap Leakage Loss

(xi) Super-critical Mach Loss

When the inlet velocity exceeds sonic conditions ($M_1' > 1$), inlet bow shock loss is calculated by a normal shock assumption at the inlet [38]. It is given by,

$$\bar{\omega}_{SH} = 1 - (\frac{W_{th}}{W_1})^2 - \frac{2}{(\gamma-1)M_1'^2}[(\frac{p_{th}}{p_1})^{\frac{\gamma-1}{\gamma}} - 1] \tag{3.36}$$

The deviation between the relative flow angle and the blade inlet angle creates the incidence loss [13] since the fluid has to change its direction suddenly. It can be computed from,

$$\bar{\omega}_{INC} = 0.8(1 - \frac{C_{m1}}{W_1 \sin\beta_1})^2 + (\frac{z_{FB}t_{b1}}{2\pi r_1 \sin\beta_1})^2 \tag{3.37}$$

Equation 3.37 can be applied at the hub, mean and shroud stream surfaces and a weighted average of these values , where the mean value is weighted 10 times as heavy as the hub and shroud values, is accepted as the incidence loss.

Entrance diffusion loss [13] is due to the flow diffusion from blade inlet to throat and it can be computed as,

$$\bar{\omega}_{DIF} = 0.8(1 - \frac{W_{th}}{W_1})^2 - \bar{\omega}_{INC}; \quad \bar{\omega}_{DIF} \geq 0.0 \tag{3.38}$$

The excessive flow diffusion between the inlet and throat can cause inducer stall and the inducer stall criterion (ISC) [13] is given by,

$$ISC = \frac{W_{1s}}{W_{th}} \geq 1.75 \tag{3.39}$$

If this criterion is exceeded, the diffusion loss [13] is limited by,

$$\bar{\omega}_{DIF} \geq (\frac{W_{1s} - 1.75W_{th}}{W_1})^2 - \bar{\omega}_{INC} \tag{3.40}$$

As the throat Mach number approaches unity, choking loss [13] is calculated by,

$$\bar{\omega}_{CH} = 0.5(0.05X + X^7); \quad X > 0 \tag{3.41}$$

where X is the choke trigger and it is calculated by,

$$X = 11 - \frac{10C_r A_{th}}{A^\star} \tag{3.42}$$

Skin friction loss [13] due to the adhesive forces between the channel surfaces and fluid is calculated from,

$$\bar{\omega}_{SF} = 4c_f(\frac{\bar{W}}{W_1})^2 \frac{L_B}{d_H} \tag{3.43}$$

where $\bar{W^2} = \max[(W_1^2 + W_2^2)/2, (W_{th}^2 + W_2^2)/2]$. Average of the throat and tip values are employed to calculate the hydraulic diamater, d_H, and the skin friction coefficient, c_f. Skin friction coefficient is obtained from generalized pipe friction data given in Appendix A and it is correlated as a function of Reynolds number based on pipe diameter, $Re = \rho V d/\mu$. Hydraulic diameter calculation is also included in Appendix A.

Blade-to-blade and hub-to-shroud pressure gradients cause momentum losses due to boundary layer build-up on the blade surfaces. The blade-to-blade loading loss [13] is given by,

$$\bar{\omega}_{BL} = \frac{1}{24}(\frac{\Delta W}{W_1})^2 \tag{3.44}$$

where ΔW given by Equation (3.34). The hub-to-shroud loading loss [13] is given by,

$$\bar{\omega}_{HS} = \frac{1}{6}(\frac{\bar{\kappa}_m \bar{b} \bar{W}}{W_1})^2 \tag{3.45}$$

where $\bar{\kappa}_m = (\alpha_{c2} - \alpha_{c1})/L$, $\bar{b} = (b_1 + b_2)/2$ and $\bar{W} = (W_1 + W_2)/2$. High aerodynamic blockage is often encountered at the impeller exit since the flow has diffused substantially within the impeller. This results in a flow regime with two separate zones; high momentum core flow (jet) and low momentum wake flow (wake). This idea of two-zone flow is further explained in Section 3.1.8.2. Abrupt expansion loss [13], or blockage loss, due to the impeller tip blockage is given by,

$$\bar{\omega}_{\lambda} = [\frac{(\lambda - 1)C_{m2}}{W_1}]^2 \tag{3.46}$$

Loss associated with the mixing of the jet and wake flows is calculated by estimating the velocity at which separation takes place, W_{SEP}. It is given by,

$$W_{SEP} = W_2 \text{ for } D_{eq} \leq 2 \tag{3.47}$$

$$W_{SEP} = 0.5 W_2 D_{eq} \text{ for } D_{eq} > 2 \tag{3.48}$$

where D_{eq} is the equivalent diffusion factor given in Equation (3.33). Meridional velocity before and after mixing are then calculated using W_{SEP} and conservation of mass as,

$$C_{m,wake} = (W_{SEP}^2 - W_U^2)^{0.5} \tag{3.49}$$

$$C_{m,mix} = \frac{C_{m2} A_2}{\pi d_2 b_2} \tag{3.50}$$

assuming constant gas density. Therefore, the wake mixing loss is given by,

$$\bar{\omega}_{MIX} = (\frac{C_{m,wake} - C_{m,mix}}{W_1})^2 \tag{3.51}$$

Due to the finite clearance gap between the impeller and the stationary casing, the fluid will leak from the pressure side to the suction side of the blade. Clearance gap model given in Equations (3.25), (3.26), (3.27) is used to calculate the clearance loss as,

$$\bar{\omega}_{CL} = \frac{2 \dot{m}_{CL} \Delta p_{CL}}{\dot{m} \rho_1 W_1^2} \tag{3.52}$$

Using the average of relative thermodynamic conditions at the inlet and tip in Equation (3.24), the local sonic velocity at the mid-passage, $W^{\star}$, can be calculated. Then, the inlet critical Mach number which corresponds to the onset of sonic velocity at the mid-passage suction surface is estimated by,

$$M'_{cr} = \frac{M_1 W^{\star}}{W_{max}} \tag{3.53}$$

where W_{max} is given in Equation 3.33. When this limit is exceeded, shock waves are expected to form at the mid-passage and these shocks can induce boundary layer separations. Therefore, the super-critical Mach number loss can be estimated by,

$$\bar{\omega}_{CR} = 0.4[\frac{(M'_1 - M'_{CR})W_{max}}{W_1}]^2 \tag{3.54}$$

3.1.8 Exducer Analysis

There are two widely used options to model the impeller for the meanline analysis: one zone model and two zone model. One zone model analyses the impeller flow as a whole while two zone model divides it into two separate regions of different characteristics. One zone model completely relies on empirical models while two zone model is more physical based. Both methods are explained and compared in the following sections.

3.1.8.1 One Zone Model

The one zone model employs 1-D flow equations along with empirical flow and loss models through a mean streamline. The mean streamline corresponds to an average annulus area location. Typically, this corresponds to the radii defined by the rms of the corresponding hub and shroud radii. Empirical correlations are used for the estimation of slip factor, external losses and internal losses, given in the previous sections. These correlations require velocity and thermodynamic property information from the inlet, throat and tip of the impeller along with the geometrical input. Since the tip information is unavailable at the beginning of the analysis, the one zone model is an iterative procedure. The flow chart of this procedure is given in Figure 3.12.

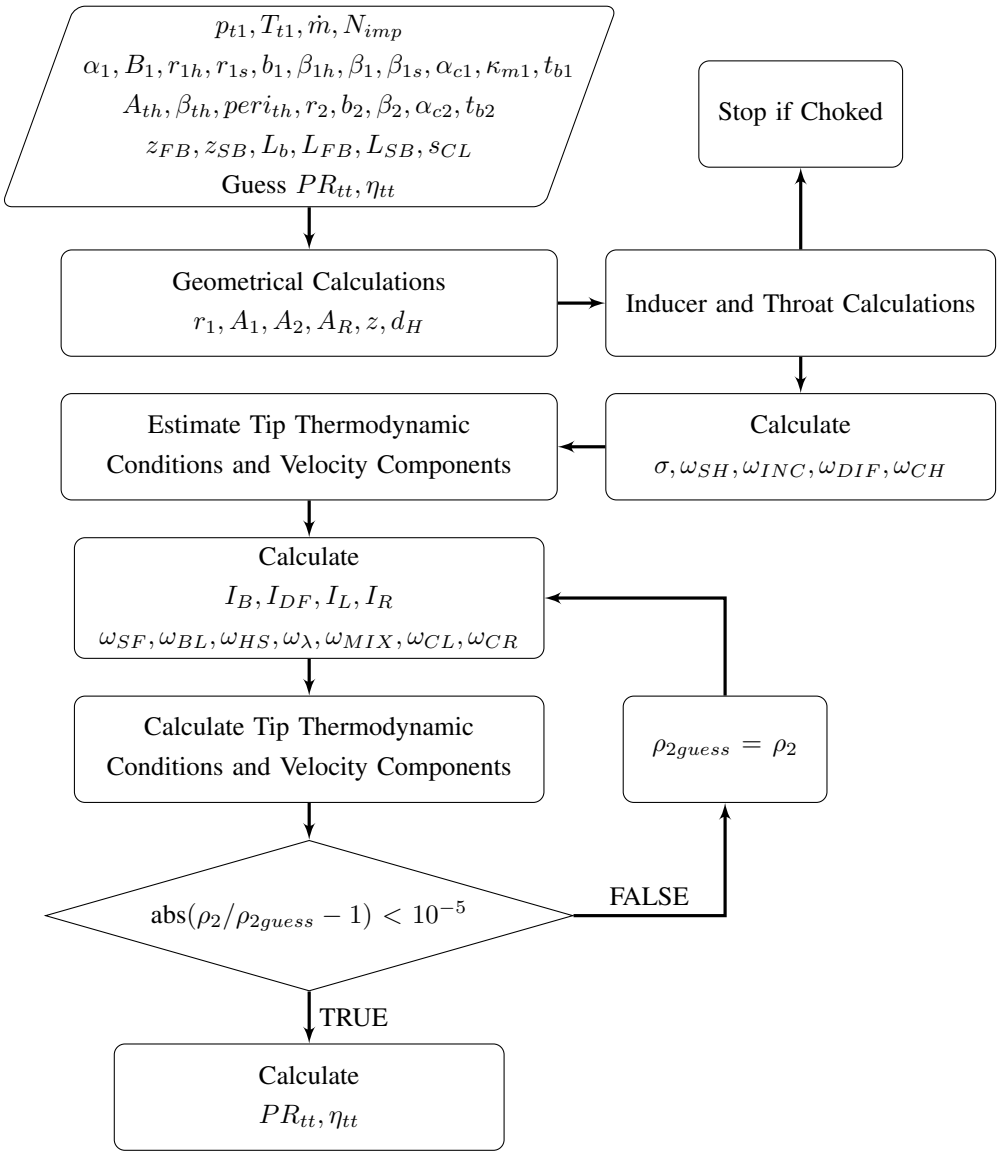

Figure 3.12: One Zone Model Procedure

First, some geometrical parameters should be calculated. They are defined in the previous sections. Second, inducer and throat is analyzed and the execution of the program is terminated if choking occurs at the inducer throat. Third, estimation of the slip factor and calculation of the losses which do not depend on the impeller tip state is done. These losses include inlet bow shock loss, incidence loss, entrance diffusion loss and choking loss. Next, estimation of the impeller tip conditions based on the initial pressure ratio and efficiency assumption. The flowchart given in Figure 3.13 can be used for this purpose. Then, work input coefficients and loss coefficients which depend on the impeller inlet, throat and tip states are computed. Employing these coefficients, impeller tip state can be obtained and iterated until the impeller tip density converges. Finally, necessary post-processing is done and the component characteristics are obtained.

Impeller tip state is calculated as follows. Since rothalpy is conserved within the impeller, ideal relative total enthalpy at the impeller tip is,

$$h'_{t2id} = h'_{t1} + 0.5(U_2^2 - U_1^2) \tag{3.55}$$

employing Equation (2.10). The deviation of the actual relative total enthalpy from the ideal one is due to the parasitic loss components. Then, the ideal relative total temperature and pressure are,

$$T'_{t2id} = \frac{h'_{t2id}}{c_{p2}} \tag{3.56}$$

$$p'_{t2id} = p_{t1}(\frac{T'_{t2id}}{T_{t1}})^{\gamma_2/(\gamma_2-1)} \tag{3.57}$$

These ideal conditions can be corrected to actual ones employing the total loss coefficient as,

$$p'_{t2} = p'_{t2id} - f_c(p'_{t1} - p_1)\bar{\omega}_{tot} \tag{3.58}$$

where f_c is a correction factor due to the fact that loss coefficients are based on inlet dynamic pressure while they are applied at the impeller tip. It is defined as,

$$f_c = \frac{p'_{t2}}{p'_{t1}} \tag{3.59}$$

At this point, it is useful to note that these calculations may require impeller tip conditions and the values from the previous iteration are used if they are not updated

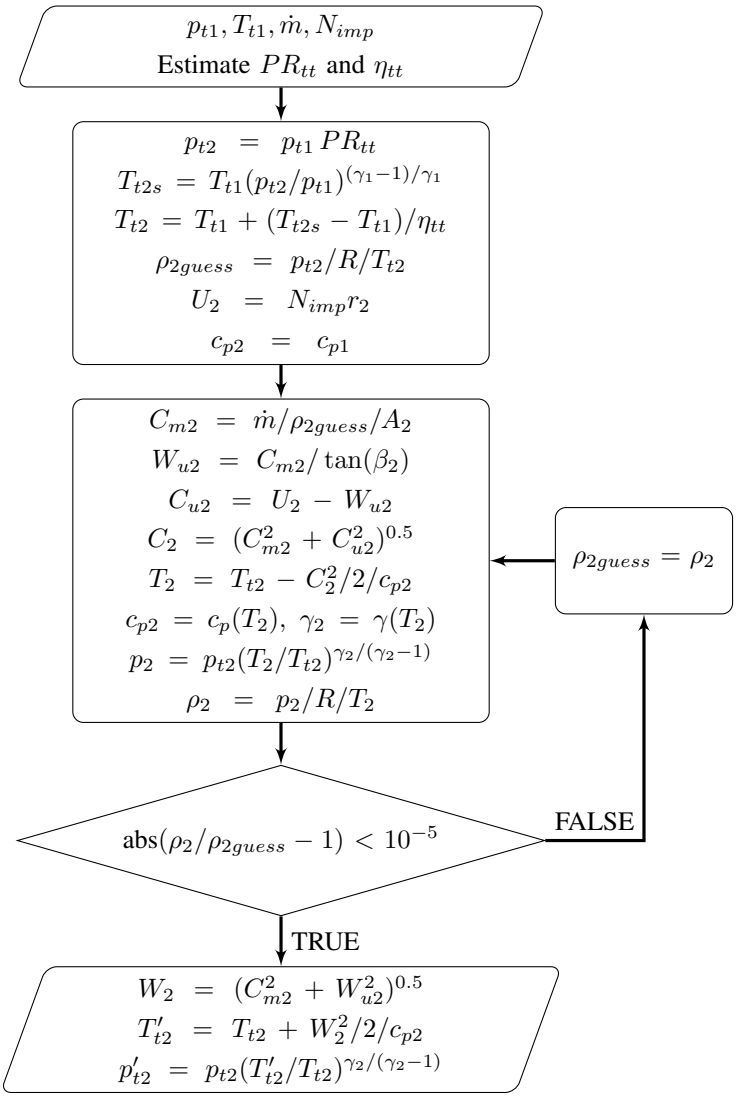

Figure 3.13: Impeller Tip Conditions Estimation Procedure

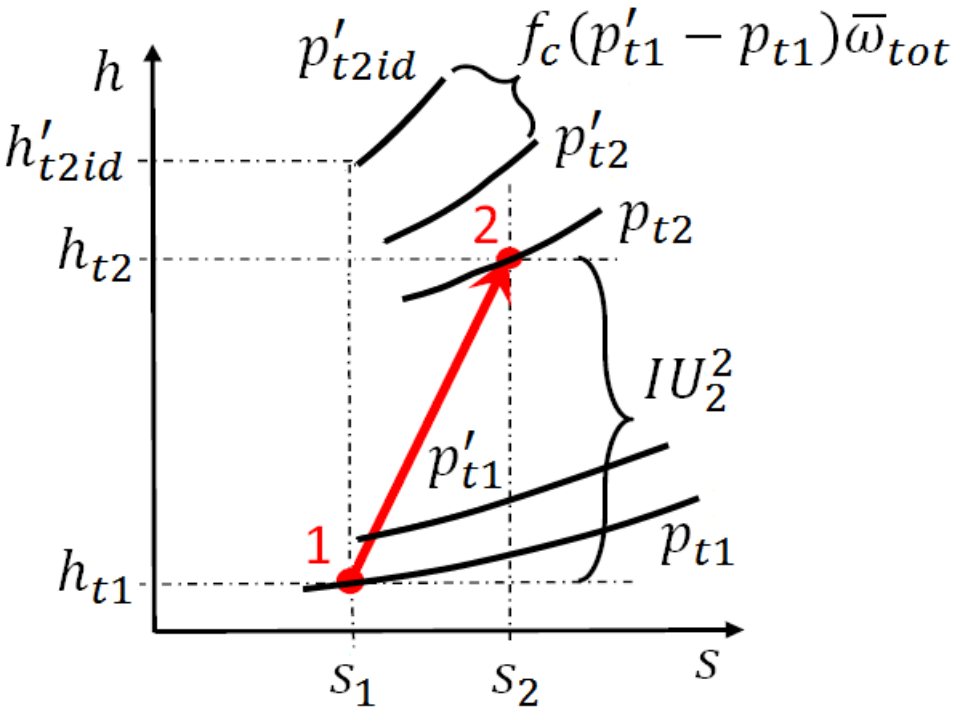

Figure 3.14: Impeller $h - s$ diagram

yet. Rest of the impeller tip conditions are calculated by employing total work input coefficient, I, as,

$$h_{t2} = h_{t1} + IU_2^2 \tag{3.60}$$

along with the basic thermodynamic relations. Impeller $h - s$ diagram is given in Figure 3.14. Velocity components can be calculated by using the definition of blade work input as,

$$C_{u2} = I_B U_2 + \frac{U_1 C_{u1}}{U_2} \tag{3.61}$$

3.1.8.2 Two Zone Model

The two zone model of Japikse [4] is based on the jet and wake model of Eckardt [16], which divides the flow within the impeller into two regions, namely jet (primary) and wake (secondary) regions. It is experimentally verified that the jet flow is nearly isentropic while wake flow contains all the flow losses. It is also verified that the wake flow has a very low momentum compared to the jet flow as shown in Figure

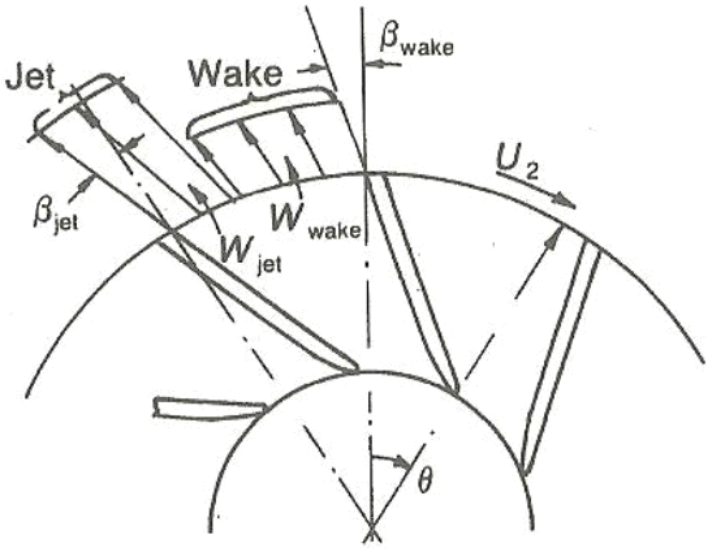

Figure 3.15: Jet and Wake Model [15]

3.15 [4]. The flowchart of two-zone modeling used in this thesis is given in Figure 3.16.

Two zone model employs Two-Element-in-Series (TEIS) model to estimate the diffusion in the primary zone. The TEIS model considers the impeller as a rotating diffuser, consists of two elements as shown in Figure 3.17. The first element, element "a", is the the inlet portion from the impeller inlet to the impeller throat. The second element, element "b", is the passage portion from the impeller throat to the impeller exit. The diffusion within these elements can be modeled very easily by treating them as a diffuser with constant effectiveness [4]. Therefore, the diffusion ratio is calculated as,

$$DR^2 = (\frac{W_{1s}}{W_{2j}})^2 = \frac{1}{1-\eta_a C_{pai}} \frac{1}{1-\eta_b C_{pbi}} \tag{3.62}$$

where C_{pai} and C_{pbi} are pressure recovery coefficients and they are defined as,

$$C_{pai} = 1 - (\frac{\sin \alpha'_{1s}}{\sin \beta_{1s}})^2 \tag{3.63}$$

$$C_{pbi} = 1 - (\frac{A_{th}}{A_e})^2 \tag{3.64}$$

where $A_e \approx A_2 \sin \beta_2$. Critical DR values that can cause impeller stall are given in Table 3.3. The parameters, η_a and η_b, are the diffusion effectiveness values. They

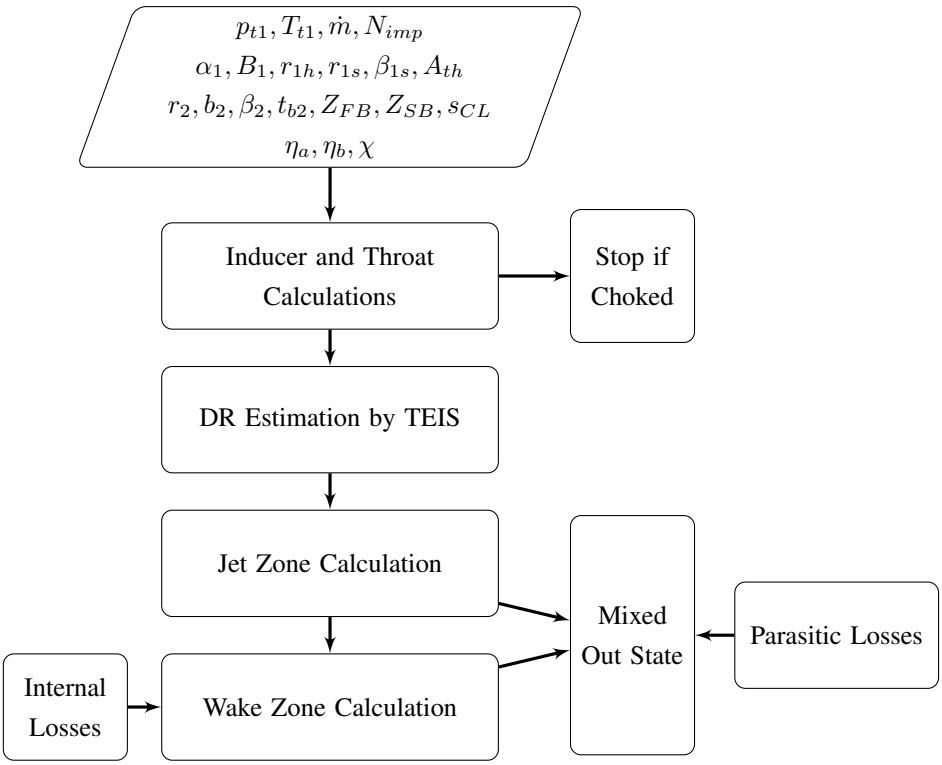

Figure 3.16: Two Zone Model Procedure

are taken as constants for the primitive TEIS model and suggested values of them are given in Table 3.3. In reality, however, these parameters are not constants and depend on impeller passage geometry and operating conditions. [4] Besides diffusion ratio, two zone model also requires two other parameters to be specified. These parameters are the secondary flow mass fraction, χ, and deviation of primary flow at the impeller tip, δ_{2j}. χ is generally assumed constant and suggested values by Japikse [4] are given in Table 3.3. It can also be defined as a function of ϵ, the secondary flow area fraction.

Table 3.3: Suggested Values for Primitive TEIS [4]

Case	η_a	η_b	DR_{stall}	χ
Large(>10"-12"D), well design	0.9-1.1	0.4-0.6	1.5-1.8	0.1-0.2
Medium size(4"-10"D), well design	0.8-0.9	0.3-0.5	1.3-1.6	0.15-0.25
Medium size(4"-10"D), ordinary design	0.6-0.8	0.0-0.4	1.2-1.5	0.2-0.3
Small(<4"D) or poor design	0.4-0.6	-0.3-0.3	1.1-1.4	0.25-0.35

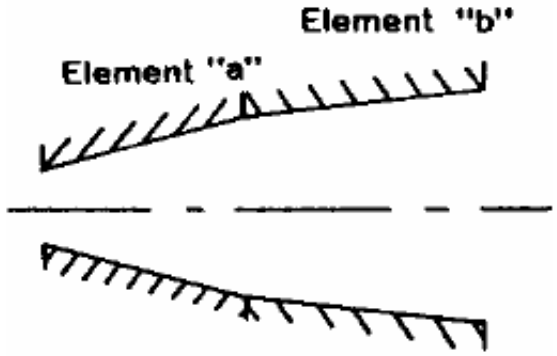

Figure 3.17: TEIS Conceptual Model [4]

They are defined as,

$$\chi = \frac{\dot{m}_w}{\dot{m}} \tag{3.65}$$

$$\epsilon = \frac{A_w}{A_2} \tag{3.66}$$

The relation between these two parameters can be derived for a specific type of impeller via experimental work or CFD investigations. Japikse [4] provides this relation for Eckardt and CETI impellers respectively as,

$$\chi = \epsilon^2 \tag{3.67}$$

$$\chi = 0.5\epsilon^2 + 0.05\epsilon \tag{3.68}$$

Many correlations exist within the literature to predict the deviation of primary flow. The slip factor model of Oh et al. [39] is used for this purpose. Equation (3.13) is not used since it is derived for mixed out flow state, not for the primary flow. Combining it with the definition of slip, relative flow angle at the impeller tip for the primary flow is,

$$\beta_{2j} = \frac{\beta_2}{2} + 0.5\cos^{-1}[(11.46 * 10^{-6}\beta_2^{2.5}\frac{U_2 A_{2j}}{W_{2j} r_2 b_2 z} + \cot\beta_2)\sin\beta_2] \tag{3.69}$$

Since the relation between χ and ϵ is not available in the preliminary design phase, the iterative procedure shown in Figure 3.18 is instead used for the primary zone calculations.

Deviation of the secondary flow, δ_{2s}, is generally set to zero since it has a little effect on the overall stage performance because the secondary flow is largely tangential [40].

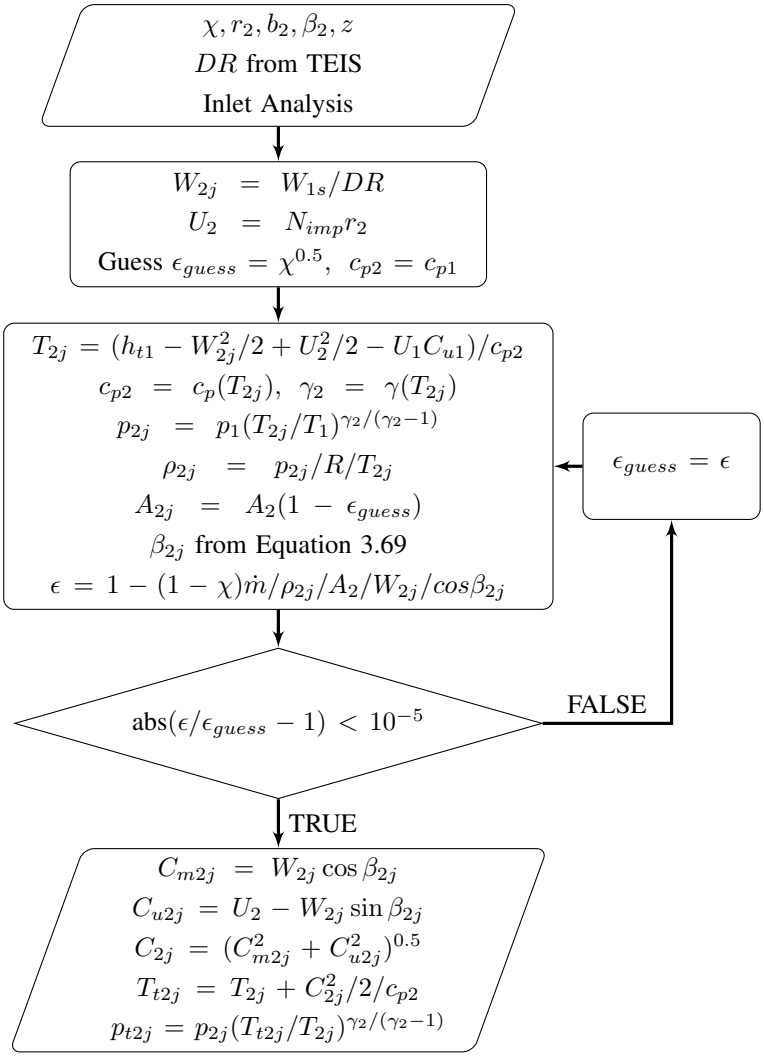

Figure 3.18: Jet Zone Calculations

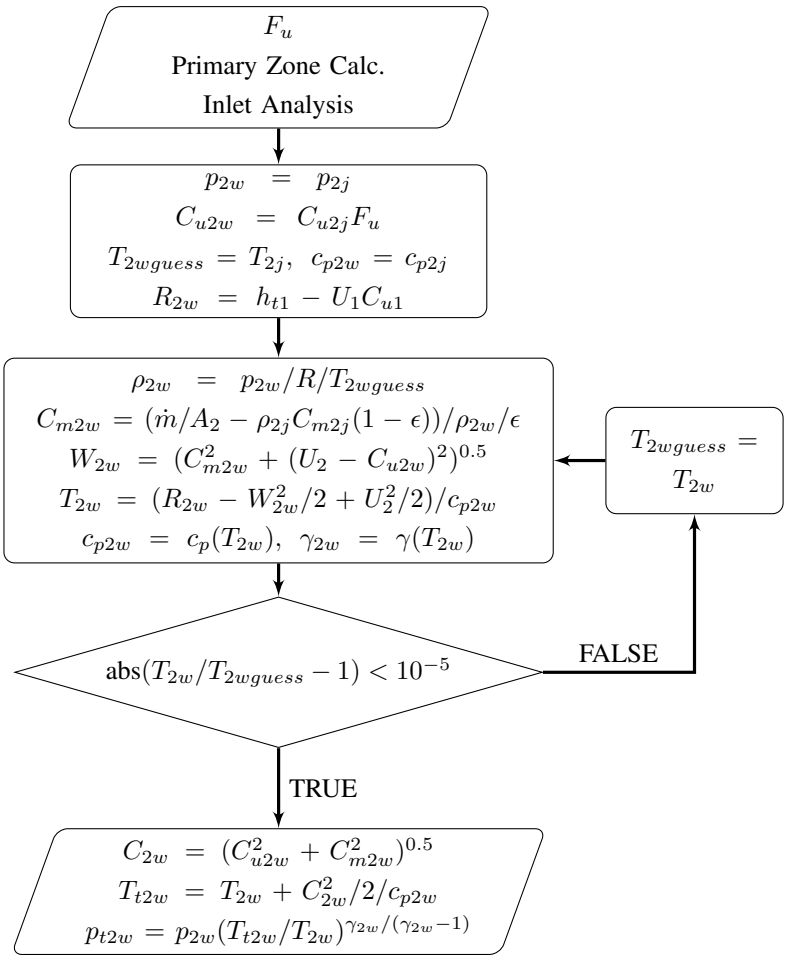

Figure 3.19: Wake Zone Calculations

However, a tangential velocity factor is used in this thesis to account for δ_{2s} [31]. It is defined as,

$$F_u = \frac{C_{u2w}}{C_{u2j}} \tag{3.70}$$

The recommended range for this parameter is 0.92 to 0.94.

The secondary flow static pressure can be equated to that of primary flow to account for the flow losses. This is often referred to as unloaded tip condition. A set of loss correlations can also be employed instead. Usage of unloaded tip condition is preferred in this thesis due to its simplicity. The iterative procedure shown in Figure 3.19 is used to calculate the wake zone conditions. Finally, mixing of primary and secondary zones at the impeller tip is modeled by assuming that this process occurs very rapidly after the flow leaves the impeller. One-dimensional energy, momentum and continuity equations are solved at the impeller tip to calculate the mixed-out

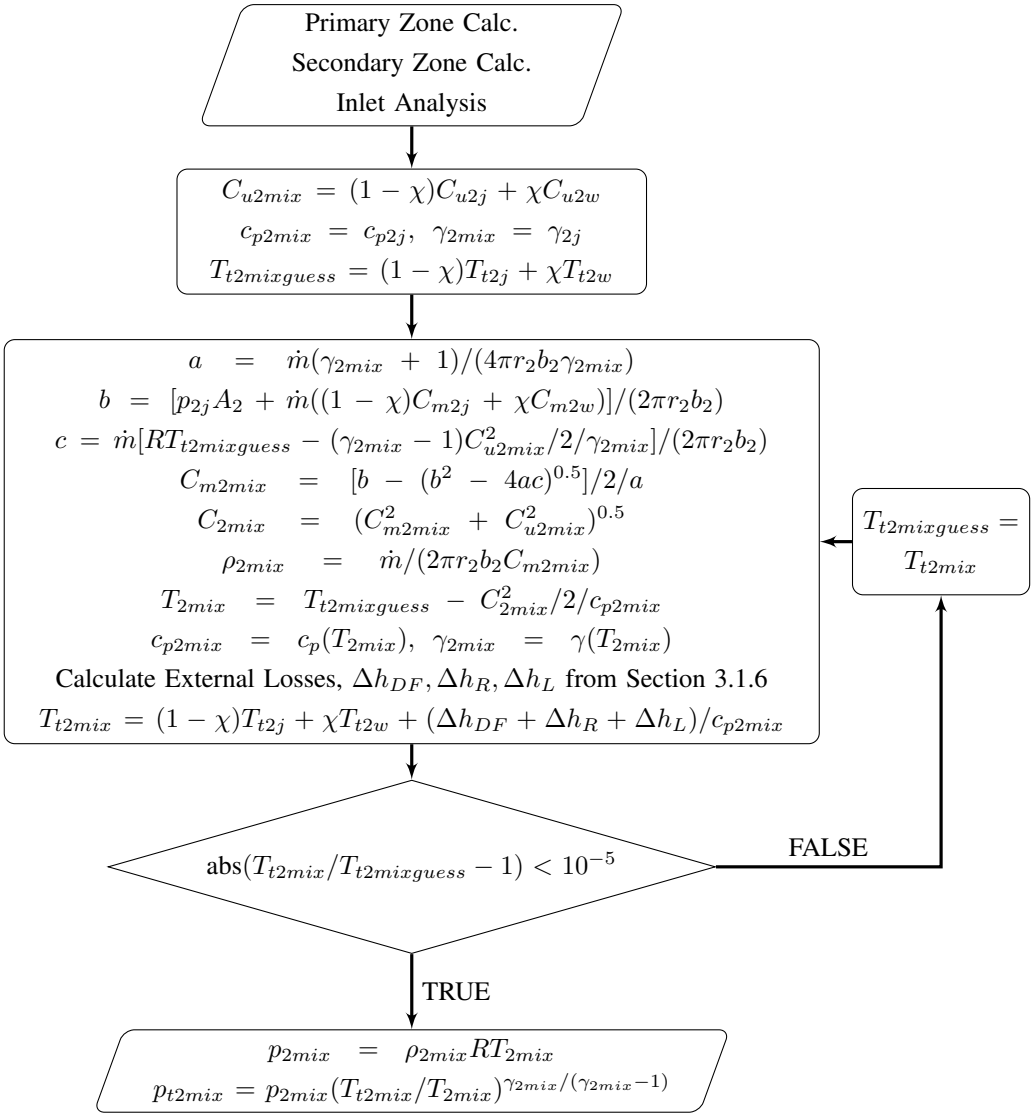

Figure 3.20: Mixed-out State Calculations [39]

state. Parasitic (external) losses are included in the energy equation to account for the enthalpy rise they impart to the flow. The flow chart of the calculation procedure for mixed-out state is given in Figure 3.20.

3.1.8.3 Comparison of One and Two Zone Models

Two zone model employs TEIS model to predict the diffusion ratio and primitive TEIS models can predict the diffusion ratio around the design point with a good accuracy. However, it fails for the off-design points, especially for high speeds [41]. This is due to the absence of accurate and broadly applicable models for the

modeling parameters, η_a and η_b, in the open literature. Japikse [4] states that several years of additional work is required to develop an enhanced version of TEIS. One zone model of Aungier, on the other hand, has a better off-design accuracy. A comparison of one and two zone models applied to Came impeller [42] is presented in Figure 3.21.

One advantage of two zone model is that it requires fewer geometrical information than one zone model of Aungier, which makes it more practical in the preliminary design phase.

Since one zone model gives better results for off-design points and it is very well documented by Aungier [13], it is a superior option for now and it is used in this thesis for the impeller analysis.

3.1.9 Impeller Gas Path Calculations

For the above mentioned impeller calculations, some impeller gas path parameters, such as inducer throat area and meanline length, are required. These parameters are diffucult to find or assume during the preliminary design and some rough calculations are useful to estimate them. The procedure given by Herbert [12] is used for this purpose based on the following assumptions:

(i) a rotor geometry with circular arc hub and double circular arc shroud as shown in Figure 3.22

(ii) blades have constant thickness and circular arc leading edges as shown in Figure 3.23

(iii) a blade angle distribution for hub and shroud as given in Tables 3.4 and 3.5.

(iv) impeller exit is fully radial ($\alpha_{c2} = 90°$)

The functions given in Tables 3.4 and 3.5 are derived by Herbert [12] to describe the geometry of the rotor based on the hub and shroud profile assumptions mentioned above. The following functions are also employed along with these functions,

$$x = (r_2 - r_{1h})(\sec \alpha_{c1h} - \tan \alpha_{c1h}) - b_2 \tag{3.71}$$

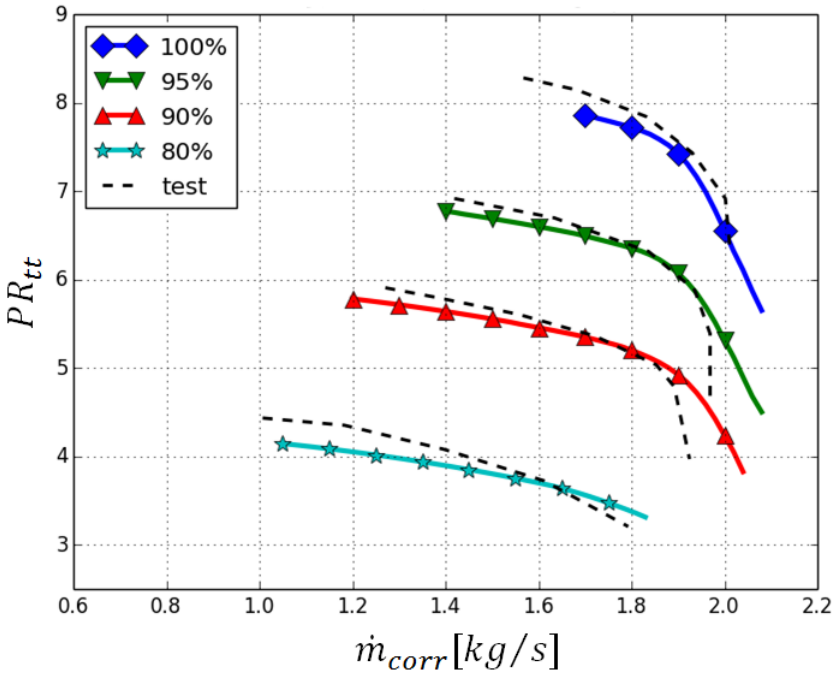

(a) One Zone Model

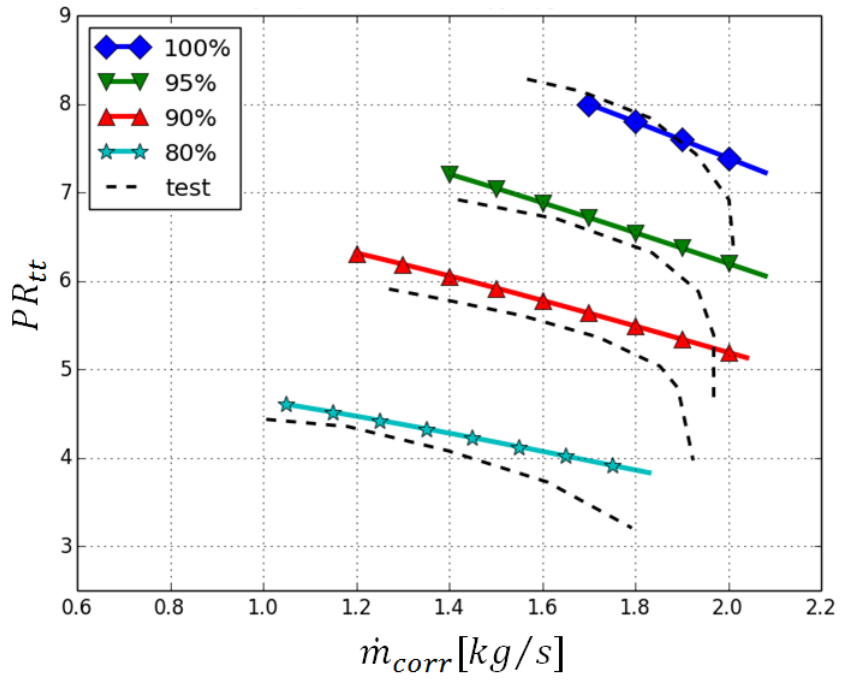

(b) Two Zone Model

Figure 3.21: Comparison of One and Two Zone Models on Came Impeller [42], Total-to-total Pressure Ratio (PR_{tt}) versus corrected mass flow rate ($\dot{m}_{corr}$), 100% = 40000rpm

$$y = r_2 - r_{1s} \tag{3.72}$$

$$\beta_{min} = \frac{\beta_2}{6}(1 + \frac{\beta_{1h}}{15}) \tag{3.73}$$

$$\frac{m_{jc}}{m_{2s}} = x + \frac{(1-\sqrt{2})y}{(2-\sqrt{2})(x+y)} \tag{3.74}$$

where m_{jc} denotes the meridional distance at the junction of two circular arcs at the shroud of the rotor.

The blade angles are measured from the meridional direction in this section, not from tangential direction as the rest of this chapter, to be consistent with the work of Herbert [12]. A simple conversion of blade angles from one system to another can be done at the beginning and end of these calculations.

Throat position at the hub and shroud are found from the blade geometry assumption shown in Figure 3.24. Some geometrical calculations on this figure results as,

$$m_\star = \frac{\pi r_1}{z_{FB}} \frac{1}{\cot\beta_a + \tan\beta_b} + \frac{t_{b1}}{2} \tag{3.75}$$

where β_a is the value of β at $m = 2m_\star - t_{b1}$ and $\beta_b = 0.5(\beta_1 + \beta_a)$. A simple iteration is needed to calculate $m_\star$ at the hub and tip since β_a and β_b are also function of $m_\star$. It should be noted that all quantities differ between hub and tip. Knowing the throat position at the hub and tip, throat position at any radius can be found by assuming that throat line is linear . Referring to Figure 3.24, it can written as,

$$m_\star(r) = m_{\star h} + (m_{\star s} - m_{\star h})\frac{r - r_{\star h}}{r_{\star s} - r_{\star h}} \tag{3.76}$$

Blade angles along the throat line is also needed for the throat area calculations and it can be calculated by assuming that $\tan\beta$ varies linearly with radius at any value of $m_\star$. That is,

$$\tan\beta(r) = \tan\beta_s(r) - (\tan\beta_s(r) - \tan\beta_h(r))\frac{r_s - r}{r_s - r_h} \tag{3.77}$$

Knowing the position of throat line and blade angle distribution along it, throat area can be calculated as,

$$A_{th} = \int_{r_{\star h}}^{r_{\star s}} (2\pi r\cos\beta(r) - z_{FB}t_\star(r))\,\mathrm{d}r \tag{3.78}$$

Table 3.4: Shroud geometry functions [12]

m_2	$\pi(x+y)/4$	
α_c	$m < m_{jc}$	$\pi m/4/m_{jc}$
	$m > m_{jc}$	$\pi(1+(m-m_{jc})/(m_{2s}-m_{jc}))/4$
r	$m < m_{jc}$	$r_{1s}+(1-\cos\alpha_c)(x+(1-\sqrt{2})y)/(2-\sqrt{2})$
	$m > m_{jc}$	$r_{1s}+(1-\cos(45°))(x+(1-\sqrt{2})y)/(2-\sqrt{2})+...$ $(\cos(45°)-\cos\alpha_c)((1-\sqrt{2})x+y)/(2-\sqrt{2})$
β	$\beta_{1s}(1-5(m/m_{2s})^2)$	

This integral can be calculated numerically using Simpson's rule, as explained in Appendix B. 10 equal intervals of r is sufficient for this calculation.

Throat radius, r_{th}, mean blade angle at the throat, β_{th}, and throat wetted perimeter, $peri_{th}$, are also required in the impeller analysis procedure. Throat radius can be assumed to be equal to the inlet radius, $r_{th} = r_1$, since throat is usually placed very close to the inlet. Knowing the blade angle distribution along the throat line, blade angle at this radius can be calculated, $\beta_{th} = \beta(r_{th})$. Throat wetted perimeter is calculated using the following formula,

$$peri_{th} = 2\pi r_{\star s}\cos\beta_{\star s} + 2\pi r_{\star h}\cos\beta_{\star h} + 2z_{FB}h_{th} - 2z_{FB}t_{b1} \tag{3.79}$$

where h_{th} is the throat line length and can be calculated as,

$$h_{th} = [(r_{\star s}-r_{\star h})^2 + (m_{\star s}-m_{\star h})^2]^{0.5} \tag{3.80}$$

Finally, the mean line meridional length, L, is calculated by the help of quasi-normals. An equal number of discrete points can be distributed along the shroud and hub curve and connecting the corresponding points with straight lines, quasi-normals are obtained. RMS radius along each quasi-normal is found first and these points are connected by linear lines along the impeller. Summing up the lengths of these small linear lines, meanline meridional length can be estimated. Accuracy of the calculation increases with the number of quasi-normal.

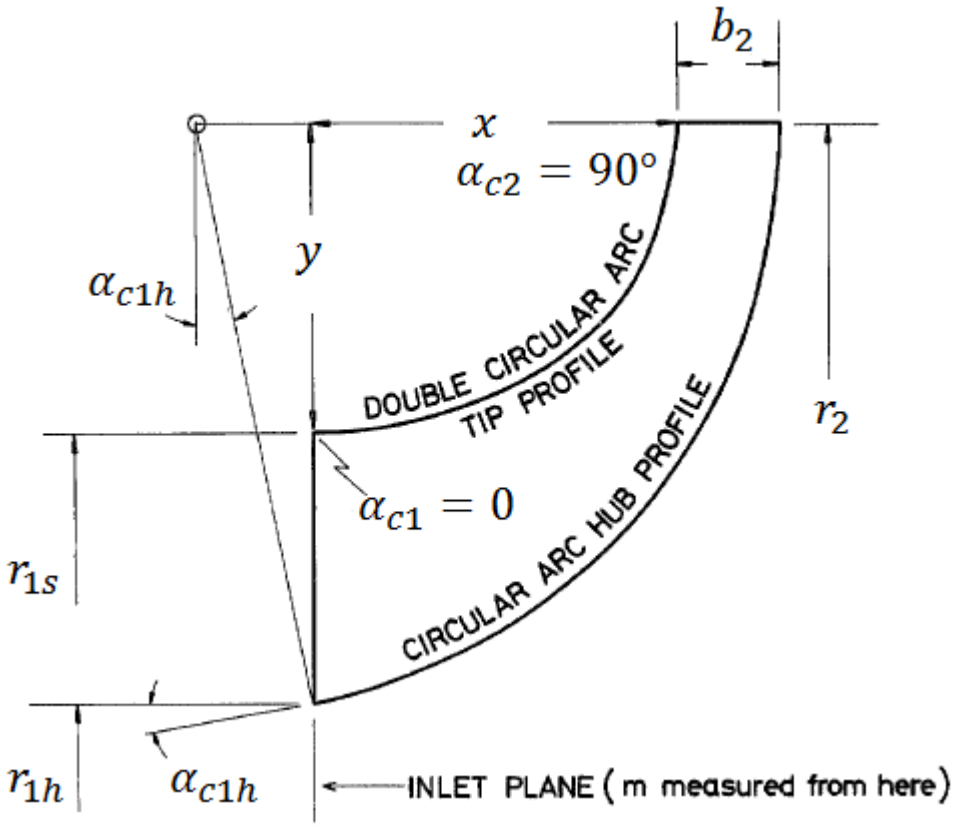

Figure 3.22: Assumed impeller geometry [12]

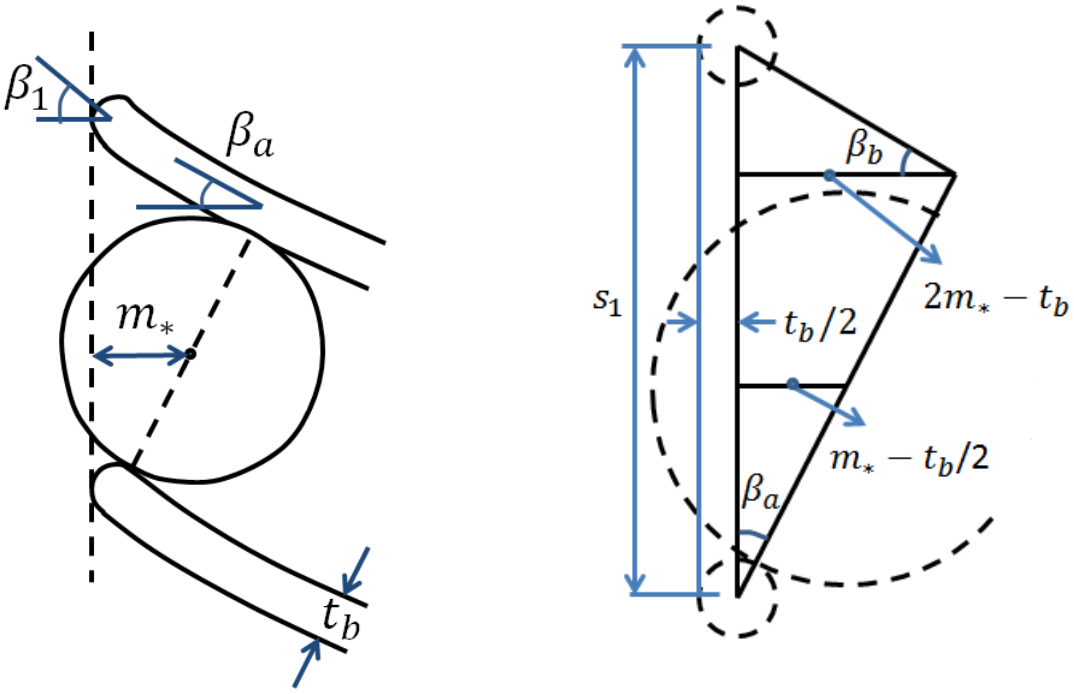

Figure 3.23: Assumed blade profile [12]

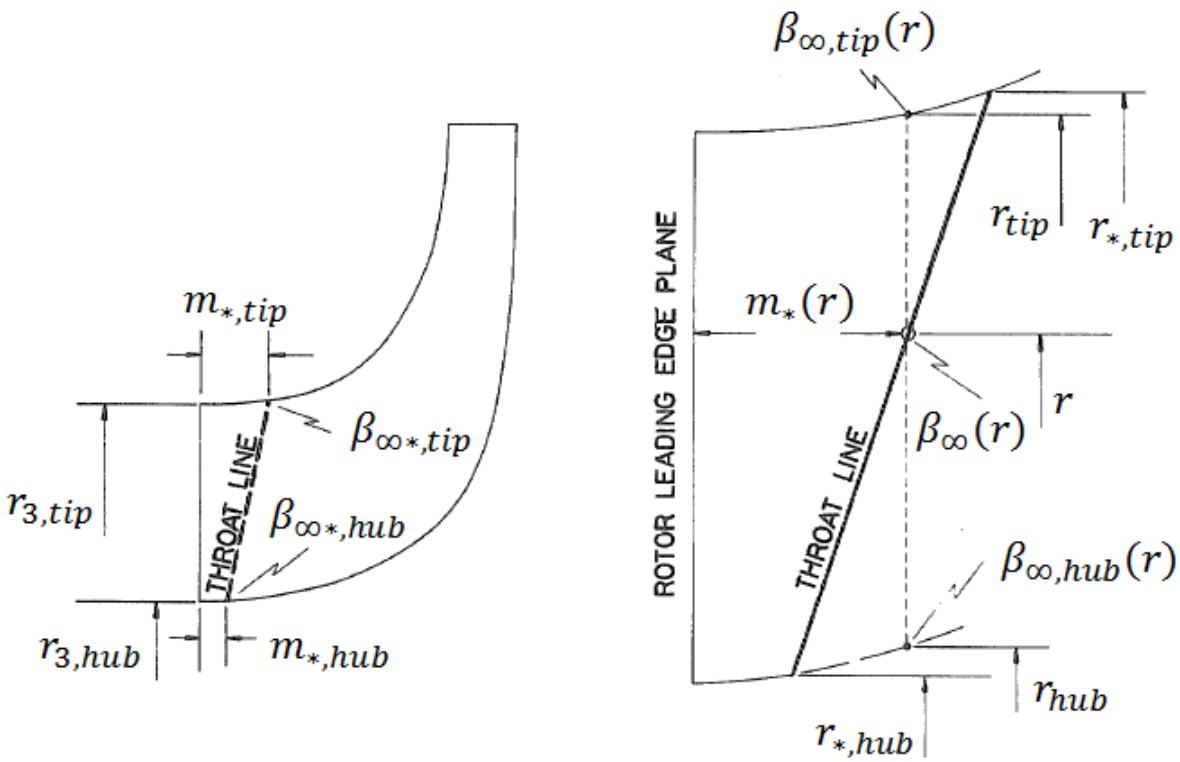

Figure 3.24: Throat Line [12]

Table 3.5: Hub geometry functions [12]

m_2	$(\pi/2 - \phi_{1h})(r_2 - r_{1h})/\cos\alpha_{c1h}$
α_c	$\alpha_{c1h} + (\pi/2 - \alpha_{c1h})m/m_{2h}$
r	$r_{1h} + (r_2 - r_{1h})(1 - \cos\phi/\cos\alpha_{c1h})$
β	$\beta_{1h} - 4(\beta_{1h} - \beta_{min})(m/m_{2h})(1 - m/m_{2h})$

3.1.10 Preliminary Impeller Sizing

Aungier [13] provides some useful correlations for the preliminary sizing of the impeller as a function of stage flow coefficient, $\phi = \dot{m}/(\rho_{1t}\pi r_2^2 U_2)$. Only the relations given for open impellers are included here. They are given by,

$$I = 0.68 - (\frac{\phi}{0.37})^3 + \frac{0.002}{\phi} \tag{3.81}$$

$$\mu_{p,VD} = 0.59 + 0.7\phi - 7.5\phi^2 - \frac{0.00025}{\phi} \tag{3.82}$$

$$\eta_{p,VLD} = \eta_{p,VD} - \frac{0.017}{0.04 + 5\phi + \eta_{p,VD}^3} \tag{3.83}$$

$$I_{par} = \frac{0.002}{\phi} \tag{3.84}$$

$$\alpha_{2,VLD} = \text{atan}(0.26 + 3\phi) \tag{3.85}$$

$$\alpha_{2,VD} = 18 + 0.5\text{ln}\phi + 585\phi^2 \tag{3.86}$$

$$\Delta z_I = 0.014 + 0.023\frac{d_2}{d_{0h}} + 1.58\phi \tag{3.87}$$

noting that $\mu = \eta I$. Therefore impeller blade work input coefficient is,

$$I_B = I - I_{par} = \frac{C_{u2}}{U_2} \tag{3.88}$$

assuming that there is no inlet swirl.

Employing the inducer optimization algorithm and the gas path calculation procedure mentioned above along with these empirical correlations enables us to create a preliminary impeller geometry. The procedure given by Figure 3.26 is followed in this thesis. During these calculations, a blade loading parameter is defined and limited to a certain value as,

$$\frac{2\Delta W}{W_1 + W_2} \leq 0.9 \tag{3.89}$$

where ΔW is given by Equation (3.34). A meridional view of the obtained impeller geometry is also plotted along with its meanline and throat line, as shown in Figure 3.25.

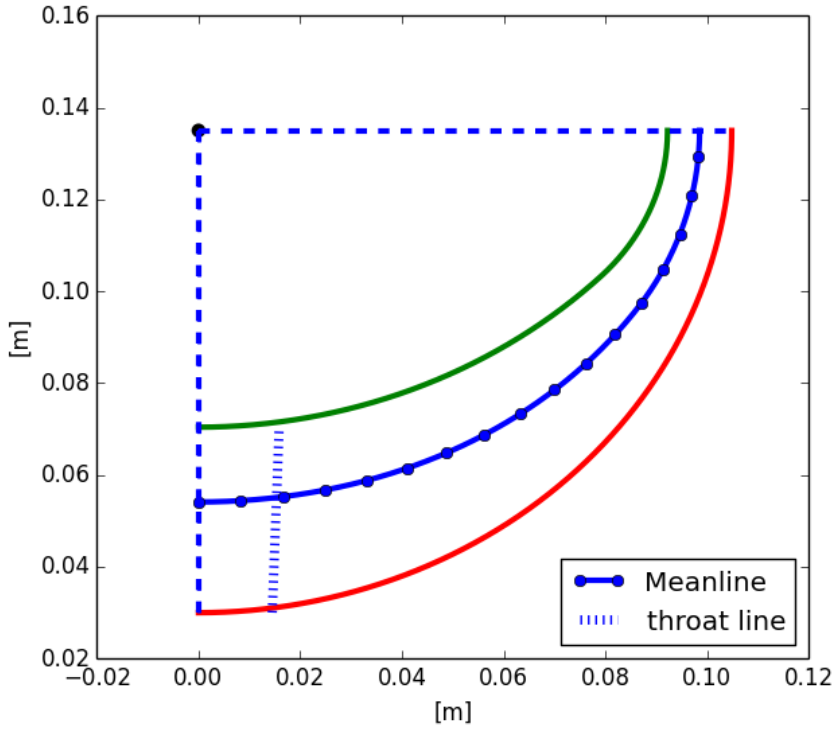

Figure 3.25: Impeller Meridional View After Impeller Sizing

3.1.11 Employing Impeller Analysis Procedure for Sizing

It is possible to employ the above analysis procedures for sizing purposes. To achieve this, the procedure given in Figure 3.27 can be employed. After specifying target performance parameters, such as pressure ratio, PR_{tar}, and swirl parameter, λ_{tar}, iterations can be carried out with the analysis procedure to obtain the sizing parameters, r_2 and b_2, which gives the desired performance. Since this problem is actually a root-finding problem, Newton-Raphson method can be used due to its fast convergence. This method is explained in Appendix B.

3.2 Vaneless Diffuser Performance

Both Aungier [13] and Stanitz [43] provide one-dimensional conservation of mass, momentum and energy equations in a form suitable for vaneless passage analysis. A boundary layer analysis along the vaneless passage is also needed to close these

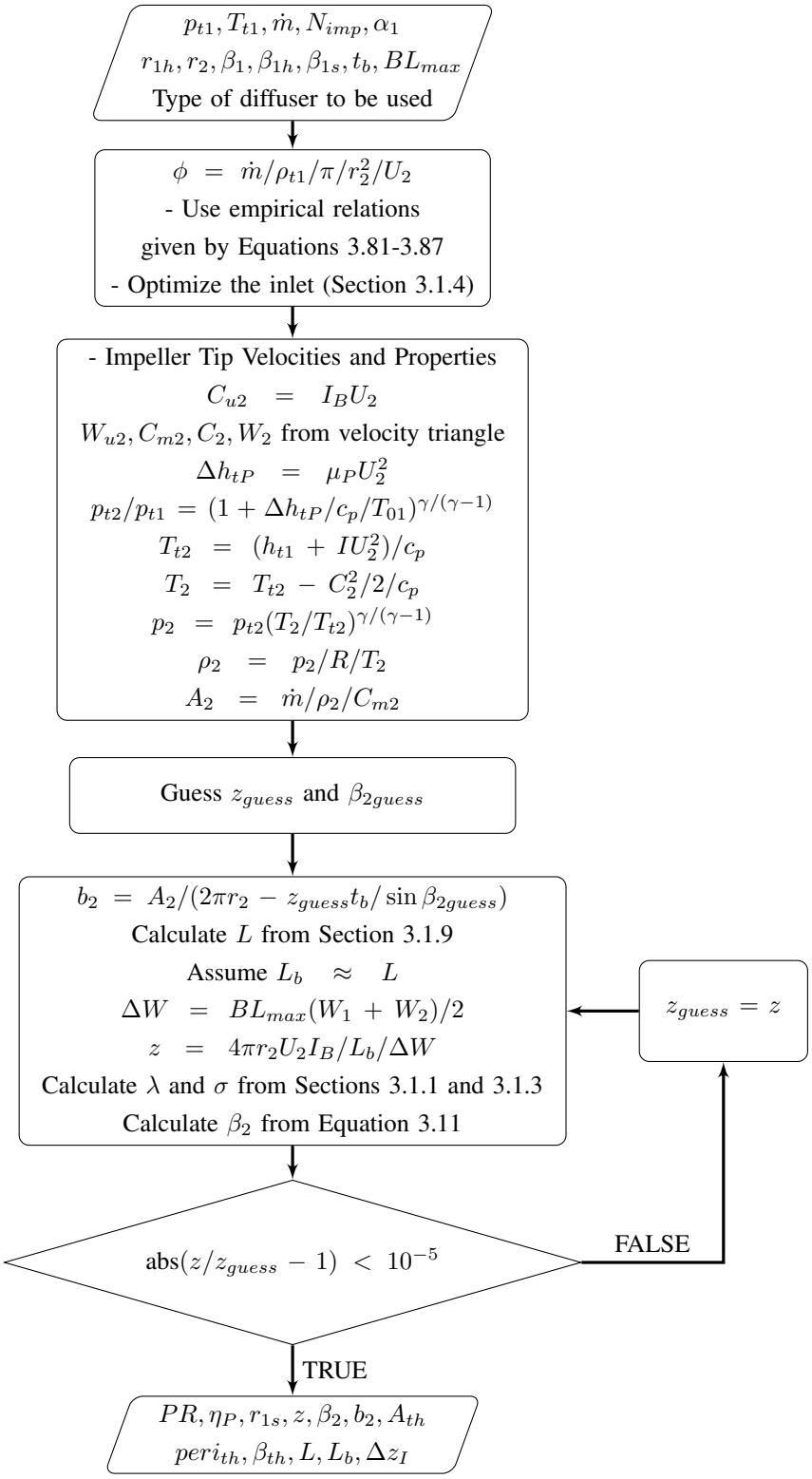

Figure 3.26: Preliminary Impeller Sizing Procedure [17]

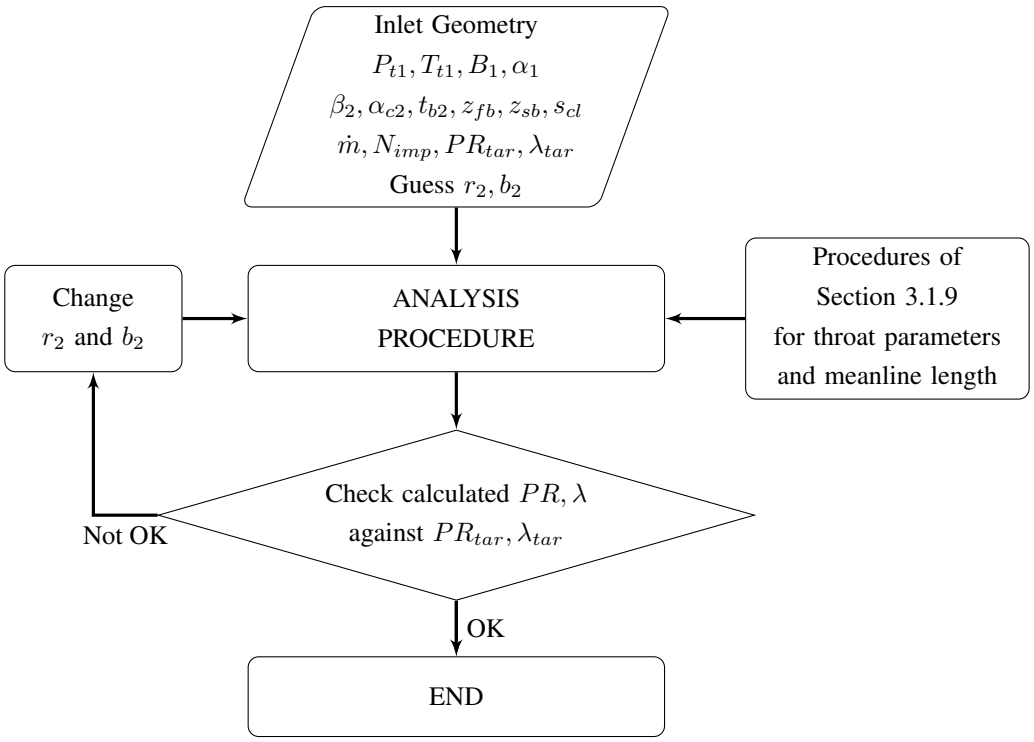

Figure 3.27: Impeller Sizing with Analysis Procedure [4]

equations. The equation set given by Aungier is preferred since it includes more loss models. He used more than 35 different compressor stage tests to developed these models. [13] It is given by,

$$2\pi r \rho b C_m (1 - B) = \dot{m} \tag{3.90}$$

$$bC_m \frac{\mathrm{d}(rC_u)}{\mathrm{d}m} = -rCC_u c_f \tag{3.91}$$

$$\frac{1}{\rho}\frac{\mathrm{d}p}{\mathrm{d}m} = \frac{C_u^2 \sin\alpha_c}{r} - C_m \frac{\mathrm{d}C_m}{\mathrm{d}m} - \frac{CC_m c_f}{b} - \frac{\mathrm{d}I_D}{\mathrm{d}m} - I_C \tag{3.92}$$

$$h_t = h + 0.5C^2 = constant \tag{3.93}$$

Last three terms of Equation (3.92) and last term of Equation (3.91) are the source terms which represents the loss contributions due to wall friction, flow diffusion and passage curvature. Aungier [13] employs the classical diffuser analogy to estimate the diffusion loss. A divergence parameter, D, is defined to identify the low loss regime. It is given as,

$$D = -\frac{b}{C}\frac{\mathrm{d}C}{\mathrm{d}m} \tag{3.94}$$

The critical value of divergence parameter below which the diffusion losses are low is given by,

$$D_m = 0.4(\frac{b_1}{L})^{0.35} \sin\alpha \tag{3.95}$$

Using this divergence parameter, the empirical diffusion efficiency is given as,

$$E = 1; \quad D \leq 0 \tag{3.96}$$

$$E = 1 - 0.2(\frac{D}{D_m})^2; \quad 0 < D < D_m \tag{3.97}$$

$$E = 0.8\sqrt{\frac{D_m}{D}}; \quad D \geq D_m \tag{3.98}$$

The diffusion term in Equation (3.92) is given by,

$$\frac{\mathrm{d}I_D}{\mathrm{d}m} = -2(p_t - p)(1 - E)\frac{1}{\rho C}\frac{\mathrm{d}C}{\mathrm{d}m} \tag{3.99}$$

Besides this streamwise diffusion loss term, an excessive meridional gradient of the vaneless passage can also lead to high losses. To check this, the maximum, stall free local area is estimated by,

$$(rb)_m = (rb)_1(1 + 0.16\frac{m}{b_1}) \tag{3.100}$$

which corresponds to a diffuser divergence angle, $2\theta_C$ of $9°$. If the local area exceeds this, a second estimate of the diffusion term is calculated by,

$$I_D = \frac{0.65(p_t - p)}{\rho}[1 - \frac{(rb)_m}{(rb)}] \tag{3.101}$$

If this value exceeds the local value obtained by integrating Equation (3.99), it is used instead.

The passage curvature term is omitted in this thesis since it has negligible effect on vaneless diffuser performance. However, if one wishes to use these equations for a vaneless passage with high curvatures, such as return bend, this terms should be included. It is given by,

$$I_C = \frac{\kappa_m(p_t - p)C_m}{13\rho C} \tag{3.102}$$

The area blockage and skin friction factor coefficient along the vaneless passage are calculated using a boundary layer growth model, based on a 1/7th power law for the boundary layer velocity profile as,

$$C_m = C_{me}(\frac{y}{\delta})^{1/7}, \quad C_u = C_{ue}(\frac{y}{\delta})^{1/7} \tag{3.103}$$

where C_{me} and C_{ue} are the values at the boundary layer edge. Using this assumption, boundary layer area blockage is derived from the integration of mass flux across the passage as,

$$B = \frac{2\delta}{8b} \tag{3.104}$$

Similarly, integrating the angular momentum flux across the passage yields,

$$rC_u = rC_{ue}(1 - \frac{2\delta}{4.5b}) \tag{3.105}$$

Therefore, if the inlet boundary layer thickness, δ_2, is known, rC_{ue} can be computed from inlet rC_u, which is the input coming from impeller analysis. Since the flow domain outside the boundary layer is inviscid, rC_{ue} is conserved ($rC_{ue} =$ constant) until the boundary layer fills the passage, that is $b = 2\delta$. Using this fact, boundary layer thickness at any local position can be computed from the local predicted rC_u. Knowing the boundary layer thickness, blockage, B, at any local position is calculated from Equation 3.104. The limit $2\delta \leq b$ should always be remembered. A simple flat plate boundary layer thickness estimate of the impeller exit is sufficient to start this analysis. It is given by [19],

$$\delta_2 = 5.142\, c_f \frac{L_B}{2}, \quad 2\delta \leq d_H \tag{3.106}$$

where the computation of hydraulic diameter is given in Appendix A. The following empirical equation can also be used instead if a vaneless passage analysis is conducted by itself,

$$\frac{2\delta}{b} = 1 - (\frac{b}{r})_{in}^{0.15} \tag{3.107}$$

The influence of boundary layer thickness, δ, is primarily on the local skin friction coefficient, c_f, along the vaneless passage which is calculated using the pipe friction model described in Appendix A, using 2δ instead of pipe diameter.

Equations through (3.90) to (3.93) are solved by casting them in finite difference form and employing a direct marching technique through the vaneless passage. Vaneless passage is divided into small segments along the meridional direction and each segment is solved by marching through the vaneless space. Exit condition of one segment becomes the inlet condition of the next. Inlet conditions of the first segment are taken from the impeller outlet. The procedure used for vaneless diffuser analysis is given in Figure 3.29. Finite difference form of the equations are [19],

$$2\pi r_{j+1}\rho_{j+1}b_{j+1}C_{m,j+1}(1-B_{j+1}) = \dot{m} \tag{3.108}$$

$$b_j C_{m,j}\frac{\Delta(rC_u)_j}{\Delta m_j} = -r_j C_j C_{u,j} c_{f,j} \tag{3.109}$$

$$\frac{1}{\rho_j}\frac{\Delta p_j}{\Delta m_j} = \frac{C_{u,j}^2 \sin\alpha_{c,j}}{r_j} - C_{m,j}\frac{\Delta C_{m,j}}{\Delta m_j} - \frac{C_j C_{m,j} c_{f,j}}{b_j} - \frac{\Delta I_{D,j}}{\Delta m_j} - I_{C,j} \tag{3.110}$$

where $\Delta()_j = ()_{j+1} - ()_j$ if the forward differencing is used and j indicates the segment number. Segment number (or number of control volumes, nCV) should be increased until the results remain unchanged with its increase, that is, the mesh independency is achieved.

The above analysis can be applied to any vaneless space including vaneless diffuser, vaneless space after vaned diffuser and return bend. Three different vaneless diffuser geometries are used in this thesis as shown in Figure 3.28.

Another important point is that rotating stall can form within the vaneless diffuser if the impeller exit angle falls below a certain angle, especially at low mass flow rates. This stall angle [18] is given by,

$$\alpha_{2,stall} = 3821.5(\frac{b_2}{r_2})^3 - 1559.6(\frac{b_2}{r_2})^2 + 238.24(\frac{b_2}{r_2}) - 0.0733 \tag{3.111}$$

3.3 Vaned Diffuser Performance

Vaned diffuser performance model given by Aungier [13] is similar to that of impeller. Calculations are performed at the inlet, throat and discharge. Since some of the loss coefficients also depend on the discharge conditions, an iterative procedure is again required. This model is validated for conventional airfoil style vaned

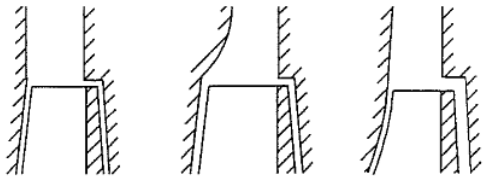

Figure 3.28: Vaneless Diffuser Geometry, from left to right: constant width, constant area, linear shroud

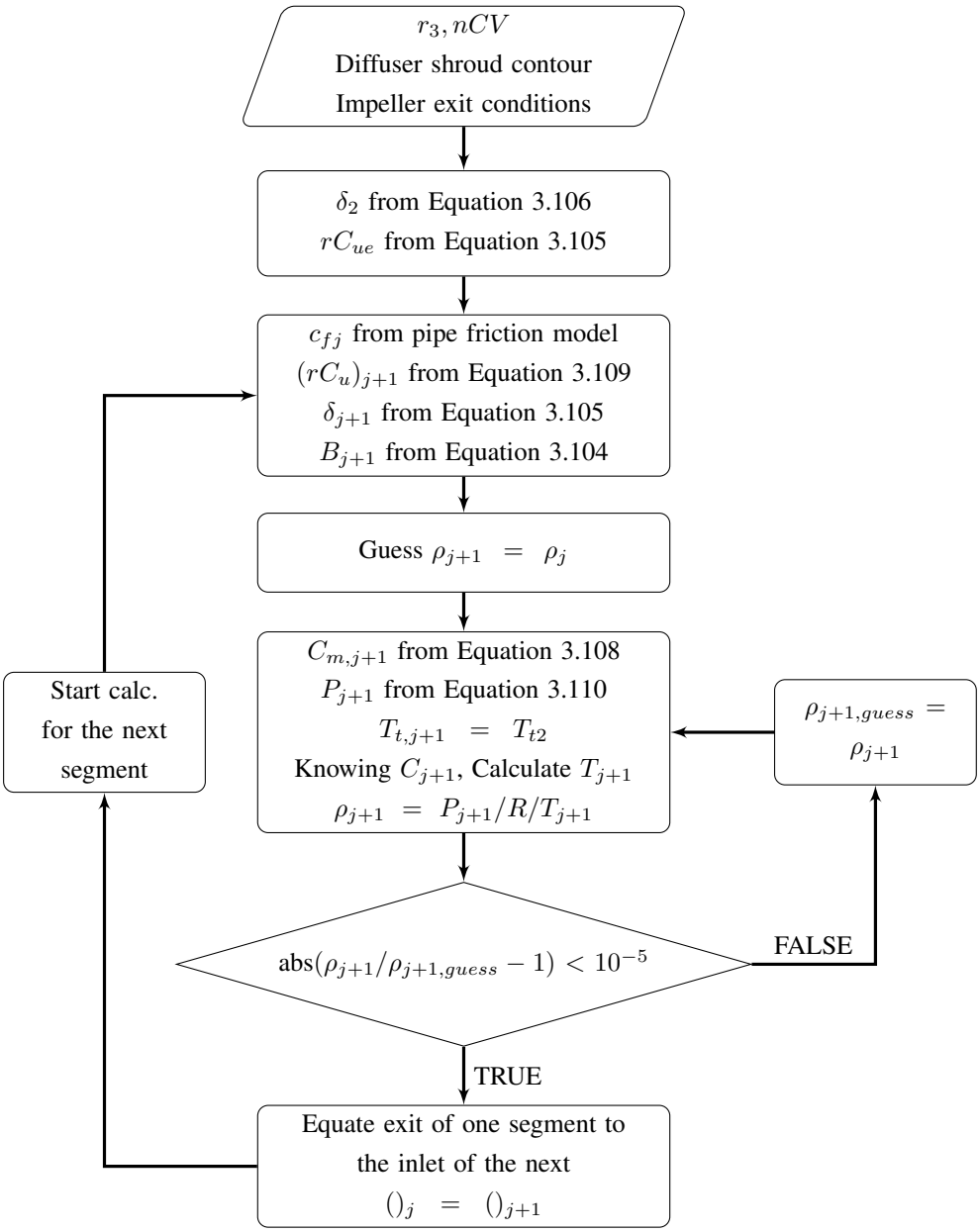

Figure 3.29: Vaneless Passage Analysis Procedure

diffusers; however, it is also generalized to be able to use it for vaned diffusers with nonparallel end walls and thick vanes. Aungier [13] states that this generalization gives reasonable results although it is not validated with high quality test data.

The vaned diffuser geometry used in this thesis is given in Figure 3.30. The inlet and discharge area of the vaned diffuser are given by,

$$A_3 = 2\pi r_3 b_3 - z_{VD} b_3 t_{b3}, \quad A_4 = 2\pi r_4 b_4 - z_{VD} b_4 t_{b4} \tag{3.112}$$

The procedure given in Figure 3.31 is employed for vaned diffuser analysis. The analysis starts with the inputs from the upstream stage component, usually a vaneless diffuser. Then, the choking and stall limits are estimated. Similar to impeller analysis, the blockage at the vane throat is estimated by a throat contraction ratio given by,

$$C_r = \sqrt{\frac{A_3 \sin \beta_3}{A_{th}}} \tag{3.113}$$

Choking will occur if $C_r A_{th} < A^\star_{th}$. Sonic flow area at the throat, $A^\star_{th} = \dot{m}/(\rho^\star C^\star)$, can be calculated using the formulation given by Equations (3.22), (3.23), (3.24) with absolute values instead of relative ones. Vaned diffuser stall estimation is based on the following two parameters supplied by Auniger [13],

$$K = \frac{r_3}{h_{th}} \left(\frac{\cos \alpha_3}{\cos \alpha_{th}} - 1 \right) \tag{3.114}$$

$$K_0 = \frac{M_3^2 \sin^2 \beta_3 \cos \beta_3}{1 - M_3^2 \sin^2 \beta_3} \tag{3.115}$$

After comparing with some experimental stall limits, Auniger [13] came up with the following stall criterion for vaned diffusers,

$$K + K_0 = 0.39 \tag{3.116}$$

which can be solved for $\alpha_{3,stall}$. If the vaned diffuser inlet flow angle, α_3, falls below this value, vaned diffuser stall is expected.

After checking for choking and stall, velocities and thermodynamic properties at the throat can be calculated using a procedure similar to impeller throat calculation procedure given in Section 3.1.5. Again throat and inlet total conditions can be taken equal since they are usually very close.

Vane discharge flow angle, α_4, can be computed using the axial-flow compressor correlations transformed to radial plane. The minimum loss deviation angle of Howell [44] is given by,

$$\delta^\star = \frac{\theta[0.92(a/c)^2 + 0.02(90 - \beta_4)]}{\sqrt{\sigma} - 0.02\theta} \tag{3.117}$$

where the location of point of maximum camber, a/c, solidity, σ, and camber angle, θ, are given by,

$$\frac{a}{c} = \frac{1}{3}(2 - \frac{\bar{\beta} - \beta_3}{\beta_4 - \beta_3}) \tag{3.118}$$

$$\sigma = \frac{z(r4 - r3)}{2\pi r_3 \sin\bar{\beta}} \tag{3.119}$$

$$\theta = \beta_4 - \beta_3 \tag{3.120}$$

where the vane angle at the midchord can be estimated as $\bar{\beta} = (\beta_3 + \beta_4)/2$. Aungier [13] models the variation of the deviation angle with incidence using the graphical data presented by Johnsen and Bullock [45] as,

$$\frac{\partial\delta}{\partial i} = \exp[((1.5 - \frac{\beta_3}{60})^2 - 3.3)\sigma] \tag{3.121}$$

Finally, the vaned diffuser discharge flow angle is calculated as,

$$\alpha_4 = \beta_4 - \delta^\star - \frac{\partial\delta}{\partial i}(\beta_3 - \alpha_3) \tag{3.122}$$

Next, the choking and incidence loss coefficients, which are the loss coefficients which do not depend on the discharge conditions, are calculated. They are the choking loss coefficient, ω_{CH}, and the incidence loss coefficient, ω_{INC}. The choking loss calculation is identical to that of impeller. The minimum-loss incidence angle is defined as,

$$\sin\alpha_3^\star = \sqrt{\sin\beta_3 \sin\alpha_{th}} = \frac{C_{m3}}{C_3^\star} \tag{3.123}$$

The minimum incidence loss for this minimum-loss incidence is given by,

$$\bar{\omega}_{INC0} = 0.8(\frac{C_3^\star - C_{th}}{C_3})^2 + \frac{zt_{b3}}{2\pi r_3} \tag{3.124}$$

The off-design incidence for incidence angles other than minimum-loss incidence is given by,

$$\bar{\omega}_{INC} = 0.8(\frac{C_3 - C_3^\star}{C_3})^2 \tag{3.125}$$

for $C_3 < C_{3,stall}$, where $C_{3,stall} = C_{m3}/\sin\alpha_{3,stall}$. If $C_3 > C_{3,stall}$,

$$\bar{\omega}_{INC} = 0.8[((\frac{C_3}{C_{3,stall}})^2 - 1)\frac{C_{th}^2}{C_3^2} + \frac{(C_{3,stall} - C_3^\star)^2}{C_{3,stall}^2}] \tag{3.126}$$

Similar to the impeller analysis, discharge conditions should be estimated to start the iterations. This estimation can be performed assuming that there is no total pressure loss within the vaned diffuser, that is, $p_{t4} = p_{t3}$.

After an initial estimation is done, the iterations are done for the discharge conditions. During this iterations, the loss coefficients which depend on the discharge conditions are calculated and updated with each iteration. They include the skin friction loss, $\bar{\omega}_{SF}$, abrupt expansion loss, $\bar{\omega}_\lambda$, and the wake mixing loss, $\bar{\omega}_{MIX}$. Aungier [13] supplies the skin friction loss as,

$$\bar{\omega}_{SF} = \frac{4c_f L_B}{d_H(2\delta/d_H)^{0.25}}(\frac{\bar{C}}{C_3})^2 \tag{3.127}$$

where the hydraulic diameter, d_H, and skin friction coefficient, c_f, are calculated using the average of throat and discharge values as in the case of impeller. Calculation of them are given in Appendix A. Similar to the vaneless diffuser analysis, the boundary layer thickness at midpassage is estimated using a simple flat-plate boundary layer approximation as,

$$\delta = 5.142c_f\frac{L_B}{2}, \quad \delta \leq \frac{d_H}{2} \tag{3.128}$$

The mean velocity, $\bar{C}$, within the vaned diffuser is calculated by,

$$\bar{C}^2 = \max[0.5(C_3^2 + C_4^2), 0.5(C_{th}^2 + C_4^2)] \tag{3.129}$$

For the remaining loss coefficients, the discharge area blockage, B_4, is needed and the correlation provided by Aungier [13] employs the following two basic design parameters,

$$2\theta_C = \tan^{-1}[((w_4 - t_{b4})\frac{b_4}{b_3} - w_3 + t_{b3})\frac{1}{2L_B}] \tag{3.130}$$

$$L = \frac{\Delta C}{C_3 - C_4} \tag{3.131}$$

where the average blade-to-blade velocity difference is given as,

$$\Delta C = \frac{2\pi}{zL_B}(r_3C_{u3} - r_4C_{u4}) \tag{3.132}$$

from simple potential flow and $w = 2\pi r \sin\beta/z$. It is observed that when $L > 1/3$ or $2\theta_C > 11°$, a sudden drop in vaned diffuser performance occurs. Based on this observation, the following correction coefficients are defined,

$$K_1 = 0.2(1 - \frac{1}{C_L C_\theta}) \tag{3.133}$$

$$K_2 = \frac{2\theta_C}{125 C_\theta}(1 - \frac{2\theta_C}{22 C_\theta}) \tag{3.134}$$

where $C_\theta = \max(2\theta_C/11, 1)$ and $C_L = \max(3L, 1)$. The discharge area blockage is defined as,

$$B_4 = [K_1 + K_2(\bar{C}_R^2 - 1)]\frac{L_B}{w_4} \tag{3.135}$$

where $\bar{C}_R = 0.5[C_{m3}\sin\beta_4/(C_{m4}\sin\beta_3) + 1]$. Similar to the impeller analysis, an abrupt expansion loss can be defined as,

$$\bar{\omega}_\lambda = [(\lambda_4 - 1)\frac{C_{m4}}{C_3}]^2 \tag{3.136}$$

where $\lambda_4 = 1/(1 - B_4)$. Finally, a wake mixing loss is included to account for excessive streamwise diffusion and vane discharge blade thickness. It is assumed that the flow separates at a velocity given by,

$$C_{SEP} = \frac{C_3}{1 + 2C_\theta}, \quad C_{SEP} \geq C_4 \tag{3.137}$$

The meridional velocities before and after the mixing are calculated from the conservation of mass as,

$$C_{m,wake} = \sqrt{C_{SEP}^2 - C_{u4}^2} \tag{3.138}$$

$$C_{m,mix} = \frac{A_4 C_{m4}}{2\pi r_4 b_4} \tag{3.139}$$

Employing these velocities, wake mixing loss is defined by,

$$\bar{\omega}_{MIX} = (\frac{C_{m,wake} - C_{m,mix}}{C_3})^2 \tag{3.140}$$

After calculating all of the loss coefficients, the discharge total pressure can be calculated from,

$$p_{t4} = p_{t3} - (p_{t3} - p_3)\bar{\omega}_{tot} \tag{3.141}$$

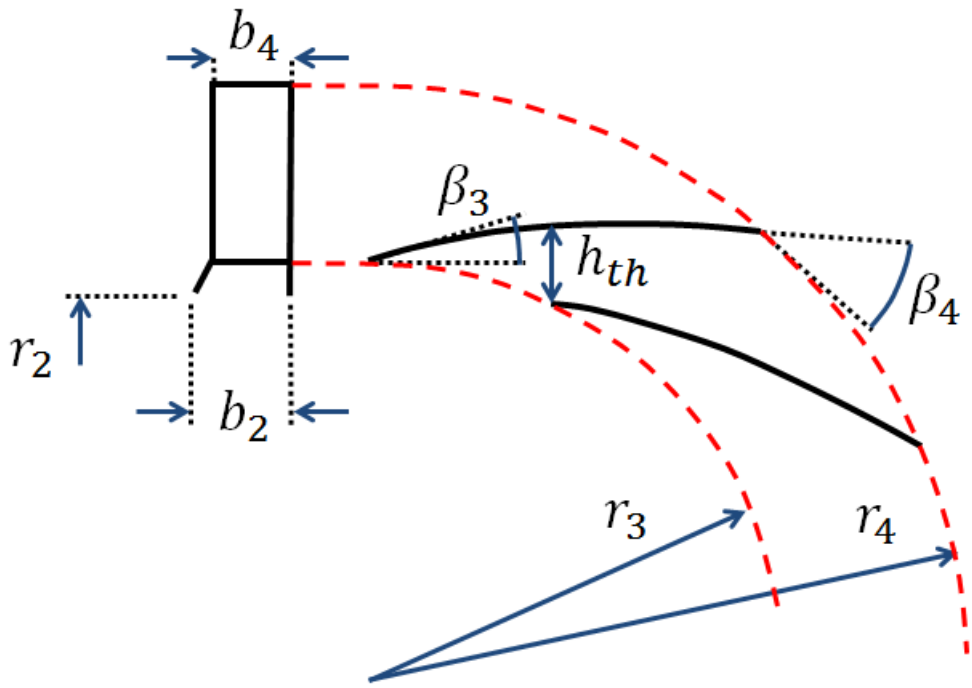

Figure 3.30: Vaned diffuser geometry [13]

where $\bar{\omega}_{tot} = \bar{\omega}_{INC} + \bar{\omega}_{CH} + \bar{\omega}_{SF} + \bar{\omega}_{\lambda} + \bar{\omega}_{MIX}$. Knowing α_4 and using conservation of mass to calculate C_{m4}, all of the velocity components at the discharge can be calculated. Since p_{t4} and $T_{t4} = T_{t3}$ are also known, static properties can be calculated using the definition of total temperature and isentropic relation. This process continues until the convergence on discharge density, ρ_4, is achieved.

3.4 Preliminary Diffuser Sizing

Correlations and design limits given by Aungier [13] is used for preliminary sizing of the vaneless and vaned diffuser. The vaned diffuser leading edge radius is estimated by,

$$\frac{r_3}{r_2} = 1 + \frac{\alpha_3}{360} + \frac{M_2^2}{15} \tag{3.142}$$

A simplified form of the angular momentum equation including wall friction effects through the vaneless space is used to calculate C_{u3} as,

$$\ln\left(\frac{r_3 C_{u3}}{r_2 C_{u2}}\right) = \frac{-c_f (r_3 - r_2)}{\bar{b} \sin \bar{\alpha}} \tag{3.143}$$

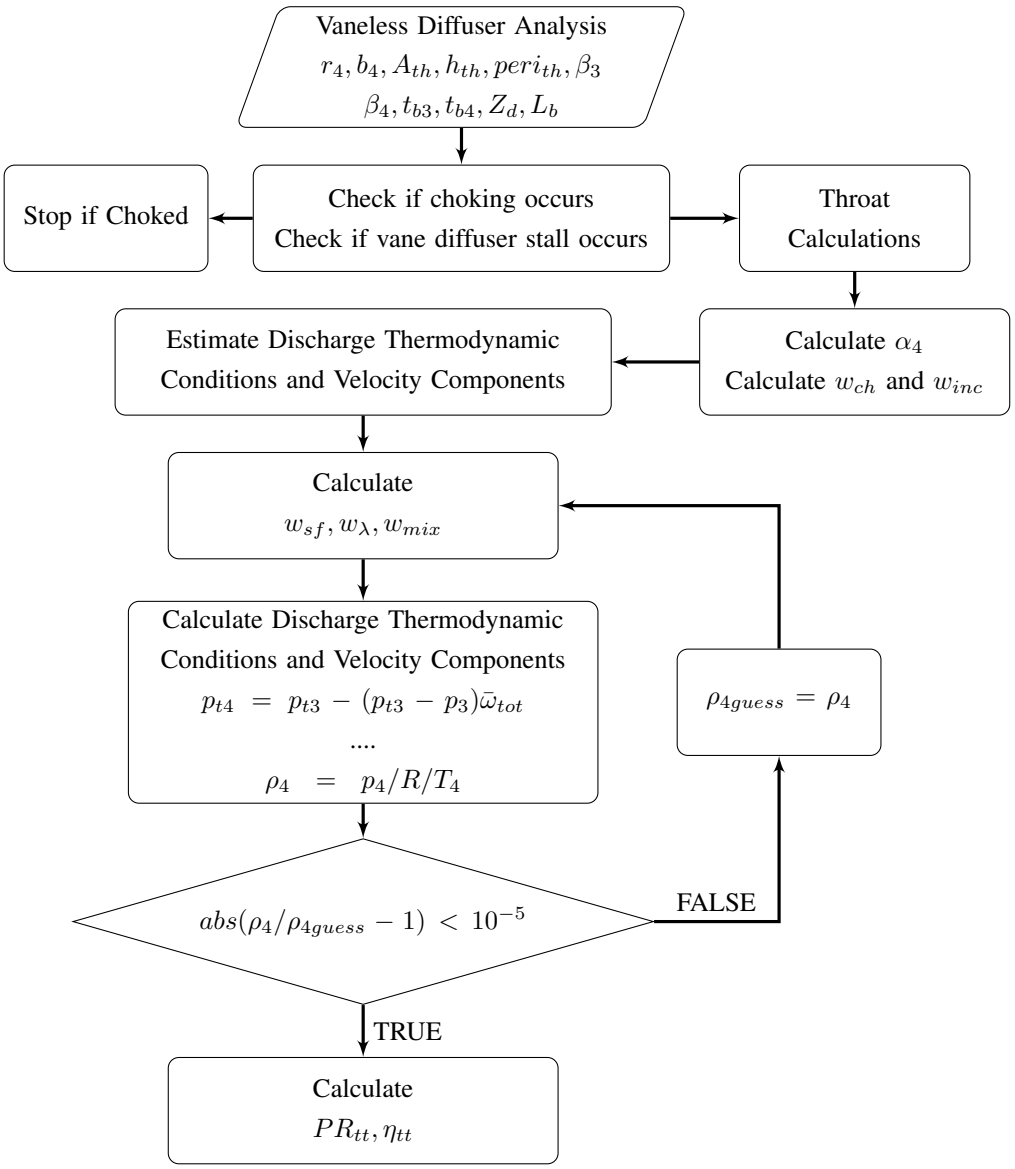

Figure 3.31: Vaned diffuser analysis procedure

where $\bar{b} = (b_2 + b_3)/2$ and $\bar{\alpha} = (\alpha_2 + \alpha_3)/2$. Another constraint on passage width comes from conservation of mass as,

$$r_2 b_2 C_{m2} = r_3 b_3 C_{m3} \tag{3.144}$$

taking density as constant.

Sizing of the vaneless diffuser starts with the specification of α_3. Equation 3.142 is employed to calculate r_3. Next, Equations (3.143) and (3.144) are used to calculate b_3. However, these equations also contain b_3 itself. Therefore, an iterative procedure is required, for which b_3 is guessed and updated until convergence. Another constraint on b_3 is that is should be less than b_2, that is, $b_3 \leq b_2$.

For the sizing of vaned diffuser, incidence angle, i_3, should specified so that $\beta_3 = \alpha_3 + i_3$ is known. Selection of the vane number is based on both aerodynamic and resonance considerations. It is preferred that $z_{VD} = z_{imp} \pm 1$. It is also preferred that $10 \leq z_{VD} \leq 20$ due to improved stall incidence range. If $z_{VD} = z_{imp} \pm 1$ do not fall within this range, $|z_{VD} - z_{imp}| \leq 8$ is required. Sizing of the discharge based on the following three design parameters; divergence angle, $2\theta_C$, blade loading parameter, L, and area ratio, A_R. They are given as,

$$\tan\theta_C = \frac{\pi(r_4 \sin\beta_4 - r_3 \sin\beta_3)}{z_{VD} L_B} \tag{3.145}$$

$$L = \frac{2\pi(r_3 C_{u3} - r_4 C_{u4})}{z_{VD} L_B (C_3 - C_4)} \tag{3.146}$$

$$A_R = \frac{r_4 \sin\beta_4}{r_3 \sin\beta_3} \tag{3.147}$$

The preferred ranges for these parameters given by Aungier [13] are $7^\circ < 2\theta_C < 10.5^\circ$, $L \leq 1/3$, and $1.4 < A_R < 2.4$. Besides these limits, it is also required to keep the r_4 below the values estimated by,

$$r_4 = (1.55 + \phi) r_2 \tag{3.148}$$

Discharge width, b_4 can be taken equal to the inlet width, that is, $b_4 = b_3$. Since no detailed shape of the vaned diffuser is available at the preliminary design phase, the following relation is used to estimate vane length,

$$L_B \approx \frac{2(r_4 - r_3)}{\sin\beta_3 + \sin\beta_4} \tag{3.149}$$

Specifying r_4 and θ_C, keeping the restrictions given above in mind, Equation (3.145) can be used to calculate β_4. Next, A_R and L are calculated and checked if they lie within the specified ranges given above. If they don't, specification of r_4 and θ_C should be revisited. The exit flow angle, α_4, can be computed using the minimum loss deviation angle of Howell [44] described in Section 3.3.

Throat parameters of the vaned diffuser can be calculated by estimating the throat width, h_{th}. Using the estimated throat width, throat area and throat periphery can be calculated as,

$$A_{th} = h_{th} b_{th} z_{VD} \tag{3.150}$$

$$peri_{th} = 2(h_{th} + b_{th}) z_{VD} \tag{3.151}$$

where it is usually assumed that $b_{th} = b_3$.

Throat width of a wedge type diffuser can be calculated using the sizing procedure given by Johannes [17]. He calculates the angles shown in Figure 3.32 as,

$$\gamma = \frac{2\pi}{z_{VD}} \tag{3.152}$$

$$\phi = \frac{\gamma}{2} - \theta_C \tag{3.153}$$

where θ_C is the channel divergence angle, ϕ is the wedge divergence angle and γ is the angle between two adjacent wedges. The channel divergence angle is calculated using Equation (3.130) and wedge divergence angle is calculated using Equation (3.153).

After calculating these angles, he gives letters to the important points on the wedge diffuser and employs a coordinate rotation of $\phi_{coord} = -(\beta_3 + \phi)$ as shown in Figure 3.32. The new axes are shown with χ and η. Coordinate of each letter on this coordinate system is calculated using basic geometrical relations. Finally, the throat width is calculated as,

$$h_{th} = \overline{bf_\chi} \tag{3.154}$$

3.5 Return System Performance

The return system geometry relevant to this thesis is given in Figure 3.33. As it can be seen from this figure, it consists of a return bend, a return channel and an exit duct.

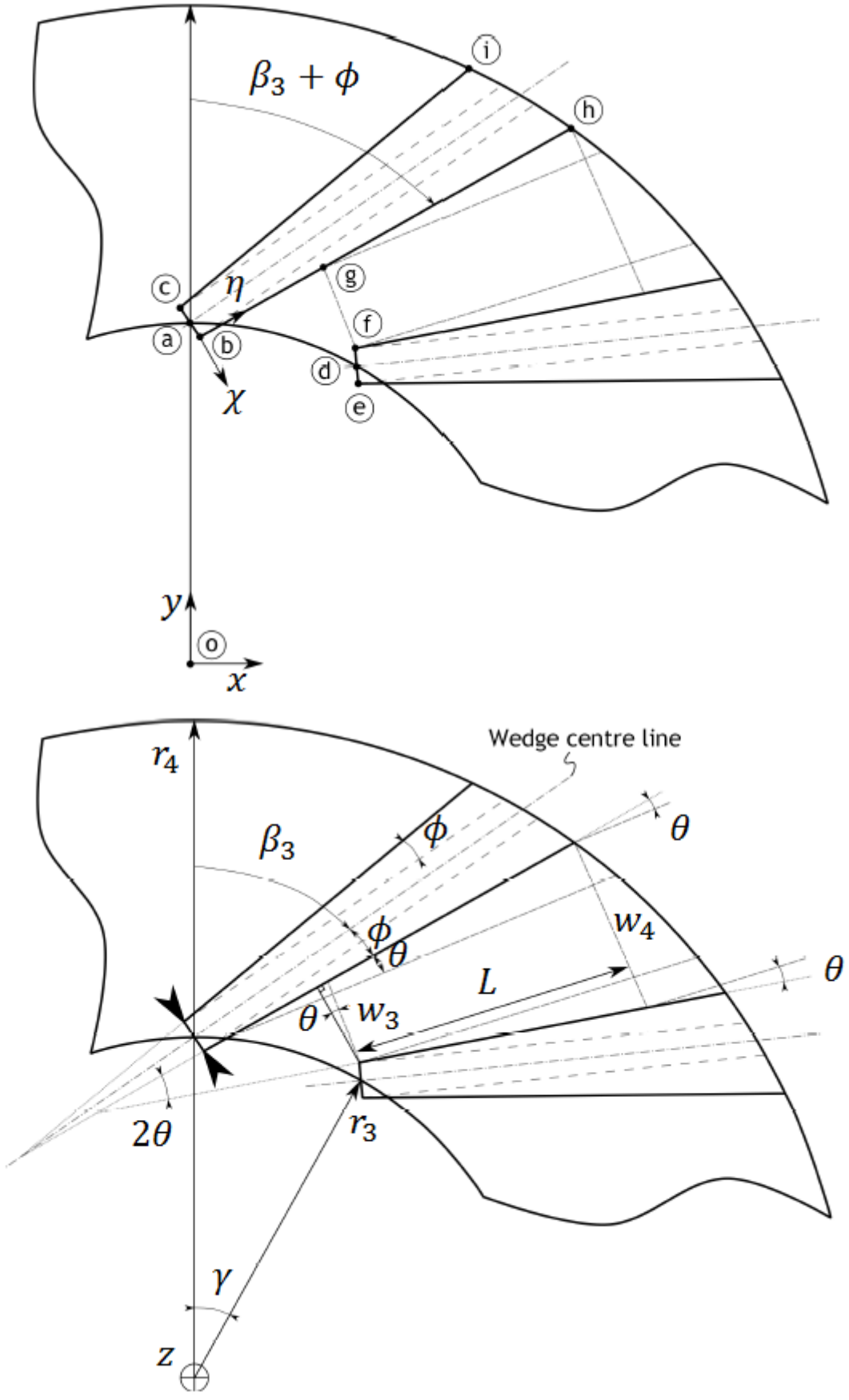

Figure 3.32: Wedge Diffuser Geometry [17]

Analysis of the return bend can be performed using the procedure explained in Section 3.2. However, since the return bend geometry is more complicated than a vaneless diffuser geometry, it can be difficult to supply the geometrical information needed by this procedure for a return bend. If this is the case and the designer can assume a loss coefficient, LC, and a swirl coefficient, $SC = C_{u6}/C_{u5}$, from his previous experience, the alternative approach given by Figure 3.34 can be employed. In this procedure, a diffusion factor, DF, guess is made and iterated until convergence using the given LC and SC along with conservation of mass.

Return channel analysis of Auniger [13] is similar to the analysis of vaned diffuser mentioned in Section 3.3. Some differences occur due to distorted flow coming from return bend and curvature of the return channel. Two estimates of the aerodynamic blockage are made for the aerodynamic blockage at the vane entrance as,

$$B_6 = 1 - \frac{(rb)_m}{r_6 b_6}, \quad B_6 = \frac{(\kappa_m b_6)^2}{12 + (\kappa_m b_6)^2} \tag{3.155}$$

and the larger value of these two estimates is used in the analysis. The minimum loss incidence angle is adjusted to account for this entrance blockage as,

$$\tan \alpha^\star = (1 - B_6) \tan[\sin^{-1}(\frac{A_{th}}{A_6})] \tag{3.156}$$

The incidence loss coefficient is given by,

$$\bar{\omega}_{INC} = 0.8(1 - \frac{C_{m6}}{C_6 \sin \alpha^\star})^2 \tag{3.157}$$

Skin friction loss coefficient is also modified to account for the loss associated with the channel curvature as,

$$\bar{\omega}_{SF} = 4c_f(\frac{\bar{C}}{C_6})^2 \frac{L_B}{d_H} + C_{m6}C_{m7}\frac{|\alpha_{c6} - \alpha_{c7}|}{13C_6^2} \tag{3.158}$$

where $\bar{C} = \max((C_6+C_7)/2, (C_{th}+C_7)/2)$, d_H is the average of throat and discharge hyraulic diameters and c_f is calculated from pipe friction model given in Appendix A using the average values of throat and discharge. Blade loading loss coefficient is given by,

$$\bar{\omega}_{BL} = \frac{1}{6}(\frac{\Delta C}{C_6})^2 \tag{3.159}$$

where the average blade-to-blade velocity difference is computed from

$$\Delta C = \frac{2\pi}{zL_B}(r_6 C_{u6} - r_7 C_{u7}) \tag{3.160}$$

Maximum velocity at the vane surface is estimated by,

$$C_{max} = 0.5(C_6 + C_7) + \Delta C \tag{3.161}$$

assuming it occurs at the midpassage. $C_{max} > C_6$ is also required. From this velocity, separation velocity is calculated as,

$$C_{SEP} = 0.5 C_{max} \text{ if } C_{max} > 2C_7 \tag{3.162}$$

$$C_{SEP} = C_7 \text{ otherwise} \tag{3.163}$$

Therefore the meridional velocities before and after the wake mixing are,

$$C_{m,wake} = \sqrt{C_{SEP}^2 - C_{u7}^2}, \;\; C_{m,mix} = \frac{C_{m7} A_7}{\pi(r_{7s} + r_{7h}) b_7} \tag{3.164}$$

Finally, the wake mixing loss is calculated as,

$$\bar{\omega}_{MIX} = (\frac{C_{m,wake} - C_{m,mix}}{C_6})^2 \tag{3.165}$$

The flow discharge angle is calculated from the minimum loss deviation angle of Howell [44] and off-design incidence effect on flow deviation angle model of Johnsen and Bullock [45] as explained in Section 3.3.

The losses due to the exit duct is given by,

$$\bar{\omega}_o = (4c_f + \frac{1}{13})|\alpha_{c7} - \alpha_{c8}|(\frac{C_{m7}}{C_6})^2 \tag{3.166}$$

which accounts for the friction and curvature losses. After calculating all loss components, the total pressure at the discharge can be calculated from,

$$p_{t8} = p_{t6} - (p_{t6} - p_6)\bar{\omega}_{tot} \tag{3.167}$$

where $\bar{\omega}_{tot} = \bar{\omega}_{INC} + \bar{\omega}_{SF} + \bar{\omega}_{BL} + \bar{\omega}_{MIX} + \bar{\omega}_o$.

The analysis procedure is the same as the vaned diffuser analysis procedure given in Section 3.3.

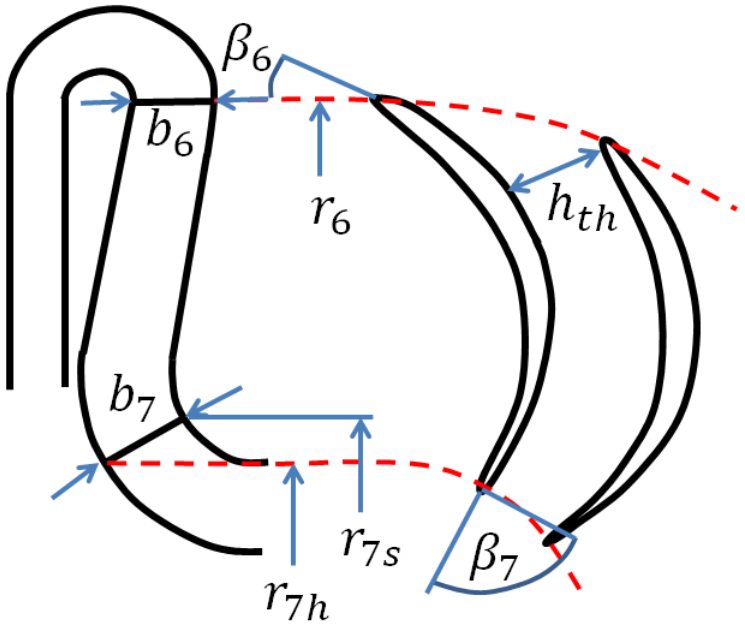

Figure 3.33: Return Channel Geometry [13]

3.6 Inlet Guide Vane (IGV) Performance

Procedure given by Herbert [12] is used for IGV performance analysis. He employs the profile loss coefficient of Ainley and Mathieson [46] and secondary loss coefficient of Dunham [47]. They are given by,

$$\bar{\omega}_p = 0.016 + 0.09(1 - \frac{s_{mean}}{c_{IGV}})^{2.64} \tag{3.168}$$

$$\bar{\omega}_s = 0.022\frac{c_{IGV}}{h_{mean}}\sin^2\alpha_0\cos\alpha_0(1+\frac{1}{4}\tan^2\alpha_0)^{0.5}[1+10(\frac{(1-B_{-1})h_{mean}}{c_{IGV}})^{0.5}] \tag{3.169}$$

where the second term of equation 3.168 drops for $s_{mean}/c_{IGV} > 1$. Total pressure loss is calculated using these loss coefficients as [12],

$$\frac{p_{t-1} - p_{t0}}{p_{t0} - p_0} = (\bar{\omega}_p + \bar{\omega}_s)(\frac{Re_0}{2 * 10^5})^{-0.2} \tag{3.170}$$

where $Re_0 = \rho_0 C_0 c_{IGV}/\mu_0$.

The procedure given in Figure 3.36 can be followed to calculate the conditions after the IGV. First some geometrical parameters are calculated which will be required by the foregoing analysis. Second, profile and secondary loss calculations are carried out using the calculated geometrical parameters. Next, the inlet is analyzed using a

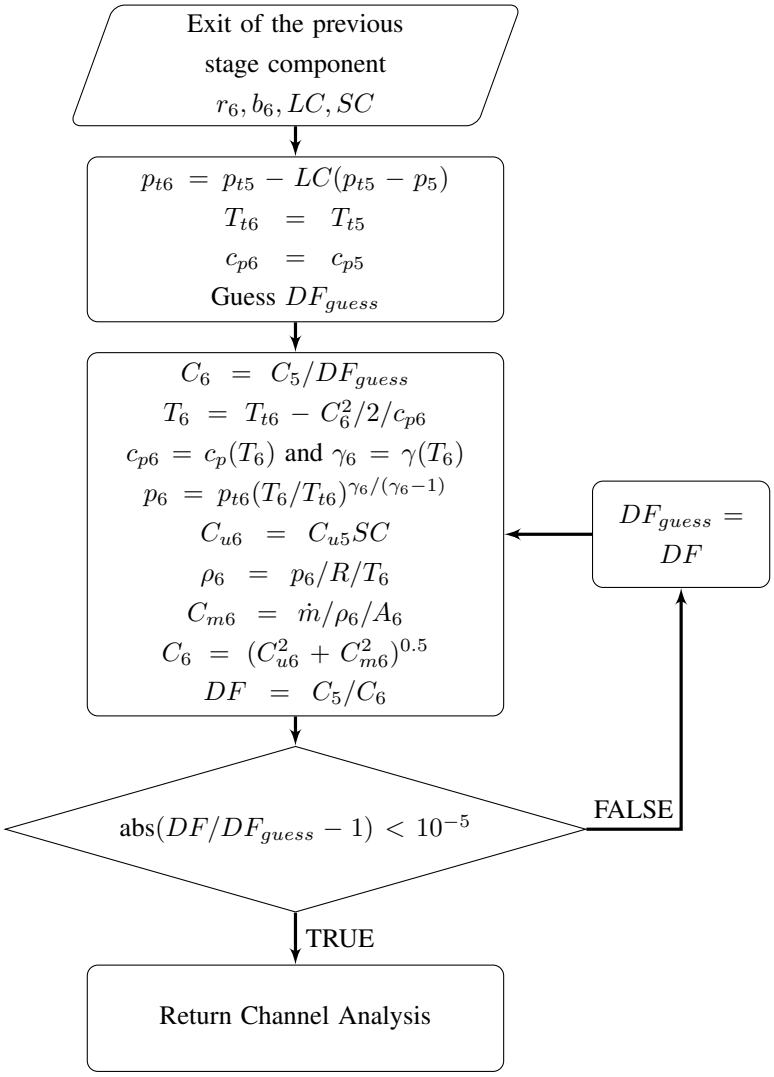

Figure 3.34: Alternative Return Bend Analysis Procedure

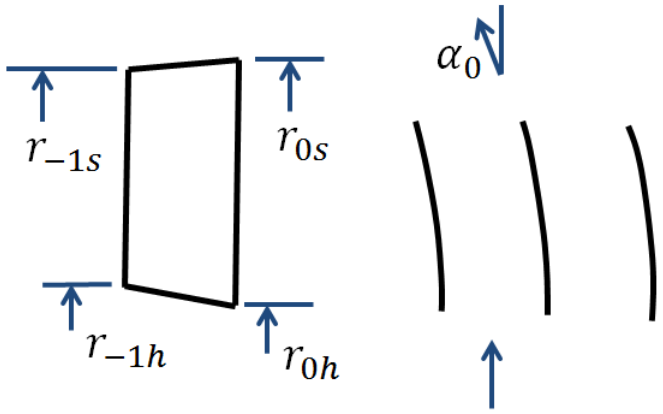

Figure 3.35: IGV Geometry [12]

procedure similar to Section 3.1.4. Finally, a guess of outlet total pressure is done as,

$$p_{t0guess} = p_{t-1} - 0.5(\bar{\omega}_p + \bar{\omega}_s)\rho_{-1}C_{-1}^2 \tag{3.171}$$

and iterated with Equation (3.170) to converge to a final p_{t0}.

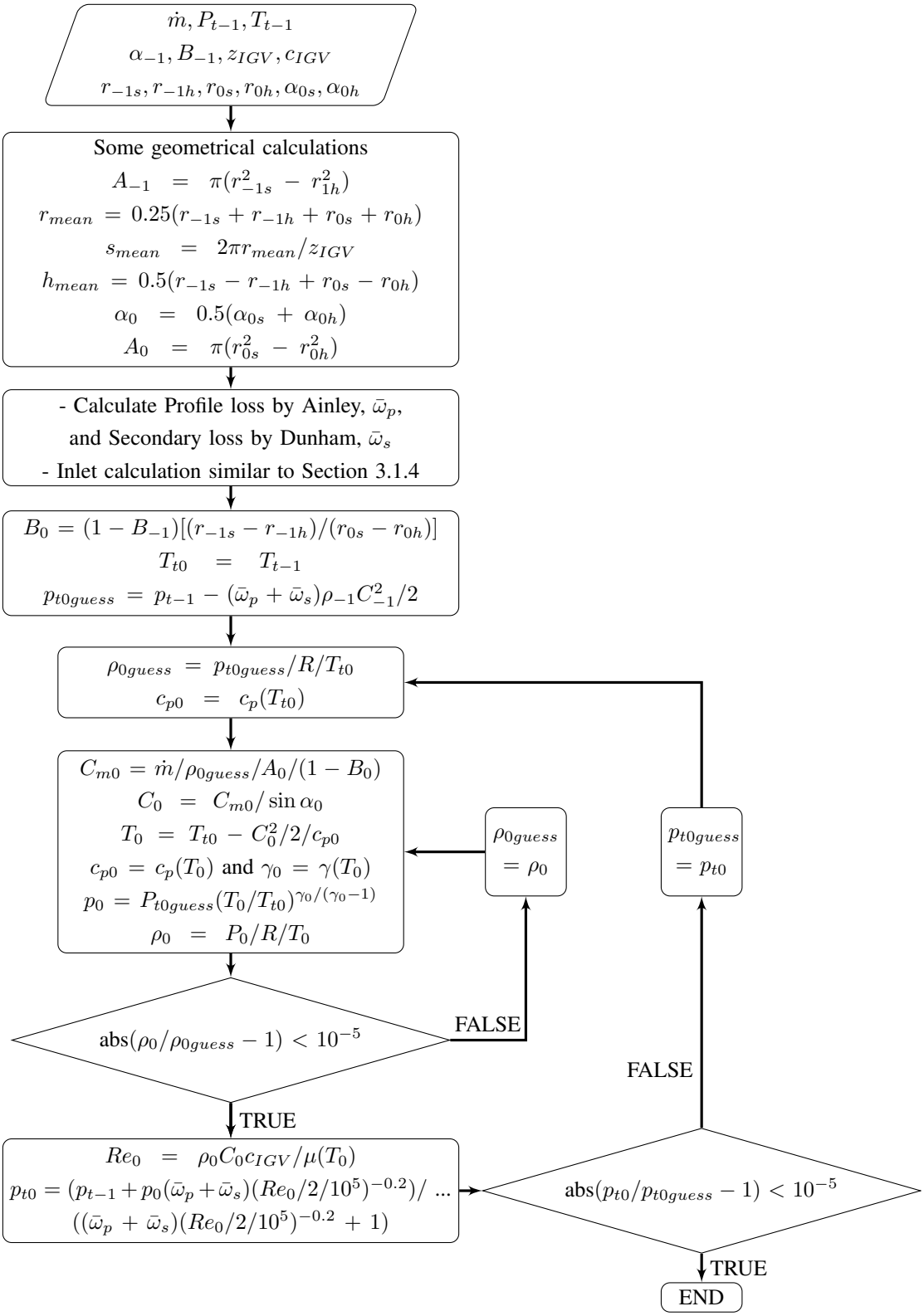

Figure 3.36: IGV Analysis Procedure

CHAPTER 4

VALIDATION CASES

4.1 Eckardt O-rotor Stage

The Eckardt O-rotor stage consists of a rotor with 20 radial blades with no backsweep and a long vaneless diffuser with hyperbolic shroud. The detailed geometry of the stage can be found in references [18], [19] and Table 4.1.

As it can be seen from Figure 4.1, slope of the performance curves over the stall region is estimated poorly. Klausner and Gampe [18] explains this behavior as follows. Since the impeller blades have no backsweep, Equation (3.11) reduces to $I_B = \sigma$ for the no inlet swirl case. Therefore, the dependency of blade work input on mass flow rate is removed for this case, which leads to an overestimation of blade work input at high mass flow rates, causing early impeller stall. This overestimation of blade work input also produces high C_{u2} velocities and low α_2 angles, which contributes to the diffusion losses at the vaneless diffuser. It can also seen from Table 4.2 that the prediction of C_{u2} is poor, especially at high mass flow rates. However, results are consistent with a reference solution which also uses a one zone model. Figure 4.3 shows the contributions from different loss components. As it can be seen from this figure, the incorrect gradient is caused by the parasitic losses and vaneless diffuser losses. Despite this poor behavior, the error on pressure characteristics reaches approximately 4% and the error on efficiency characteristics reaches 12% at high speeds.

Variation of total pressure, static pressure and flow angle along the vaneless diffuser is plotted in Figure 4.2 to assess the performance of vaneless diffuser analysis. Trends

Table 4.1: O-rotor Stage Geometry [18]

Impeller							
Inlet		Throat		Tip		Overall	
r_{1h}[mm]	45	A_{th}[mm^2]	32080.1	r_2[mm]	200	z_{FB}	20
r_{1s}[mm]	140	β_{th}[°]	39.76	b_2[mm]	26	z_{SB}	0
β_{1h}[°]	57.12	$peri_{th}$[m]	4.422	β_2[°]	90	L_b[mm]	202.26
β_1[°]	33.83			α_{c2}[°]	86.15	L_{fb}[mm]	171.26
β_{1s}[°]	26.75			t_{b2}[mm]	1.08	L_{sb}[mm]	0
α_{c1}[°]	1.68					s_{cl}[mm]	0.372
κ_{m1}[rad/m]	-2.49					s_d[mm]	0.372
t_{b1}[mm]	2.11						
Vaneless diffuser							
r_3[mm]	340						
Type	Hyperbolic shroud						

are captured quite well although there is a slight shift due to the incorrect initial condition given by the impeller exit.

4.2 Radiver Stage

The Radiver Stage consists of an impeller with 15 backswept blades and a diffuser of different configurations. The detailed geometry can be found in references [18, 20, 21] and Table 4.3.

For one configuration, it has a short vaneless passage followed by a wedge type vaned diffuser. Figure 4.4 gives the pressure ratio map for this configuration. Unfortunately, no complete efficiency map is available in the literature. The pressure ratio characteristics is estimated well except the choking regions at low speeds. A much more abrupt choking than the real case is obtained. The error of the choke estimation reaches 8% at low speeds. The reason for this behavior is probably due to the incorrect estimation of blockage at the vaned diffuser throat. In fact, removing this blockage and resolving the stage, Figure 4.5 is obtained. As it can be seen from

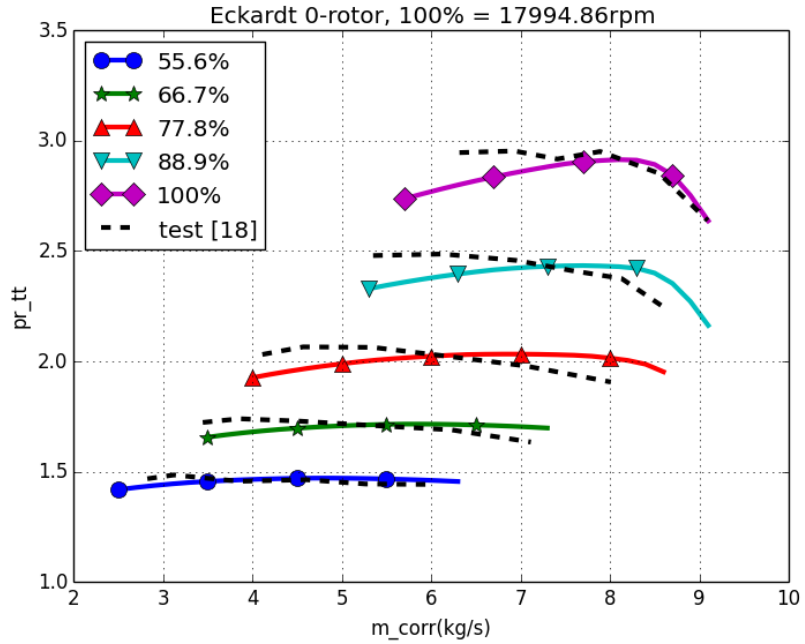

(a) PR_{tt} *vs.* $\dot{m}_{corr}$

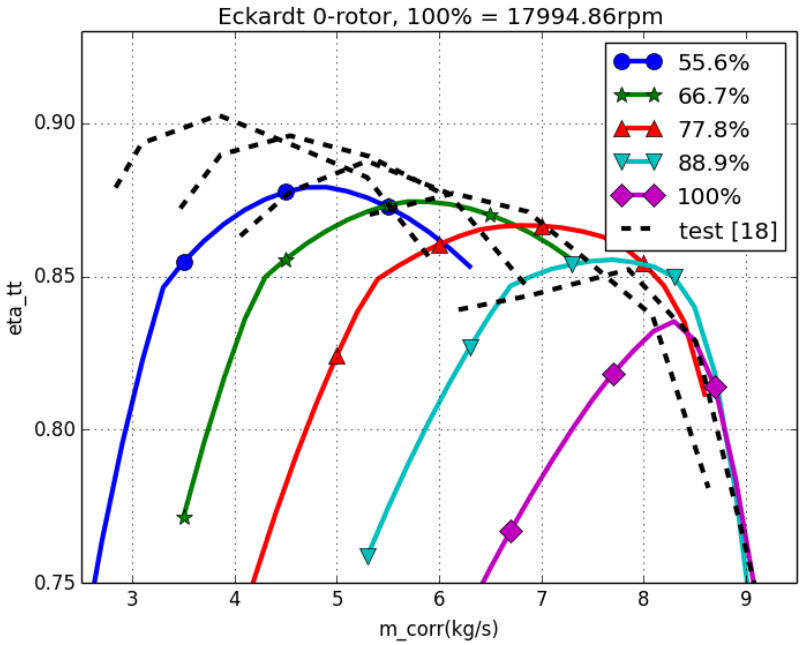

(b) η_{tt} *vs.* $\dot{m}_{corr}$

Figure 4.1: O-rotor Performance Map

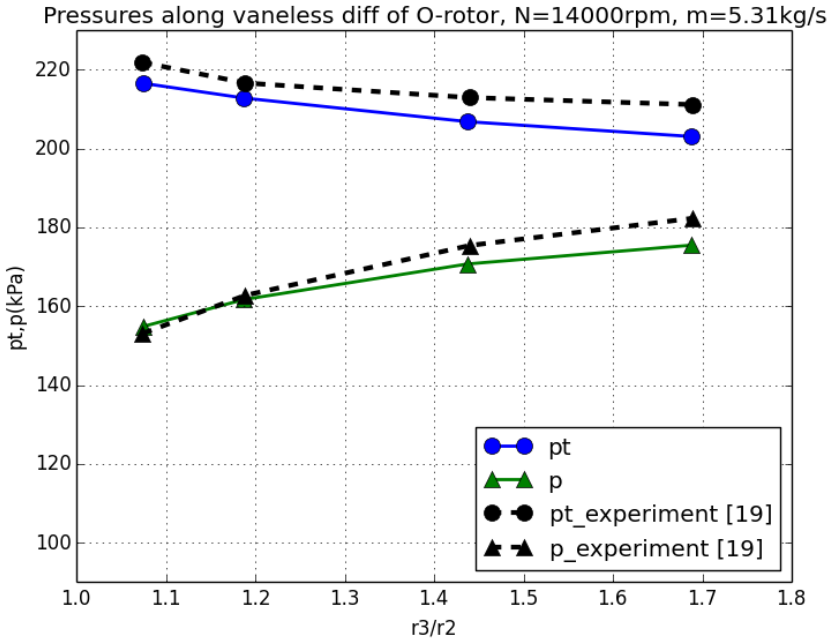

(a) Total and Static Pressure

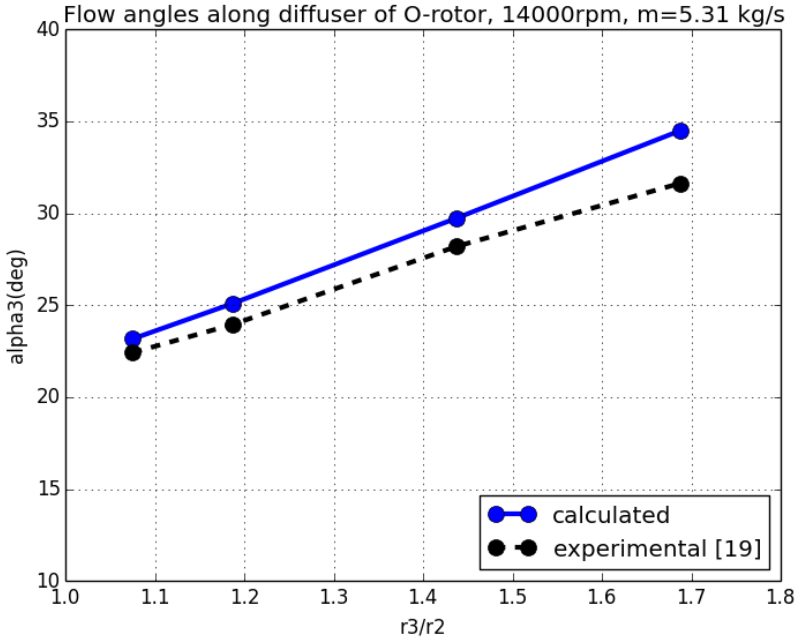

(b) Flow angle

Figure 4.2: O-rotor, Distributions along Vaneless Diffuser

Table 4.2: O-rotor Impeller Exit Comparison

	Experiment [18]		Reference Solution [18]		Developed Code		Error (%) by reference [18]		Error (%) by Developed Code	
$\dot{m}$ [kg/s]	6.07	5.32	6.07	5.32	6.07	5.32	6.07	5.32	6.07	5.32
T_{t2} [K]	364	363.5	363.3	363.3	362.6	362.7	0.192	0.06	0.38	0.23
$\eta_{s,imp}$	0.959	0.951	0.961	0.962	0.95	0.948	0.2	1.16	0.94	0.315
C_2/U_2	0.97	0.981	0.967	0.945	0.967	0.945	0.3	3.7	0.3	3.7
C_{u2}/U_2	0.819	0.899	0.877	0.877	0.876	0.876	7.08	2.45	6.96	2.55
W_2/U_2	0.502	0.407	0.424	0.371	0.43	0.376	15.5	8.85	14.3	7.62
α_2 [°]	29.8	23.7	24.83	21.78	25.13	22.08	16.7	8.1	15.67	6.84

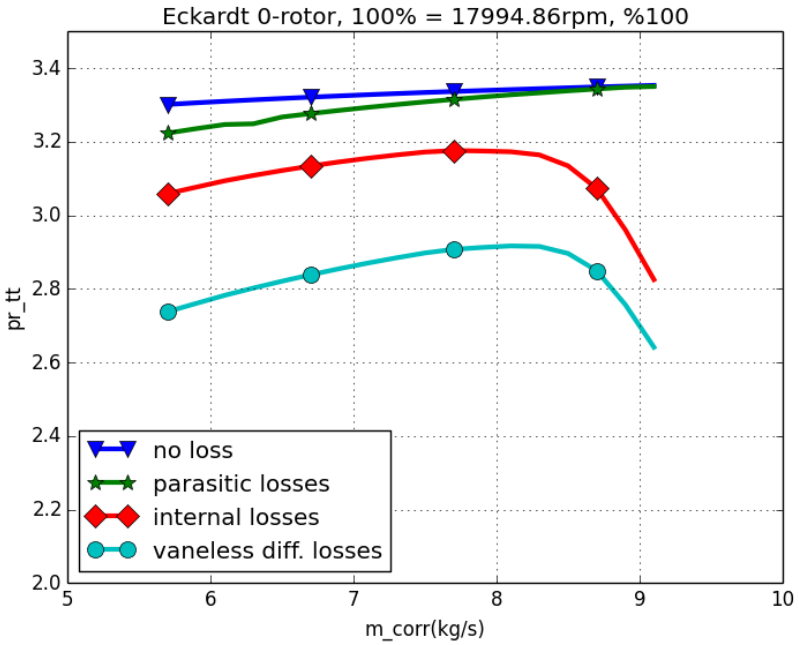

Figure 4.3: Loss Contributions

Table 4.3: Radiver Stage Geometry [18]

Impeller							
Inlet		Throat		Tip		Overall	
r_{1h}[mm]	30	A_{th}[mm^2]	8668.28	r_2[mm]	135	z_{FB}	15
r_{1s}[mm]	72.9	β_{th}[°]	40.72	b_2[mm]	11.1	z_{SB}	0
β_{1h}[°]	66.596	$peri_{th}$[m]	1.701	β_2[°]	52.36	L_b[mm]	139.19
β_1[°]	43.881			α_{c2}[°]	88.28	L_{fb}[mm]	122.77
β_{1s}[°]	33.435			t_{b2}[mm]	1.68	L_{sb}[mm]	0
α_{c1}[°]	7					s_{cl}[mm]	0.585
κ_{m1}[rad/m]	-5.22					s_d[mm]	0.585
t_{b1}[mm]	0.92						
Vaneless diffuser							
r_3[mm]	139 (345 for the vaneless configuration)						
Type	Constant width						
Vaned diffuser							
Inlet		Throat		Tip		Overall	
β_3[°]	19.97	A_{th}[mm^2]	3919	r_4[mm]	277.62	Z_d	23
t_{b3}[mm]	0.45	h_{th}[mm]	17.25	b_4[mm]	11.1	L_b[mm]	183.69
		$peri_{th}$[m]	1.304	β_4[°]	58.35		
				t_{b4}[mm]	24.69		

this figure, choking behavior is improved a lot.

Figure 4.6 gives the pressure ratio characteristics for another configuration, which has a long vaneless diffuser. Again no efficiency data is available. A similar behavior with O-rotor stage is obtained, which also has a long vaneless diffuser. Klausner and Gampe [18] again explains this behavior with the small α_2 at the impeller exit at low mass flow rates which causes large diffusion losses at the long vaneless diffuser. The errors on pressure ratio estimation reaches 7.5% at high speeds.

Figure 4.7 presents the total pressure and absolute Mach number curves against $\dot{m}$ at 28541 rpm, compared with an experimental result and a meanline solution by the reference [19] for the configuration with vaned diffuser. A good match with the

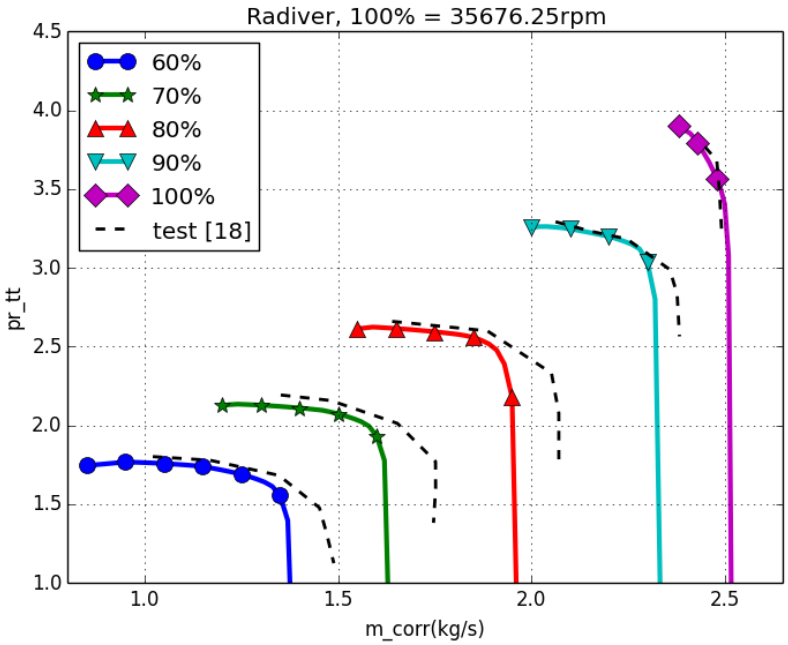

Figure 4.4: Radiver Performance Map with Vaned Diffuser, PR_{tt} $vs.$ $\dot{m}_{corr}$

experimental case is obtained although deviations occur in the choking range due to abrupt choking behavior.

4.3 NASA CC3 Stage

The NASA CC3 Stage consists of an impeller with 15 main and 15 splitter blades having high backswept and a vaned diffuser of wedge type with 24 vanes. It has also a configuration with a vaneless diffuser. The detailed geometry can be found in references [18, 22, 23] and Table 4.4.

As it can be seen from Figure 4.8, a quite good estimation of both pressure ratio and efficiency characteristics is obtained for the configuration with vaned diffuser. Errors for the efficiency estimation are below 3% and errors for choking estimation are below 1%.

Figure 4.9 shows the estimation of pressure ratio and efficiency characteristics for the configuration with vaneless diffuser. The solution seems better compared to the solutions obtained for the vaneless diffuser configurations of O-rotor stage and

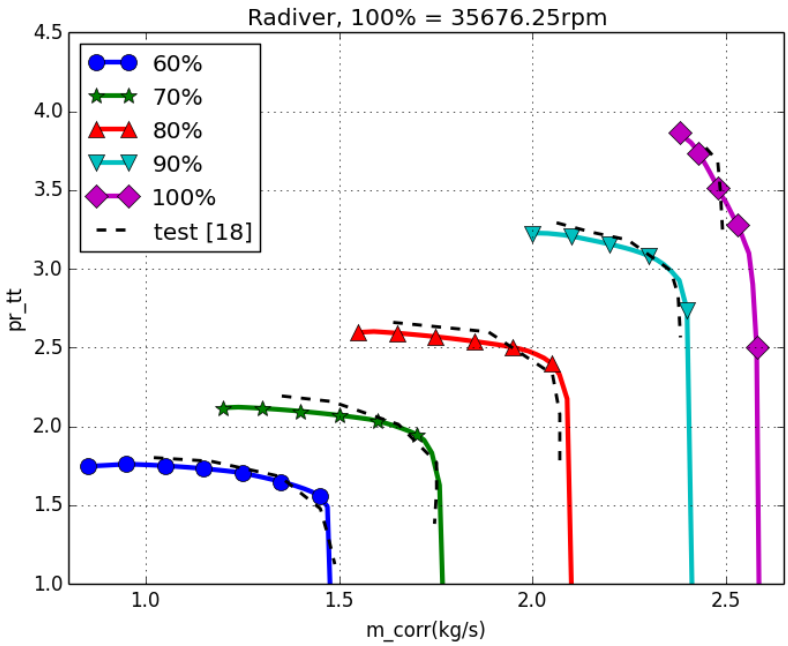

Figure 4.5: Radiver Performance Map with Vaned Diffuser, Vaned Diffuser Throat Blockage Removed, PR_{tt} $vs.$ $\dot{m}_{corr}$

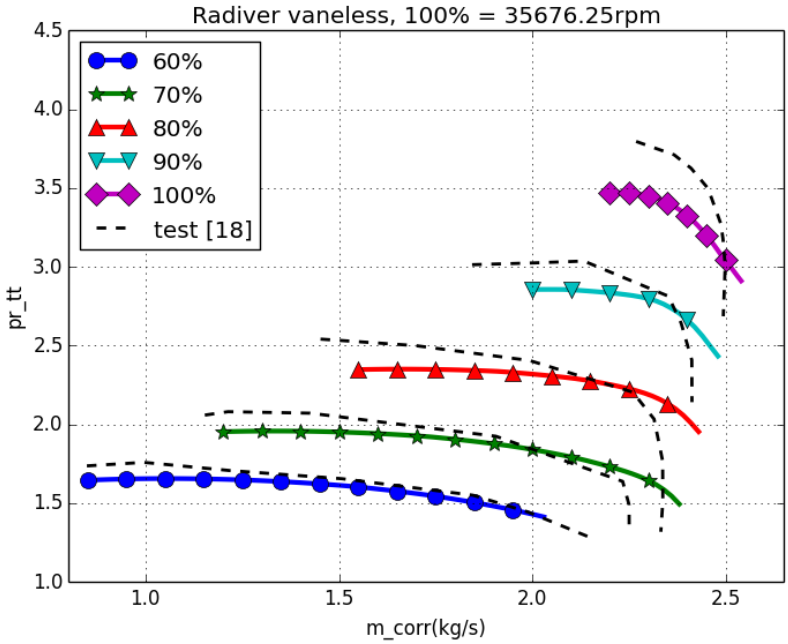

Figure 4.6: Radiver Performance Map with Vaneless Diffuser, PR_{tt} $vs.$ $\dot{m}_{corr}$

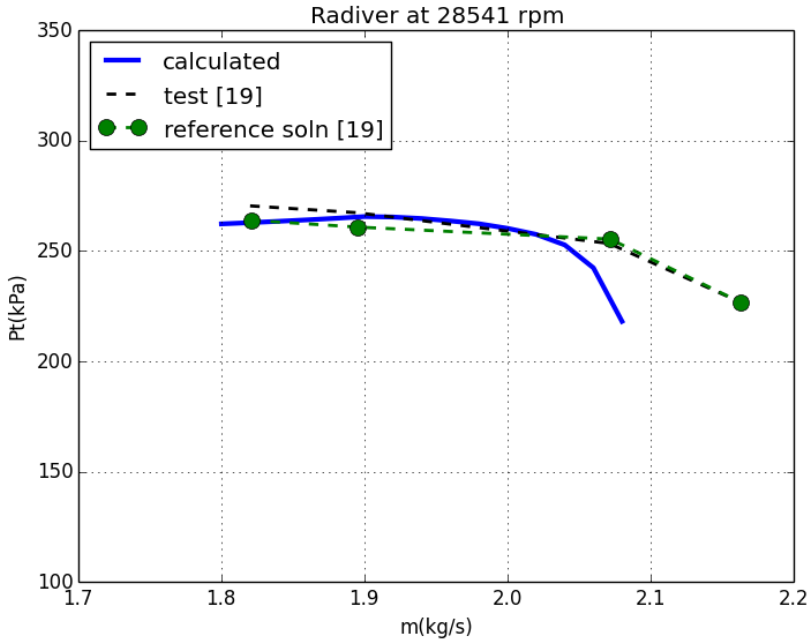

(a) Total Pressure

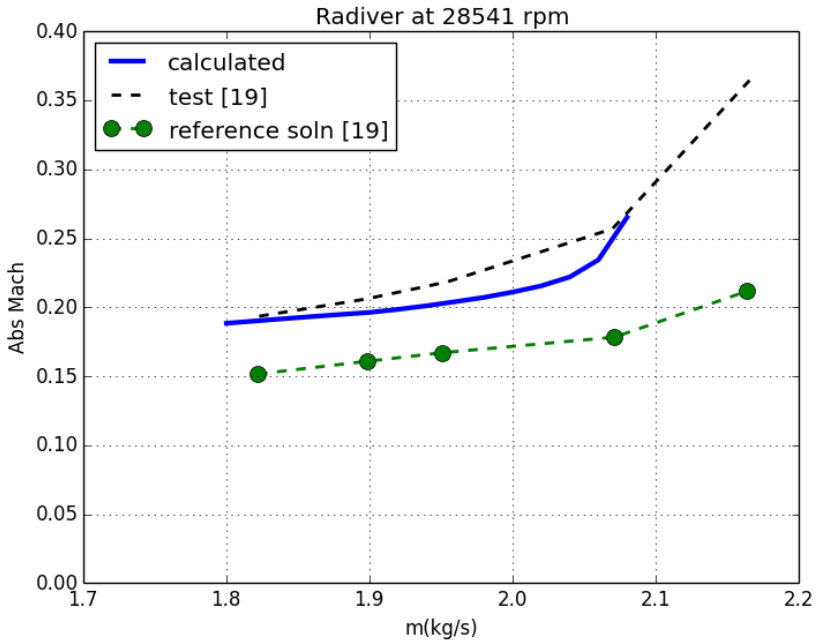

(b) Absolute Mach

Figure 4.7: Radiver, Vane Diffuser Exit

Table 4.4: NASA CC3 Stage Geometry [18]

Impeller							
Inlet		Throat		Tip		Overall	
r_{1h}[mm]	41.37	A_{th}[mm^2]	17499.5	r_2[mm]	215.2	z_{FB}	15
r_{1s}[mm]	104.95	β_{th}[°]	52.394	b_2[mm]	17.05	z_{SB}	15
β_{1h}[°]	50.83	$peri_{th}$[m]	2.556	β_2[°]	40	L_b[mm]	260.26
β_1[°]	41.883			α_{c2}[°]	86.15	L_{fb}[mm]	250.927
β_{1s}[°]	33.464			t_{b2}[mm]	3.0	L_{sb}[mm]	172.47
α_{c1}[°]	1.68					s_{cl}[mm]	0.372
κ_{m1}[rad/m]	-2.49					s_d[mm]	0.372
t_{b1}[mm]	3.0						
Vaneless diffuser							
r_3[mm]	232.41 (253.936 for the vaneless configuration)						
Type	Constant width						
Vaned diffuser							
Inlet		Throat		Tip		Overall	
β_3[°]	12.23	A_{th}[mm^2]	5980.798	r_4[mm]	362	Z_d	24
t_{b3}[mm]	0.419	h_{th}[mm]	14.09	b_4[mm]	17.05	L_b[mm]	242.05
		$peri_{th}$[m]	1.49	β_4[°]	56		
				t_{b4}[mm]	38.38		

Radiver stage. This is due to the fact that vaneless diffuser of this stage is comparatively short and impeller blades have high backsweep. Choking losses at the highest speed are overestimated causing some large deviations in this region. The deviations reach 17% for the pressure characteristics and 10% for the efficiency characteristics. However, the deviations for the rest of the operating range are below 3%.

4.4 Jones Stage

The Stage of Jones consists of an impeller with 17 main and 17 splitter blades having no backswept and an airfoil type vaned diffuser with 41 vanes. The detailed geometry can be found in references [18, 24] and Table 4.5. The pressure ratio of the stage is higher than the limits mentioned by Aungier [13]; however, it is included to see how the analysis behave outside its limits.

As it can be seen from Figure 4.10, a good estimation of both characteristics obtained besides the regions of choke for the 95% and 90% speeds, where some overestimation of the choking flow rate is obtained. Maximum deviation of choking mass flow is around 2.5% at these speeds, which causes some large deviations in efficiency characteristics in the choking regions.

4.5 A Case with a Return Channel

Since there is no well defined test case for a stage with a return system in the literature, a commercial meanline software named as Compal, which belongs to Concepts NREC Inc., is used to create a stage with return channel and compare the results with the developed code.

The stage shown in Figure 4.11 is created in Compal. It has an impeller with a rotational speed of 42000 rpm and a backsweep angle of 60° (from tangential direction). A wedge type diffuser is employed and a return system is included.

The obtained results are shown in Figures 4.12 and 4.13. The deviations are small

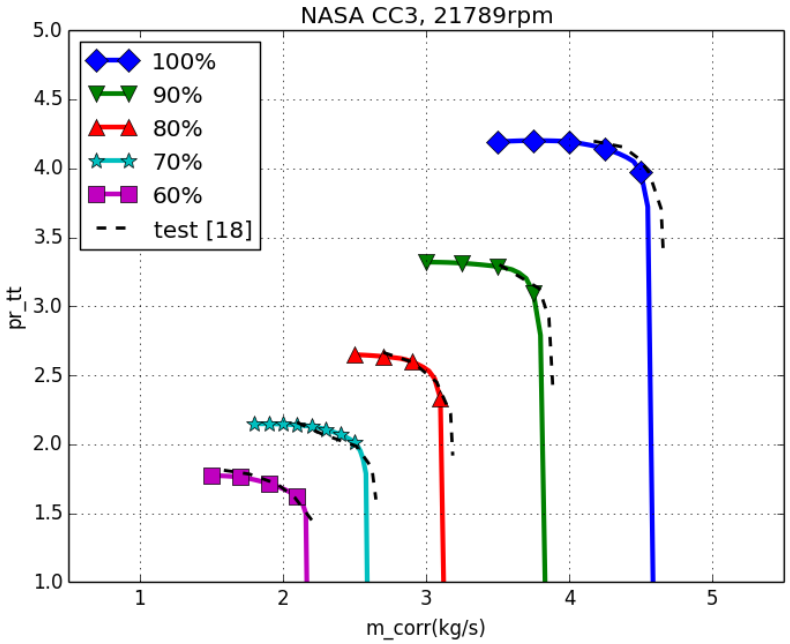

(a) PR_{tt} *vs.* $\dot{m}_{corr}$

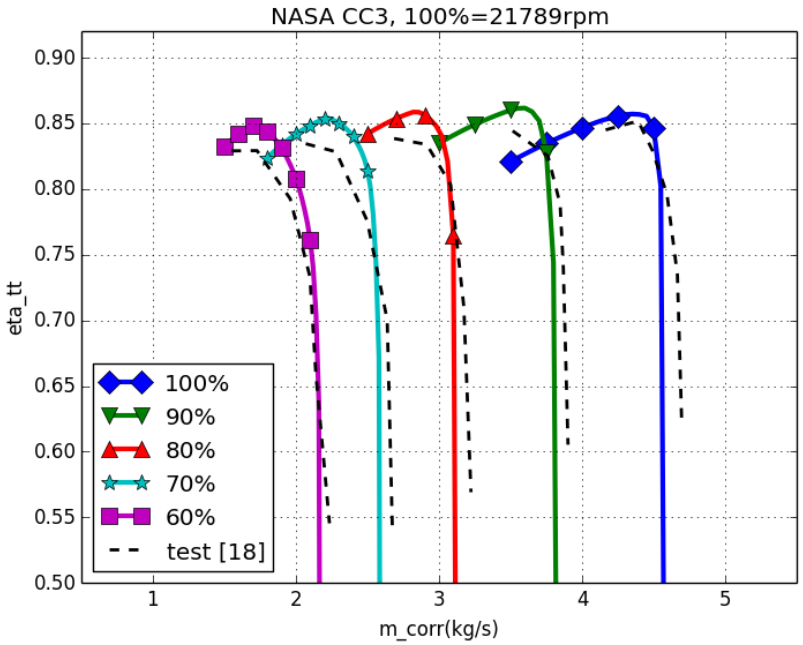

(b) η_{tt} *vs.* $\dot{m}_{corr}$

Figure 4.8: NASA CC3 with Vaned Diffuser Performance Map

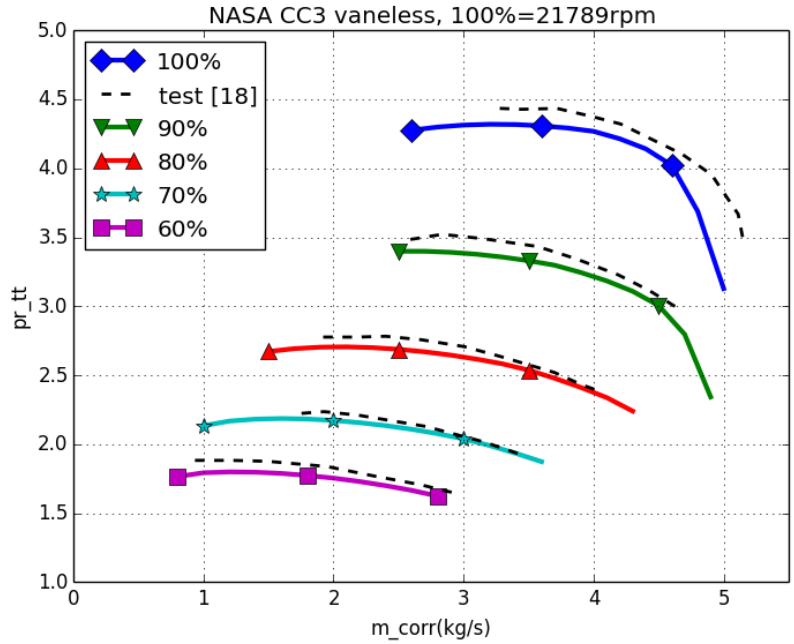

(a) PR_{tt} *vs.* $\dot{m}_{corr}$

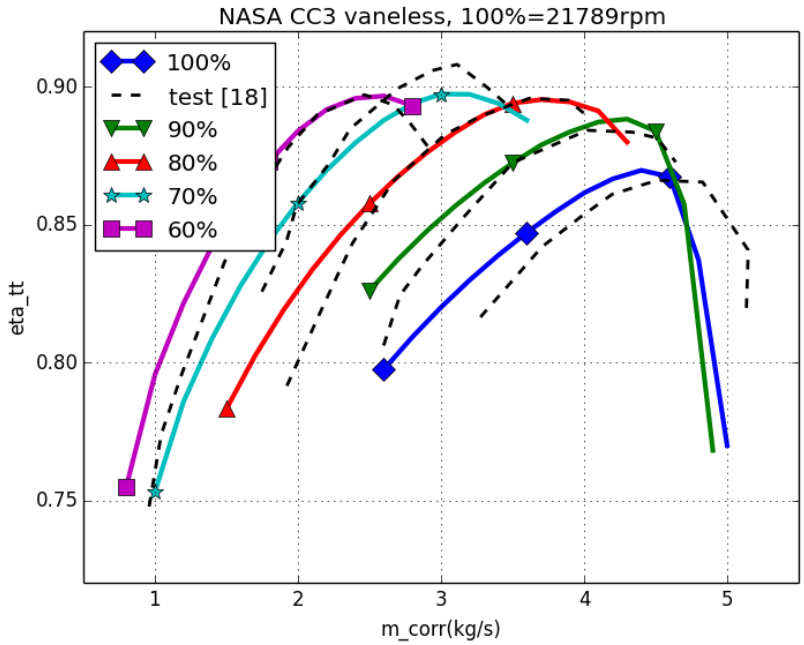

(b) η_{tt} *vs.* $\dot{m}_{corr}$

Figure 4.9: NASA CC3 with Vaneless Diffuser Performance Map

Table 4.5: Jones Stage Geometry [18]

Impeller							
Inlet		Throat		Tip		Overall	
r_{1h}[mm]	30.48	A_{th}[mm^2]	5788.44	r_2[mm]	124.46	z_{FB}	17
r_{1s}[mm]	67.31	β_{th}[°]	39.87	b_2[mm]	5.08	z_{SB}	17
β_{1h}[°]	51.9	$peri_{th}$[m]	1.701	β_2[°]	90	L_b[mm]	114.175
β_1[°]	36.525			α_{c2}[°]	82	L_{fb}[mm]	102.801
β_{1s}[°]	30			t_{b2}[mm]	1.1	L_{sb}[mm]	59.3
α_{c1}[°]	2.1					s_{cl}[mm]	0.55
κ_{m1}[rad/m]	-3.5					s_d[mm]	0.55
t_{b1}[mm]	2						
Vaneless diffuser							
r_3[mm]	130.685						
Type	Constant width						
Vaned diffuser							
Inlet		Throat		Tip		Overall	
β_3[°]	24.83	A_{th}[mm^2]	1650	r_4[mm]	177	Z_d	41
t_{b3}[mm]	0.48	h_{th}[mm]	7.01	b_4[mm]	5.08	L_b[mm]	81.54
		$peri_{th}$[m]	1.18	β_4[°]	45.24		
				t_{b4}[mm]	0.9		

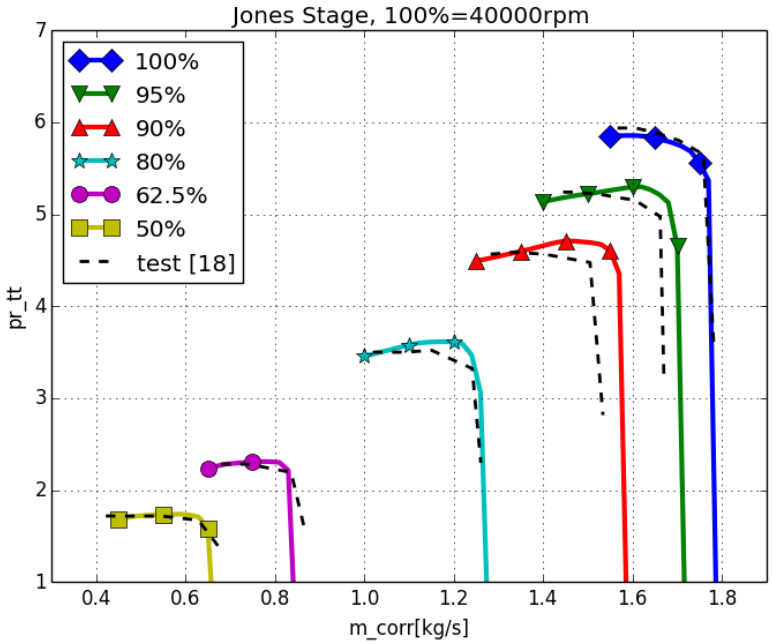

(a) PR_{tt} *vs.* $\dot{m}_{corr}$

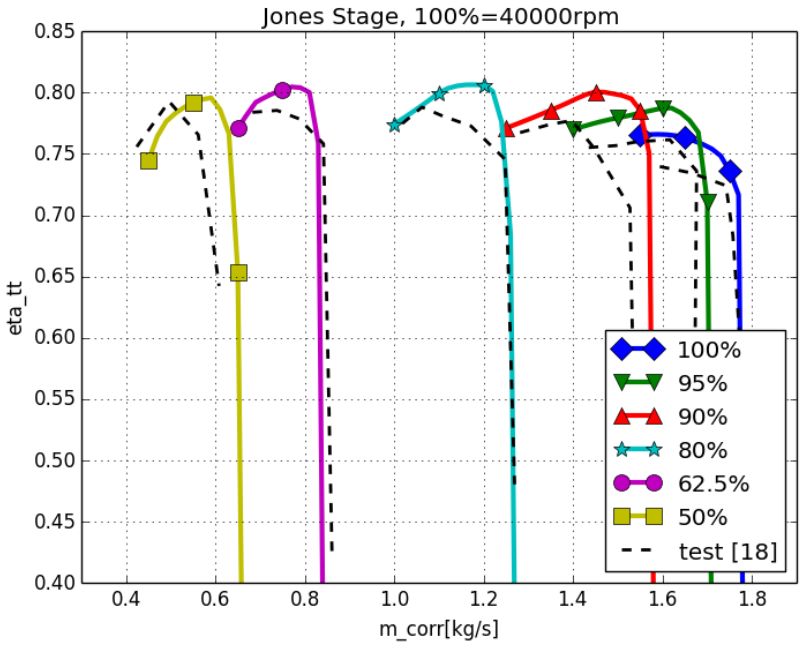

(b) η_{tt} *vs.* $\dot{m}_{corr}$

Figure 4.10: Jones Stage with Vaned Diffuser Performance Map

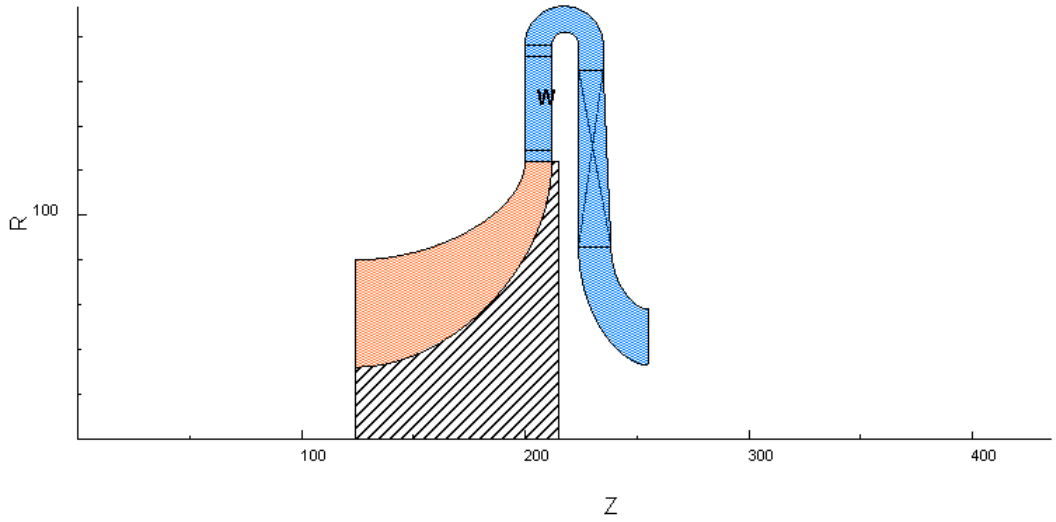

Figure 4.11: The Stage with a Return System

except in choking regions. It is not clear how the calculations are done for the throat parameters or how the choking losses are calculated for the vaned diffuser within Compal. The deviations within the choking region may be caused by the differences in these calculations from the developed code.

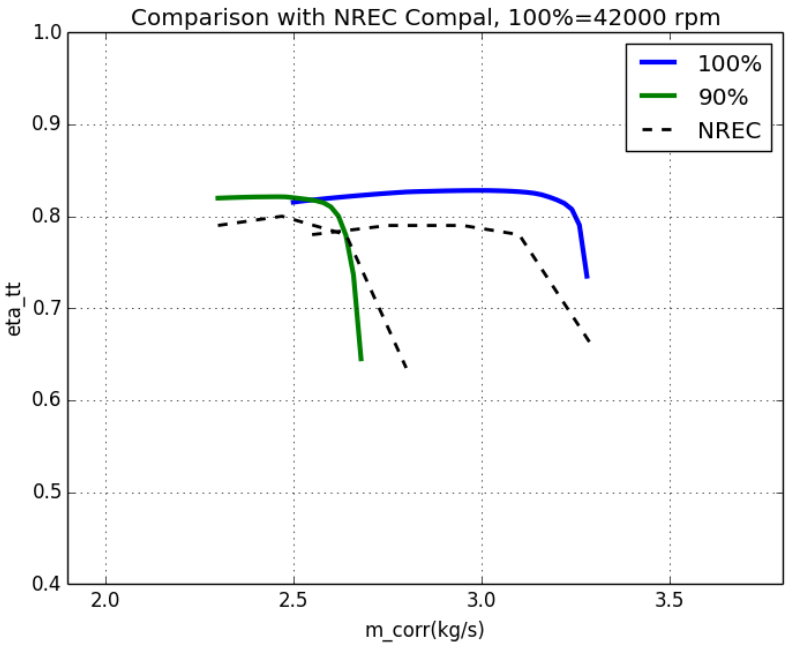

Figure 4.12: Efficiency Map for the Stage with a Return System

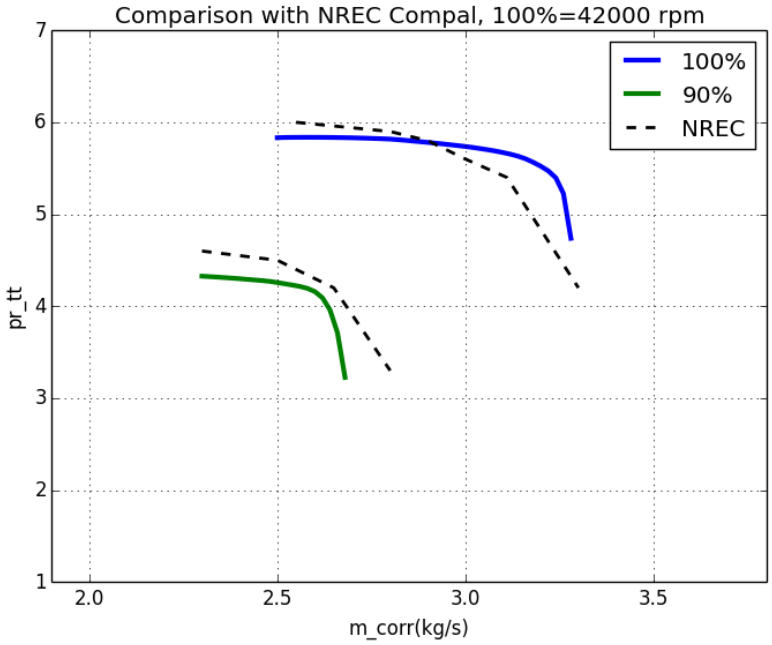

Figure 4.13: Pressure Ratio Map for the Stage with a Return System

CHAPTER 5

CONCLUDING REMARKS

The aim of this thesis is to develop a computer program that can be used to estimate the performance of radial compressors using mean-line method. For this purpose, each stage component is analyzed individually using an extensive set of models for flow losses, blockage and other important flow phenomena.

Two famous approaches to the impeller analysis, namely the one zone model of R. Aungier [13] and two zone model of D. Japikse [4], are investigated and it is observed that the one zone model performs better at off design points if the two zone model is used together with the primitive TEIS model. Therefore, the one zone model is preferred for the impeller analysis. The procedure given by Herbert [12] and empirical correlations given by Aungier [13] are used to create the impeller geometry and calculate some preliminary values for the impeller parameters needed by the impeller analysis. One dimensional conservation equations are employed for the vaneless diffuser analysis along with the loss models for diffusion, curvature, wall friction and boundary layer growth. A simple marching technique is used to solve these equations. Vaned diffuser and return channel are analyzed using the loss models given by Aungier [13] along with minimum loss deviation model of Howell [44] and off-design deviation model of Johnsen and Bullock [45]. The empirical correlations and design limitations given by Aungier [13] and the procedure given by Johannes [17] are used to size the vaned diffuser and calculate some preliminary values for the vaned diffuser parameters needed by the vaned diffuser analysis. IGV is analyzed using the profile loss coefficient of Ainley and Mathieson [46] and secondary loss coefficient of Dunham [47] along with the procedure given by

Herbert [12].

Four different cases are investigated for the validation of the written code and it is observed that the analysis procedure performs well for the stages with backswept impellers and vaned diffusers. For the stages with radial blades and long vaneless diffusers, an overestimation of the diffusion losses is observed at low mass flow rates. This overestimation is due to the low α_2 values at the impeller exit which reduces the diffusion efficiency of the vaneless diffuser. An overestimation of the blockage at the impeller and vaned diffuser throat is also observed for some cases.

As a future work, more test cases should be investigated, especially the ones with a return channel. Vaneless diffuser diffusion loss correlation should be improved to handle the cases with long vaneless diffuser and radially bladed impellers. Throat blockage correlations should also be revisited to improve the accuracy of the analysis within the choking region.

REFERENCES

[1] J.D. Denton and W.N. Dawes. Computational fluid dynamics for turbomachinery design. *Proceedings of the Institution of Mechanical Engineers*, 213, 1999.

[2] C.H. Wu. A general through flow theory of fluid flow with subsonic and supersonic velocities in turbomachines of arbitrary hub and casing shapes. *NACA paper TN2302*, 1951.

[3] E. Steinhardt. *Aero-Engine Design: State of the Art, HP Compressor*. Von Karman Institute for Fluid Dynamicsl, 2003.

[4] D. Japikse. *Centrifugal Compressor Design and Performance*. Concepts ETI, Inc., 1996.

[5] A. Whitfield and N.C. Baines. *Design of Radial Turbomachines*. Longman Scientific and Technical, 1990.

[6] S.L. Dixon. *Fluid Mechanics and Thermodynamics of Turbomachinery*. Butterworth-Heinemann, 1998.

[7] N.A. Cumpsty. *Compressor Aerodynamics*. Longman Scientific and Technical, 1989.

[8] D. Japikse and N.C Baines. *Introduction to Turbomachinery*. Concepts ETI, 1994.

[9] H.W. Oh, E.S. Yoon, and M.K. Chung. An optimum set of loss models for performance prediction of centrifugal compressors. *Proceedings of IMechE, Part A: Journal of Power and Energy*, 1997.

[10] S. K. Roberts. Effects of fluid properties on the aerodynamic performance of turbomachinery for semi-closed cycle gas turbine engines using o2/co2 combustion. Master's thesis, Carleton University, 2001.

[11] M. R. Galvas. Fortran program for predicting off-design performance of centrifugal compressors. *NASA TN D-7487*, 1973.

[12] M.V. Herbert. A method of performance prediction for centrifugal compressors. *Aeronautical Research Council Reports and Memoranda, No. 3843*, 1980.

[13] R.H. Aungier. *Centrifugal Compressors, A Strategy for Aerodynamic Design and Analysis*. Asme Press, 2000.

[14] R.H. Aungier. Mean streamline aerodynamic performance analysis of centrifugal compressors. *ASME*, 1995.

[15] R.C. Dean and Y. Senoo. Rotating wakes in vaneless diffusers. *Journal of Basic Engineering*, 1960.

[16] D. Eckardt. Instantaneous measurements in the jet-wake discharge flow of a centrifugal compressor impeller. *Journal of Engineering for Power*, 1975.

[17] J. Schiff. A preliminary design tool for radial compressors. Master's thesis, Lund University, Division of Thermal Power Engineering, 2013.

[18] E. Klausner and U. Gampe. Evaluation and enhancement of a one-dimensional performance analysis method for centrifugal compressors. *Proceedings of ASME Turbo Expo*, 2014.

[19] A.L. de Wet. Performance investigation of a turbocharger compressor. Master's thesis, University of Stellenbosch, Department of Mechanical and Mechatronic Engineering, 2011.

[20] L. Moroz, P. Pagur, Y. Govoruschenko, and L. Romanenko. Integrated conceptual design environment for centrifugal compressors flow path design. *Asme International Mechanical Engineering Congress and Exposition*, 2008.

[21] O. Borm, B. Balassa, H. Kau, and P. Kau. Comparison of different numerical approaches at the centrifugal compressor radiver. *American Institute of Aeronautics and Astronautics, Inc. ISABE 1242*, 2011.

[22] T.F. McKain and G.J. Holbrook. Coordinates for a high performance 4:1 pressure ratio centrifugal compressor. *NASA CR-204134*, 1997.

[23] S. Kulkarni, T.A. Beach, and G.J. Skoch. Computational study of the cc3 impeller and vaneless diffuser experiment. *NASA TM-216566*, 2013.

[24] M.G. Jones. The performance of a 6.5 pressure ratio centrifugal compressor having a radially-vaned impeller. *Aeronautical Research Council, C.P. No. 1385*, 1977.

[25] H.I.H. Saravanamuttoo, G.F.C. Rogers, and H. Cohen. *Gas Turbine Theory*. Prentice Hall, 2001.

[26] Jet and rocket propulsion. *http://physics-tutor.site90.net/drupal/node/16*, 2008. Accessed: 2015-05-16.

[27] N. Falck. Axial flow compressor mean line design. Master's thesis, Lund University, Division of Thermal Power Engineering, Department of Energy Sciences, 2008.

[28] R.H. Aungier. *Axial-Flow Compressors, A Strategy for Aerodynamic Design and Analysis*. Asme Press, 2000.

[29] E.A. Baskharone. *Principles of Turbomachinery in Air-Breathing Engines*. Cambridge University Press, 2006.

[30] B.W. Botha and A. Moolman. Determining the impact of the different losses on centrifugal compressor design. *R and D Journal*, 2005.

[31] M. Olivero. *Evolution of a Centrifugal Compressor From Turbocharger to Micro Gas Turbine Applications*. PhD thesis, Dellft Technical University, 2012.

[32] F.J. Wiesner. A review of slip factors for centrifugal impellers. *ASME Journal of Engineering for Power*, 1967.

[33] J.K. Miller. Anatomy of a turbocharger. *http://www.cartechbooks.com /techtips/anatomy-of-a-turbocharger-whats-inside-and-how-it-works/*, 2015. Accessed: 2015-04-26.

[34] J.W. Daily and R.E. Nece. Chamber dimension effects on induced flow and frictional resistance of enclosed rotating disks. *ASME Journal of Basic Engineering*, 1960.

[35] J.W. Daily and R.E. Nece. Roughness effects on frictional resistance of enclosed rotating disks. *ASME Journal of Basic Engineering*, 1960.

[36] S. Lieblein, F.C. Schwenk, and R.L. Broderick. Diffusion factor for estimating losses and limiting blade loadings in axial-flow compressor blade elements. *NACA TN 3662*, 1953.

[37] S. Lieblein. Loss and stall analysis of compressor cascades. *ASME, Journal of Basic Engineering*, 1959.

[38] X. Gong and R. Chen. Total pressure loss mechanism of centrifugal compressors. *Mechanical Engineering Research*, 2014.

[39] I. Britton and J.E. Donald Gauthier. Performance prediction of centrifugal impellers using a two-zone model. *Proceedings of ASME Turbo Expo*, 2008.

[40] R.J. Pelton. One-dimensional radial flow turbomachinery performance modeling. Master's thesis, Brigham Young University, 2007.

[41] K. Im. *Development of a Design Method for Centrifugal Comporessors*. PhD thesis, Michigan State University, Mechanical Engineering Department, 2012.

[42] P.M. Came. The development, application and experimental evaluation of a design procedure for centrifugal compressors. *Proceedings of IMechE*, 1978.

[43] J.D. Stanitz. One-dimensional compressible flow in vaneless diffusers of radial and mixed-flow centrifugal compressors, including effects of friction, heat transfer and area change. *NACA TN 2610*, 1952.

[44] A.R. Howell. Development of british gas turbine unit. *ASME*, 1947.

[45] I.A. Johnsen and R.O. Bullock. Aerodynamic design of axial flow compressors. *NASA SP-36*, 1965.

[46] D.G. Ainley and G.C.R. Mathieson. A method of performance estimation for axial-flow turbines. *ARC R and M 2974*, 1957.

[47] J. Dunham. A review of cascade data on secondary losses in turbines. *Journal of Mechanical Engineering Science*, 1970.

[48] E. Goos and A. Burcat. Third millenium ideal gas and condensed phase thermochemical database. *http://burcat.technion.ac.il/dir/Archives/THERM2010.DAT*, 2013. Accessed: 2015-05-01.

[49] G. Cazelais. Simpson's rule. *http://pages.pacificcoast.net/ cazelais/187/ simpson.pdf*, 2008. Accessed: 2015-04-28.

[50] S.C. Chapra and R.P. Canale. *Numerical Methods for Engineers*. McGraw-Hill, 2006.

APPENDIX A

THERMODYNAMIC MODELS

A.1 Gas Model

Fourth degree NASA coefficients [48] are used for the temperature dependent c_p. It is given as,

$$c_p = R\left(a_1 + a_2T + a_3T^2 + a_4T^3 + a_5T^4\right) \tag{A.1}$$

where R is the gas constant of air ($R = 287.062\ j/kg/K$) and coefficients of the polynomial are given in Table A.1. The term in the parenthesis is dimensionless. Knowing the gas constant, R, and the specific heat, c_p, specific heat ratio is given by,

$$\gamma = c_p/(c_p - R) \tag{A.2}$$

Sutherland's formula is used to update the viscosity with temperature. It is given as,

$$\mu = 1.716 * 10^{-5}(\frac{T}{273.15})^{1.5}\frac{383.55}{T + 110.4} \tag{A.3}$$

where T is in K and μ is in $kg/m/s$.

Table A.1: NASA polynomial coefficients [48]

T > 1000	T < 1000
$a_1 = 3.08792717E + 00$	$a_1 = 3.56839620E + 00$
$a_2 = 1.24597184E - 03$	$a_2 = -6.78729429E - 04$
$a_3 = -4.23718945E - 07$	$a_3 = 1.55371476E - 06$
$a_4 = 6.74774789E - 11$	$a_4 = -3.29937060E - 12$
$a_5 = -3.97076972E - 15$	$a_5 = -4.66395387E - 13$

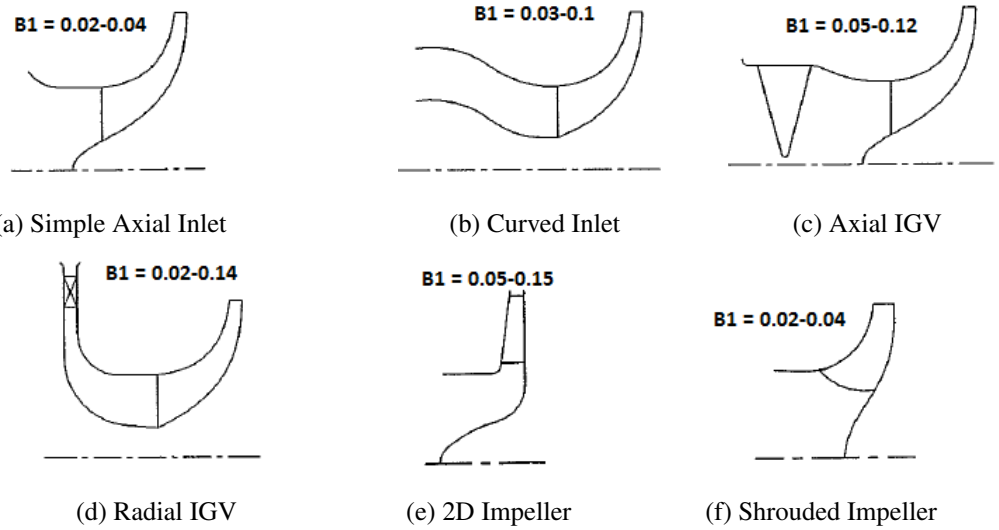

(a) Simple Axial Inlet (b) Curved Inlet (c) Axial IGV

(d) Radial IGV (e) 2D Impeller (f) Shrouded Impeller

Figure A.1: Assumed Inlet Blockage Values [4]

A.2 Inlet Blockage

Inlet blockage values which can be used during impeller inlet analysis are given in Figure A.1

A.3 Skin Friction Coefficient

Wall friction is one of the loss mechanisms common to all stage components and a general formulation of the skin friction coefficient is needed covering all flow regimes. [13] The formulation used in this thesis is based on the generalized pipe friction data, where the skin friction coefficients are correlated as a function of Reynolds number based on pipe diameter. It is given as,

$$Re_d = \rho V d/\mu \tag{A.4}$$

The usual practice is to replace d with d_H for general passages. Skin friction coefficients are also a function of wall surface finish; however, its effect is neglected in this thesis.

For $Re_d < 2000$, the flow is laminar and the skin friction coefficient is calculated as [13],

$$c_{f,l} = 16/Re_d \tag{A.5}$$

For $Re_d > 4000$, the flow is turbulent and the skin friction coefficient is calculated as [19],

$$1/\sqrt{4c_{f,t}} = -1.8\log_{10}(6.9/Re_d) \tag{A.6}$$

The transition from laminar to turbulent is modeled as weighted averages of the above calculated values. It is given by,

$$c_f = c_{f,l} + (c_{f,t} - c_{f,l})(Re_d/2000 - 1) \tag{A.7}$$

A.4 Hydraulic Diameter

Hydraulic diameter is given by,

$$d_H = 4\,\frac{CrossSectionalArea}{WettedPerimeter} \tag{A.8}$$

From throat to tip, the mean hydraulic diameter of the impeller can be written as,

$$d_H = \frac{4A_{th}}{peri_{th}}\frac{1}{2} + \frac{4A_2\sin\beta_2}{2\pi d_2\sin\beta_2 + 2zb_2 - 2zt_{b2}}\frac{1}{2} \tag{A.9}$$

After some algebraic manipulations,

$$d_H = \frac{2A_{th}}{peri_{th}} + \frac{A_2\sin\beta_2}{\pi d_2\sin\beta_2 + zb_2 - zt_{b2}} \tag{A.10}$$

where $peri_{th} \approx 2\pi d_{th}\sin\beta_{th} + 2z_{FB}h_{th} - 2z_{FB}t_{b1}$. Similarly for the vane diffuser,

$$d_H = \frac{2A_{th}}{peri_{th}} + \frac{A_4\sin\beta_4}{\pi d_4\sin\beta_4 + z_{VD}b_4} \tag{A.11}$$

The same formula can also be used for the return channel.

APPENDIX B

NUMERICAL METHODS

B.1 Simpson's Rule

Simpson's rule is a numerical integration method that employs high order polynomials (2nd order or higher) to estimate the value of a definite integral. If 2nd order polynomials are used as shown in Figure B.1, the following Simpson's formula is obtained,

$$\int_a^b f(x)\,\mathrm{d}x \approx \frac{\Delta x}{3}(y_0 + 4y_1 + 2y_2 + 4y_3 + 2y_4 + ... + 4y_{n-1} + y_n) \tag{B.1}$$

B.2 Newton-Raphson Method

If an initial guess of a root of the function, $f(x)$, is x_i, a tangent extending from the point $[x_i, y_i]$ can be drawn and the point where this tangent crosses the x-axis usually

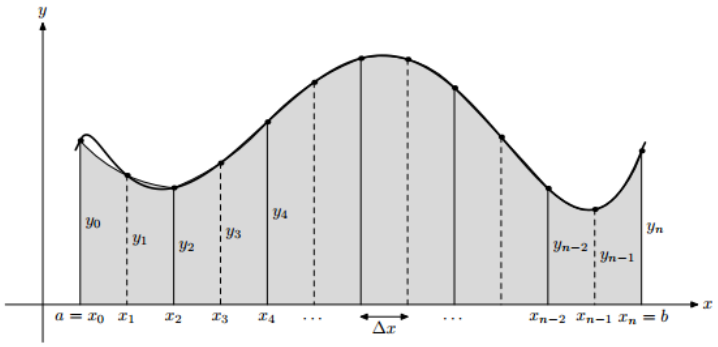

Figure B.1: Simpson's Rule [49]

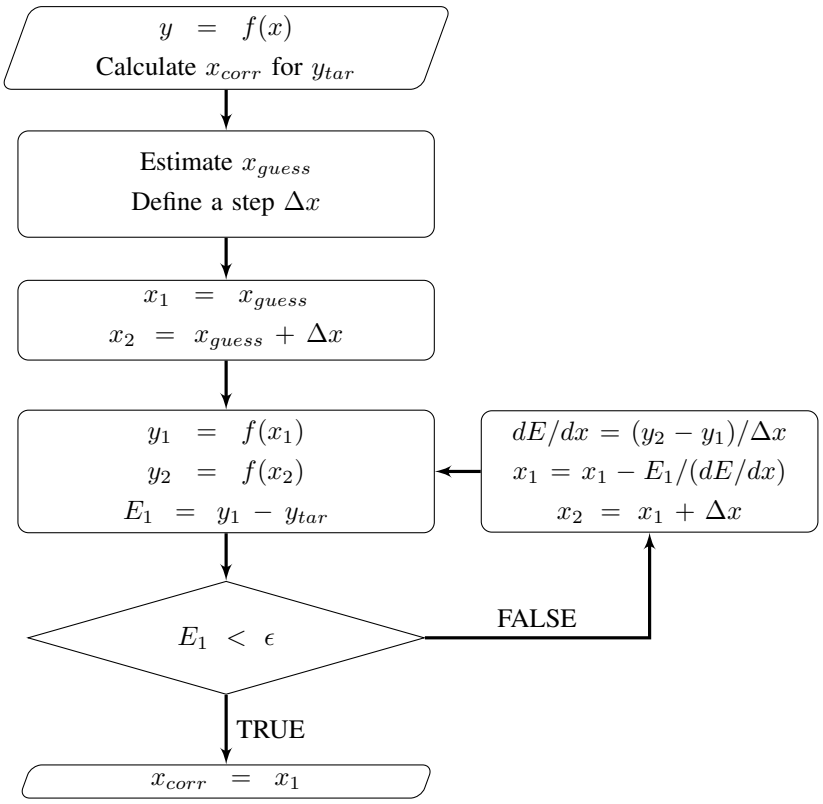

Figure B.2: Newton Raphson Method with Numerical Differentiation

gives an improved estimate of the root, x_{i+1}. [50] That is,

$$x_{i+1} = x_i - \frac{f(x_i)}{f'(x_i)} \tag{B.2}$$

If the derivative of the function, $f'(x_i)$, can not be calculated directly, it can be calculated numerically. The procedure given in Figure B.2 uses numerical differentiation to find the root of $y = f(x)$. The target y value is y_{tar} and x_{corr} is the corresponding root.